# ULTRA-THIN DIELECTRIC LAYERS ON METAL SUBSTRATES STUDIED BY SCANNING TUNNELING MICROSCOPY AND SCANNING TUNNELING SPECTROSCOPY

THÈSE N$^{O}$ 3962 (2007)

PRÉSENTÉE LE 14 NOVEMBRE 2007

À LA FACULTÉ DES SCIENCES DE BASE

Laboratoire de physique des surfaces

PROGRAMME DOCTORAL EN PHYSIQUE

ÉCOLE POLYTECHNIQUE FÉDÉRALE DE LAUSANNE

POUR L'OBTENTION DU GRADE DE DOCTEUR ÈS SCIENCES

PAR

Hans - Christoph PLOIGT

Diplom - Chemiker, Philipps - Universität Marburg, Allemagne
et de nationalité allemande

acceptée sur proposition du jury:

Prof. R. Schaller, président du jury
Prof. W.-D. Schneider, directeur de thèse
Dr R. Fasel, rapporteur
Prof. U. Höfer, rapporteur
Prof. J. Repp, rapporteur

ÉCOLE POLYTECHNIQUE
FÉDÉRALE DE LAUSANNE

Suisse
2007

# Abstract

In this thesis, ultra-thin dielectric layers on metal substrates are studied mainly by scanning tunneling microscopy and scanning tunneling spectroscopy.

In chapter 2, field emission resonances, i.e. bound states in the potential well between sample and tip with an applied voltage, are used to determine the local work function on a sample with patches of different structural composition. To do so, a simple theoretical model is developed and used to simulate the peak positions of the measured dI/dV spectra. In the present case the sample is a Ag(100) surface covered by up to three monolayers of NaCl. The presented method is also applicable to other systems suitable for STM measurements. Additionally, the surface potential is locally probed in the dipole layer region between domains of different work function.

In chapter 3, new molecular structures on silver surfaces are presented, that are formed by a mixture of gases. This mixture contains the small molecules $H_2$, $H_2O$, CO, $CO_2$, and $N_2$. No final conclusion can be drawn on the chemical nature of these structures due to the impossibility of the scanning tunneling microscope to determine chemical species. But already the presence of these structures indicates that there is a multitude of unknown interactions, that are possible between a transition metal surface and even smallest molecules.

In chapter 4, the moiré pattern is described that a $BC_3$ film creates on a $NbB_2(0001)$ surface. As the growth of the $BC_3$ sheet is incommensurate, a moiré pattern is formed that modulates the apparent height of the atoms on the STM images, i.e. the local density of states. The $BC_3$ layer exhibits a completely different behavior than the closely related graphite layer, because it is transparent for the tunnel current. In the present case, the $BC_3$ layer is visible on the STM images only by its moiré effect.

**Keywords:** Scanning tunneling microscopy, field emission resonances, local work function, NaCl, $BC_3$, moiré

# Zusammenfassung

Die vorliegende Arbeit handelt von dünnen Schichten dielektrischer Materialien, die auf Metallsubstrate aufgebracht wurden und dann hauptsächlich mit Rastertunnelmikroskopie und Rastertunnelspektroskopie untersucht wurden.

In Kapitel 2 werden Feldemissionsresonanzen, also gebundene Zustände im Potentialtopf zwischen Probe und Spitze bei positiver angelegter Spannung, genutzt, um die lokale Austrittsarbeit einer Probe mit örtlich variierender Zusammensetzung zu bestimmen. Dazu wird ein eindimensionales Modell entwickelt, um die Peakpositionen in den gemessenen dI/dV Spektren zu simulieren. Die Probe besteht im vorliegenden Fall aus einer bis zu drei Monolagen dicken NaCl Schicht auf einer Ag(100) Oberfläche. Die vorgestellte Methode läßt sich aber auch auf andere Systeme anwenden und erlaubt es darüberhinaus, die Dipolschicht zwischen Bereichen unterschiedlicher Austrittsarbeit zu charakterisieren.

In Kapitel 3 werden neue molekulare Strukturen auf Silberoberflächen vorgestellt, die durch ein Gemisch an leichten Gasen auf der Übergangsmetalloberfläche entstanden sind. Durch die mangelnde Fähigkeit des Rastertunnelmikroskops, chemische Elemente zu bestimmen, läßt sich zwar keine endgültige Schlußfolgerung über die chemische Natur dieser Strukturen treffen, jedoch gibt allein schon das Vorhandensein dieser Strukturen Hinweise auf die Vielfalt an Wechselwirkungen, die zwischen Übergangsmetalloberflächen und selbst kleinsten Molekülen möglich ist.

In Kapitel 4 wird das Moiré Muster beschrieben, das eine $BC_3$ Schicht auf einer $NbB_2(0001)$ Oberfläche erzeugt. Da das Wachstum der $BC_3$-Schicht inkommensurabel mit dem Substrat ist, ergibt sich das Moiré Muster, das die scheinbare Höhe der Atome auf den STM Bildern, sprich die lokale Zustandsdichte, moduliert. Die $BC_3$-Schicht verhält sich hierbei völlig anders als die verwandte Graphitschicht, da sie für den Tunnelstrom transparent ist und auf den STM Bildern nur durch das Moiré Muster erkennbar ist.

**Schlagworte:** Rastertunnelmikroskopie, Feldemissionsresonanzen, lokale Austrittsarbeit, NaCl, $BC_3$, Moiré

# Contents

# Abbreviations

These are the most frequently used abbreviations in this thesis.

| | |
|---|---|
| STM | scanning tunneling microscope or scanning tunneling microscopy, depending on the context |
| STS | scanning tunneling spectroscopy |
| $k_B$ | Boltzmann's constant |
| $E_{F,s}$ | Fermi level of the sample |
| $E_{F,t}$ | Fermi level of the tip |
| $E_{vac,s}$ | vacuum level of the sample |
| $E_{vac,t}$ | vacuum level of the tip |
| FER | field emission resonance |
| LDOS | local density of states |
| 1D | one dimensional or one dimension, depending on the context |
| 2D, 3D | analogical to 1D |
| $\rho_s$ | density of states of the sample |
| $\rho_t$ | density of states of the tip |
| $e$ | charge of an electron ($1.602 \cdot 10^{-19}\, C$) |
| $\phi_s$ | work function of the sample |
| $\phi_t$ | work function of the tip |
| RT | room temperature |
| ML | monolayer |
| LEED | low energy electron diffraction |
| DFT | density functional theory |
| 2PPE | two photon photoemission |
| IPE | inverse photoemission |
| UPS | ultraviolet photoelectron spectroscopy |
| PEEM | photoemission electron microscopy |
| EELS | electron energy loss spectroscopy |
| NFE | nearly free electron |
| AES | Auger electron spectroscopy |
| $tsd$ | tip-sample distance |

# Chapter 1

# Introduction to STM theory

## 1.1 Introduction

Until the invention of the STM by Binnig and Rohrer surfaces were studied by non-local techniques. But the interest and great motivation of these two researchers was to get informations about the surface at a certain point of the sample. First attempts towards that goal were made since the early 1970's when Young published his first results obtained with the topografiner [1]. He brought a metallic tip in close contact with a metallic sample and applied a high voltage between both. The field emission current between the electrodes was then used as a feedback signal for the tip-sample distance to adjust a chosen current set point. The tip was scanned over the sample by piezo positioners while the feedback circuit set the tip-sample distance in a way to hold the current constant which resulted in rough topographies of the studied surface. Binnig and Rohrer built then the STM in the early 1980's. The principle mechanism to acquire the topographies was the same except that they brought the tip so close to the sample that they could use the tunnel current resulting from a small voltage drop across the junction as a feedback signal [2–4]. This experimental setup needed an extremely efficient vibration damping which was not achieved before [5]. As the tunnel current depends exponentially on the tip-sample distance the topographies were spatially much better resolved, down to atomic resolution [4]. The second big advantage beside the high spatial resolution, that results from the concept of the experiment as a tunneling and not a field emission experiment, was the possibility to study the electronic structure of the sample by scanning tunneling spectroscopy (although the topography images contain electronic information, too, see Sec. 1.2). This is not possible with a field emission experiment where one is restricted to high voltages, i.e. far away from the Fermi level of the sample, the electrons around the Fermi level being the ones determining most of the properties of a metal, i.e. the most interesting to study. Furthermore, the emission area in field emission experiments is of the order of several hundreds of $Å^2$ [6, 7], thus reducing the local character of the experiment. So STM and STS were a breakthrough in surface science that finally lead to the Nobel Prize in 1986 for Binnig and Rohrer[1]. That opened up a large number of new possibilities to study surfaces at the atomic level, for instance: measurements of the local density of states of a surface state [8] and of its lifetime or of the energy gap of a superconductor [9], studies of inelastic processes [10], spin resolved measurements [11], and growth studies at a local scale [12].

[1] Together with Ernst Ruska who invented the scanning electron microscope.

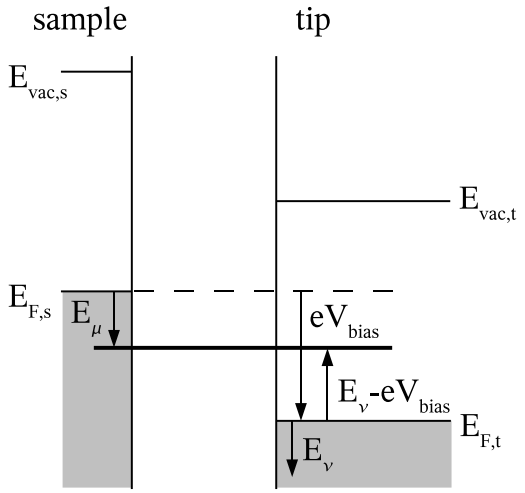


**Figure 1.1** The energetic levels of the states involved in the tunnel process. The situation corresponds to a negative applied voltage, as defined throughout this thesis.

## 1.2 The constant current mode

In the constant current mode, as already shortly described above, one acquires topography images of the sample. The tunnel current is hold constant while the tip scans over the surface. The corresponding changes in tip-sample distance occuring during the scan are then recorded and represented as 3D surfaces, from where the expression topography has its origin. But as the tunnel current does not only depend on the tip-sample distance but also on the density of states in tip and sample these two aspects are combined in the topography images which therefore include electronic information, too.

Bardeen [13] calculated the tunnel current between two electrodes separated by a vacuum gap to (compare Fig. 1.1 for notations)

$$I = \frac{2\pi e}{\hbar} \sum_{\mu,\nu} \left[ f(E_\mu) \left[ 1 - f(E_\nu - eV_{bias}) \right] - f(E_\nu) \left[ 1 - f(E_\mu + eV_{bias}) \right] \right] |M_{\mu\nu}|^2 \, \delta(E_\mu - E_\nu). \tag{1.1}$$

Here, $E_\mu$ and $E_\nu$ are electronic energies in the sample ($\mu$) and tip ($\nu$) with respect to the corresponding $E_F$. $\sum_{\mu\nu}$ means the summation over all sample and tip states. $f(E)$ is the Fermi-Dirac function, $V_{bias}$ the applied bias voltage where positive voltages are defined as shifting $E_{F,t}$ to higher energies with respect to $E_{F,s}$. $\delta(E)$ is the Dirac distribution and $M_{\mu\nu}$ is the tunnel matrix element. There are two terms necessary for forward and backward tunneling due to the thermal broadening of the Fermi edge in tip and sample. That leads to a non-zero backward tunnel probability that reduces the total tunnel current. That becomes especially important if the applied voltage is small compared to $k_B T$. The calculation of $M_{\mu\nu}$ implies the overlap of the eigenfunctions of the sample's Hamiltonian and the tip's Hamiltonian. If one restricts the expression to small voltages ($\sim$10 mV for metal-vacuum-metal tunneling) and 0 K, which turns the Fermi-Dirac functions into step functions then the tunnel current is calculated by

$$I = \frac{2\pi}{\hbar} e^2 V_{bias} \sum_{\mu,\nu} |M_{\mu\nu}|^2 \, \delta(E_\mu - E_F) \delta(E_\nu - E_F). \tag{1.2}$$

But to compare with real experiments one needs an expression for $M_{\mu\nu}$. If one approximates the tip wave functions by spherically symmetric functions, as proposed by Tersoff and Hamman [14], one gets an analytic expression for $M_{\mu\nu}$ and, consequently, the tunnel current:

$$I = \frac{32\pi^3}{\hbar} e^2 V \phi^2 \rho_t(E_F) R^2 \kappa^{-4} \exp\{2\kappa R\} \sum_\mu |\psi_\mu(\vec{r}_0)|^2 \, \delta(E_\mu - E_F), \tag{1.3}$$

where $\phi$ is the work function of tip and sample, supposed to be the same in this case, $\kappa = \sqrt{\frac{2m\phi}{\hbar^2}}$, and $\psi_\mu(\vec{r}_0)$ is the value of the eigenfunction of the sample's Hamiltonian for the energy $E_\mu$ at the center of curvature of the tip.

With the local density of states at $\vec{r}$ defined like

$$\rho(\vec{r}, E) = \sum_n |\psi_n(\vec{r})|^2 \, \delta(E_n - E), \tag{1.4}$$

one sees that the current is directly proportional to the density of states of the sample and of the tip at $E_F$.

If one records the variation of the current while the tip is scanning along the surface at constant height one would obtain a map that represents the local density of states of the sample in the plane that is scanned by the tip. But as the variation in height on a typical sample exceeds the typical tunneling distance of ∼1 nm between tip and sample one would very fast create a contact between tip and sample. This is a probable scenario as additionally, the sample is almost never mounted exactly perpendicular to the tip, which creates an additional, for large scan areas even more important height variation. That means, that that technique, which in fact is rarely applied, is only possible in cases of extremely flat surfaces or small scan areas. Additionally, this type of measurement is restricted by the dynamical range of the current amplifier that covers in most cases only about 3 orders of magnitude. That corresponds roughly to a variation in height of about 3 Å (see Sec. 1.3.2).

Therefore, in most STM measurements the constant current mode is applied. The images obtained for small voltages can be interpreted as maps of LDOS of the sample at $E_F$. Exceptions and extensions of this interpretation are discussed in the following paragraph for finite, but comparably small voltages, in Sec. 2.5 for the field emission regime and in Sec. 2.2 for changes in barrier height due to local work function changes.

Often STM experiments are performed at bias voltages higher than 10 mV. This can be necessary if higher tunnel resistances are needed because either certain sample properties are studied as a function of tunnel resistance or because the sample just does not allow to tunnel at low voltages due to the presence of a band gap as it is the case for semiconductors or due to a possible sensitivity and instability at low voltages. The obtained STM images can be interpreted in a straightforward manner as follows. The principle of Tersoff and Hamann is easily extended to finite voltages. The current is then proportional to [15, 16]

$$I(V_{bias}) \propto \int_0^{eV_{bias}} \rho_t(E - eV_{bias}) \rho_s(E) T(E, V_{bias}, z) dE. \tag{1.5}$$

Energies are given with respect to the corresponding Fermi level. Supposing that $\rho_t(E)$ is constant in the energy window of interest one arrives at

$$I(V_{bias}) \propto \int_0^{eV_{bias}} \rho_s(E) T(E, V_{bias}, z) dE. \tag{1.6}$$

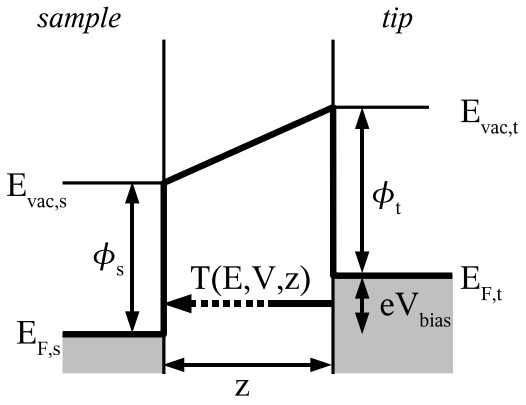


**Figure 1.2** The trapezoidal tunnel barrier, the simplest model for a tunnel barrier with applied voltage. All image potential effects are neglected. Its charm stems from the simplicity that allows for the analytical solution of several tunneling problems as for instance the transmission coefficient (see Eq. 1.13) or the FERs [20]. z is the distance between the two electrodes. The transmission coefficient $T$ is not a vectorial quantity, the arrow in the scheme indicates only the tunneling from occupied into unoccupied states.

As mentioned before, this paragraph is dealing with finite, but small voltages, which means that one can set the transmission coefficient constant. One gets

$$I(V_{bias}) = \int_0^{eV_{bias}} \rho_s(E)\, dE \cdot T(E_{F,s}, V_{bias}, z). \tag{1.7}$$

The transmission coefficient in that expression can be calculated for the 1D case in the Wentzel-Kramers-Brillouin (WKB) approximation [17] because the energies of interest are far below the maximum of the potential barrier [18] as

$$T(E, V, z) = ge^{-2K}. \tag{1.8}$$

$g$ is a prefactor that varies slowly with energy and is taken as unity. The 3D case was discussed in [19] and it turns out that Eq. 1.8 stays valid. The exponent $K$ is calculated as

$$K = \int_0^t \sqrt{\frac{2m}{\hbar^2}} \sqrt{V_{barrier}(V, z) - E}\, dz. \tag{1.9}$$

The integration limits 0 and $t$ are the turning points of the tunnel barrier. In the case of a trapezoidal barrier (see Fig. 1.2) this corresponds to the surfaces of tip and sample as long as the energy is below the work function of the sample (or of the tip for a bias voltage of opposite sign as the one depicted in Fig. 1.2). $V_{barrier}$ is the potential of the barrier in the tunnel junction.

The expression for K can be simplified by defining an average barrier potential as

$$\bar{\phi}(V, z) = \frac{1}{t} \int_0^t V_{barrier}(V, z) dz \tag{1.10}$$

$$= \frac{1}{t} \int_0^t V_{barrier}(0, z) + \frac{eV}{t} z\, dz \tag{1.11}$$

$$= \bar{\phi}_0 + \frac{eV}{2}. \tag{1.12}$$

It is important to recall that $V_{barrier}(V,z)$ is measured with respect to $E_{F,s}$. Consequenly, a positive voltage that rises $E_{F,t}$ with respect to $E_{F,s}$ increases $V_{barrier}(V,z)$. $\bar{\phi}_0$ indicates the average barrier potential without applied voltage under the assumptin of equal work functions in tip and sample. A possible contact potential between tip and sample can be included in the second term, the electric field, that contains the voltage $V$. This result can be inserted in Eq. 1.9 and leads to

$$K = \sqrt{\frac{2m}{\hbar^2}} t \sqrt{\bar{\phi}_0 + \frac{eV}{2} - E_{F,s}}. \tag{1.13}$$

This expresssion is only true for a trapezoidal tunnel barrier (see Fig. 1.2) for which $\bar{\phi}_0 = V_{barrier}(0,z)$ for $0 \leq z \leq t$. For other, more realistic barrier shapes one has to go back to Eq. 1.9 and solve it—in some cases numerically—to get the transmission coefficient. Inserting Eq. 1.13 into Eq. 1.8 and then into Eq. 1.6 leads after rearrangement of the different terms to

$$t(V_{bias}) \propto \left[\frac{8m}{\hbar^2}\left(\bar{\phi}_0 + \frac{eV_{bias}}{2} - E_{F,s}\right)\right]^{-\frac{1}{2}} \cdot \ln\left\{\frac{\int_0^{eV_{bias}} \rho_s(E)\,dE}{I(V_{bias})}\right\} \tag{1.14}$$

That means that the topography obtained in constant current mode for voltages up to approximately 0.5 V, where the transmission coefficient can still be taken as constant (see Fig. 1.3), can be interpreted as surfaces of constant integrated LDOS of the sample.

## 1.3 Scanning tunneling spectroscopy

Scanning tunneling spectroscopy is an important mean to gather informations about the electronic structure of the sample [21, 22] and consists of measuring the derivative of the tunnel current with respect to the bias voltage. Eq. 1.3 holds only for small voltages close to the Fermi level of the sample which means that only $\rho_s(E_F)$ is probed. Eq. 1.5 shows the extension for higher voltages.

Experimentally, I(V) curves are easily obtained with an STM as it was already done for mechanical break junctions (MBJ) [23] or tunneling through a thin insulating layer between semiconductors [24] or metals [25]. The only difference is the high mechanical sensitivity of the tip, that must not change during the measurement. If one supposes that the density of states in the tip was peaked at $E_{F,t}$ as

$$\rho_t(E) = \delta(E - E_{F,t}), \tag{1.15}$$

then I(V) curves would represent directly $\rho_s(E)$ (compare Eq. 1.5). But as that is an unrealistic approximation one has to get the information about $\rho_s(E)$ in another way, which are dI/dV measurements. The derivative of the tunnel current with respect to the bias voltage is, as deduced from Eq. 1.5, proportional to

$$\begin{aligned}\frac{dI(V_{bias})}{dV} \quad \propto \quad & e\rho_s(eV_{bias})\rho_t(0)T(eV_{bias}, V_{bias}, z) \\ & + \int_0^{eV_{bias}} \rho_s(E)\rho_t(E - eV_{bias})\,\frac{\partial T(E,V,z)}{\partial V}\Big)_{V=V_{bias}} dE \\ & - \int_0^{eV_{bias}} \rho_s(E) e \frac{\partial \rho_t(E - eV_{bias})}{\partial E} T(E, V_{bias}, z) dE.\end{aligned} \tag{1.16}$$

The contribution of the different terms to the dI/dV signal measured in an experiment depends on the measurement mode as described in the following sections.

### 1.3.1 Open feedback loop

The most common spectroscopy mode of the STM is the one with open feedback loop. Here, the tip is placed at a certain location on the sample and the feedback loop is disabled so that the distance between tip and sample stays constant during the measurement. When the system has stabilized, i.e. the vibrations are sufficiently damped and the piezo creep is negligible, the tunneling voltage is ramped between the given limits and the I(V) curve is recorded. The dI/dV data is obtained by a simultaneous measurement with a lock-in amplifier. Additional to the voltage ramp a modulation voltage with a frequency of about 1 kHz is applied to the tunnel junction. The resulting AC signal in the tunnel current can be detected by a lock-in amplifier the output of which can be taken as proportional to dI/dV for modulation voltages that are small compared to $V_{bias}$. The higher the amplitude of that voltage is the better is the signal-to-noise ratio of the dI/dV signal obtained but at the cost of diminished energy resolution [26]. A closer look at Eq. 1.16 reveals how this measurement can be interpreted. Several assumptions are made: First, if one works at low bias voltages (up to a few hundreds of mV) one can take the transmission coefficient as a constant with respect to the bias voltage, i.e. for changes in the tunneling barrier and with respect to E, i.e. for the different states involved in the tunnel process. This will cancel the second term in Eq. 1.16. Secondly, one supposes that the density of states in the tip is constant around the Fermi level which cancels the third term in Eq. 1.16. Finally, one sees that the dI/dV signal is proportional to $\rho_s(eV_{bias})$. This interpretation can only be misleading if inelastic processes appear in the tunnel junction [26,27] (see Sec. 4.3) or if interference between different tunnel channels cause conductance anomalies [28] like in Kondo systems.

### 1.3.2 Closed feedback loop

If one is intended to measure the dI/dV signal over a huge voltage range ($> 1$ V) one cannot work with an open feedback loop because of the restricted dynamical range of the current amplifier. Additionally, the transmission coefficient is not constant any more with respect to E and V, which does not allow any more for a simple interpretation of the dI/dV signal in terms of LDOS. The dI/dV measurement in closed feedback loop conditions is possible when the applied modulation voltage varies faster than the response frequency of the feedback circuit. Therefore the measured lock-in signal is still the same as for a measurement at fixed tip-sample distance. But one has to keep in mind, that the tip sample distance changes during the voltage ramp. However, this variation in tip-sample distance is small during the integration time of the lock-in amplifier. Hence, every spectroscopic point is an instantaneous snapshot of the differential conductance.

Fig. 1.3 shows the values calculated by Eq. 1.8 for a trapezoidal tunnel barrier where the tip-sample distance is 2 nm, the work function of the sample 4.64 eV, and the work function of the tip 4 eV. Additionally, in Tab. 1.1 some numerical values are given. Both confirm what was already supposed in Sec. 1.3, namely that the transmission coefficient stays approximately constant only for voltages of several hundreds of mV, but not for the high voltages normally used in spectroscopic measurements with closed feedback loop.

If one supposes $\rho_t$ as constant in Eq. 1.16, the differential conductance is the sum of two terms. The first is proportional to $\rho_s(eV_{bias})$ but with a weighting factor $T(eV_{bias}, V_{bias}, z)$ that increases approximately exponentially with V. The same holds for the second term that includes the derivative of $T$ with respect to $V$, which is approximately exponential, too. So both terms tend to produce an expoentially increasing differential conductance

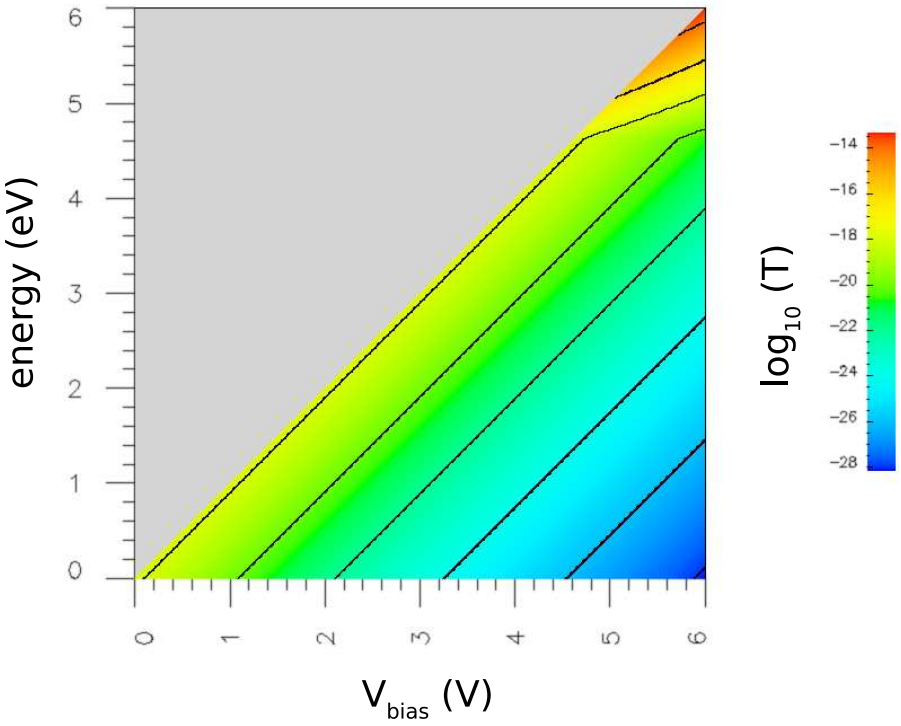


**Figure 1.3** Graph showing the change in transmission coefficient with bias voltage and energy where the logarithmic form was chosen for better comparison. The contour lines connecting points of equal $\log_{10}(T)$ correspond to the shown tick values of the colorbar. The strong increase of the transmission coefficient for voltages above the sample work function is obvious. Transmission coefficients for $E > E_{F,t}$ are not shown because no tunneling is possible for these energies in the 0 K approximation. The contour lines in the field emission regime are not perfectly equally spaced, which indicates that the decrease of $T$ with energy is not exactly exponential.

signal modulated by $\rho_s(E)$. But during an experiment with closed feedback loop the tip retreats in order to hold the current constant which decreases $T$ again. The resulting dI/dV spectrum is a superposition of the two effects. Finally, only bigger changes in $\rho_s$ will be apparent in the dI/dV spectrum as the transmission coefficient decreases very fast with increasing tip-sample distance (see Tab. 1.1). The fine structure of the sample's electronic structure is not visible due to the second term that averages out the contributions at different energies. Changes in $\rho_s$ appear most often as peaks in the dI/dV spectrum because the tip retreats to compensate for the increased density of states at the probed energy. Additionally, the transmission coefficient is decreasing fast for energies below $E_{F,t}$if one works at high voltages, which results in a dI/dV peak for a step or a peak in $\rho_s(E)$ even independent of wether the feedback loop is enabled or not. Examples are the onset of the valence and conduction band in semiconductors [22], the highest occupied molecular orbital (HOMO) and the lowest unoccupied molecular orbital (LUMO) of adsorbed molecules on surfaces [29], and the field emission resonances on surfaces probed by an STM tip [21,30]. For the latter it is very important to keep in mind the fact that the peaks of the dI/dV spectrum correspond for each of them to a different tunnel barrier characterized by $V_{bias}$ and tip-sample distance. Consequently, the Stark effect [31] has to be considered for the FERs the energy of which evolves during the dI/dV measurement.

| energy (eV) | $V_{bias}$ (V) | z (nm) | $T$ |
|---|---|---|---|
| 1.0 | 1.0 | 1.0 | $1.3 \cdot 10^{-9}$ |
| 0.5 | 1.0 | 1.0 | $3.6 \cdot 10^{-10}$ |
| 0.0 | 1.0 | 1.0 | $1.1 \cdot 10^{-10}$ |
| 0.5 | 0.5 | 1.0 | $1.3 \cdot 10^{-9}$ |
| 0.3 | 0.5 | 1.0 | $7.6 \cdot 10^{-10}$ |
| 0.5 | 0.5 | 1.1 | $1.6 \cdot 10^{-10}$ |
| 6.0 | 6.0 | 3.0 | $1.2 \cdot 10^{-20}$ |
| 5.8 | 6.0 | 3.0 | $3.6 \cdot 10^{-22}$ |

**Table 1.1** The transmission coefficient $T$ calculated for a trapezoidal barrier using Eq. 1.8. Energies are given with respect to $E_{F,s}$

.

# Chapter 2

# Field emission resonances and local work function

## 2.1 Introduction

The work function $\phi$ is a fundamental property of any metal surface. It is defined as the minimum energy that is necessary to remove an electron from the metal to infinity at 0 K. Measuring $\phi$ provides a straightforward method to monitor the state of a surface because any adsorbed species or surface defect will generally induce changes in $\phi$. This phenomenon has important consequences concerning reaction mechanisms and catalysis at surfaces because it can promote reactivity [32]. However, the work function value determined by most experimental methods is averaged over large sample areas [32–34]. This averaging happens always when the work function is probed at a distance which is large compared to the dimensions of the area of interest, because different net charges exist on neighboring areas of the sample if their work functions differ. To get the full local surface structure information, the surface potential has to be measured very close to the surface. It is then meaningful to define a local work function $\phi_{loc}$ at some point $\mathbf{r}$ close to the surface as $\phi_{loc}(\mathbf{r}) = V_{eff}(\mathbf{r})$ - $E_F$ [32], where $V_{eff}(\mathbf{r})$ is the effective surface potential felt by the electron at $\mathbf{r}$ and plays the role of a local vacuum level, and $E_F$ is the Fermi level of the sample. Spatial variations in $V_{eff}(\mathbf{r})$ at distances of the surface of the order of one nanometer should mainly reflect either local electrostatic changes in the surface dipole layer, which saturate rapidly over few Bohr radii away from the surface, or changes in the exchange-correlation potential which is also short-ranged. Local work function changes typically occur at surface inhomogeneities, e.g. at steps, impurity atoms, defects and interfaces at patches of adsorbed species.

Experimentally, local work functions have been probed in various ways. Two spectroscopic techniques take advantage of the presence of image potential states at surfaces which form a Rydberg series pinned to the local vacuum level [35]. In two photon photoemission (2PPE) [36] and inverse photoemission [37,38] experiments, image potential state energies are measured with respect to $E_F$ and the vacuum level is extracted from an interpolation of the quantum defect formula for a Rydberg series [39]. These methods opened up the possibility to extract layer dependent work functions of homogeneous adsorbed layers [40–42]. Whereas a usual photoemission experiment probes the work function averaged over the whole sample, photoemission of adsorbed xenon was a breakthrough because of the large diameter of a Xe atom and its weak bonding interaction with any substrate.

Therefore, the surface potential could be measured at about 0.2 nm in front of the surface by site-sensitive Xe atom-probes distributed over the whole surface, with a lateral sensitivity of 0.5 to 1.0 nm [32]. Kelvin probe force microscopy [43] and photoemission electron microscopy [44] have shown that contact potentials can be detected on a length scale of several tens of nm. With the close proximity between tip and sample, STM confirmed the existence of different local surface potentials at the atomic scale through apparent barrier height measurements [45]. This technique is spatially sensitive to the variations of the decay length of the electron density at $E_F$, perpendicular to the surface. In practice, the widely used 1D model of a trapezoidal barrier to approximate the tunnel barrier is a crude approximation. It neglects the tip and sample image potentials contribution and requires a determination of the tip work function to extract quantitative information about the sample work function. On the other hand, after the pioneering work of Becker et al. and Binnig et al. [30, 46] STS of FERs was recognized to be a sensitive probe to access qualitatively local surface potential changes [47–50]. However, quantitative analysis allowing local work function changes to be extracted, have not been carried out up to now from STM or STS measurements. More sophisticated STM setups that combine the STM with a photon source allow for the determination of the absolute values of the sample and tip work function [51, 52] by the detection of photoemitted electrons. But this technique suffers from a rather poor energy and spatial resolution and is therefore only rarely applied, especially given the more complicated experimental setup compared to a standard STM.

In this chapter, it is shown that low temperature STS of the FERs on a metallic surface partially covered with ultra-thin insulating layers allows for the determination of local surface potential changes and the absolute value of the adsorbate induced work function by a 1D model calculation. This method is very well suited to probe the local surface potential at any freely chosen spot on the sample. As a particular system NaCl/Ag(100) is studied. The obtained work function equals $3.2 \pm 0.1$ eV on the first three ML NaCl/Ag(100). In order to reproduce correctly the binding energies of high order FERs it is necessary to take into account the shape of the tip apex. Across the edge of a NaCl island, abrupt changes occur in the energy levels of the FERs within a 1 nm wide region where tunneling into both, NaCl/Ag(100) and Ag(100), occurs. This result yields a lateral resolution of 1 nm for local surface potential differences, which reflects the diameter of the effective emission area at the tip apex.

### 2.1.1 Experimental procedure

The Ag single crystals are cleaned by Ar sputtering and subsequent annealing. After the annealing the sample is cooled down to the wanted deposition temperature. The temperature is then stabilized by a button heater. Typical deposition temperatures are in the range from RT to 200 °C. The NaCl is thermally evaporated from a Ta crucible by resistive heating with Ta wires. The typical evaporation temperatures are in the range from 560 °C to 620 °C. Once the NaCl is well degassed, the pressure in the preparation chamber rises to $5 \cdot 10^{-9}$ mbar during the evaporation, which is due to gas emission from the Macor piece around the crucible (see Chap. 3). The sample is placed at a distance of 10–20 cm away from the crucible. The evaporation time, which is typically between 1 and 10 min, is controlled by a mechanical shutter. After the transfer of the sample to the STM [53], nice NaCl islands are observed on the sample.

All dI/dV measurements were performed with closed feedback loop (constant current mode) using the lock-in technique with a modulation voltage of 5 to 10 $mV_{pp}$ at $\sim$1.5

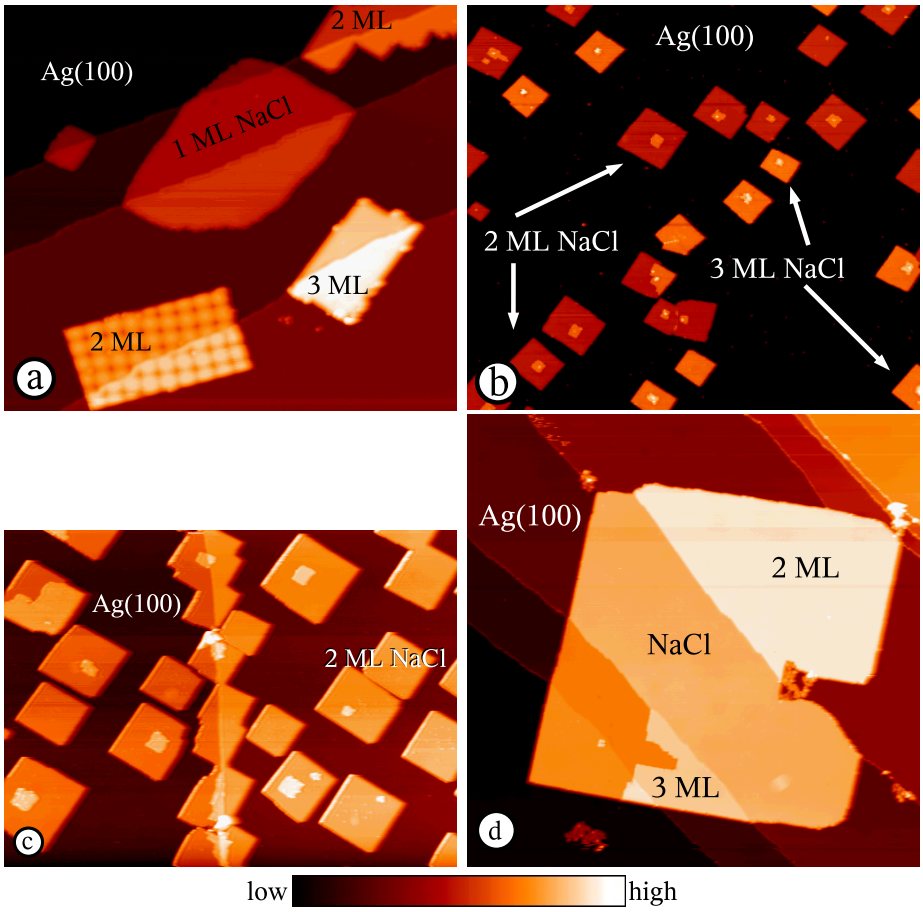


**Figure 2.1** STM images showing the NaCl islands grown with different sample temperatures during deposition. The ratio height to surface decreases with increasing sample temperature. a) In the bottom left corner a moire island is visible [55]. Sample temperature RT, 165x150 nm$^2$, $V_{bias} = 3.2$ V, $I = 20$ pA b) sample temperature RT, 500x450 nm$^2$, $V_{bias} = 4$ V, $I = 20$ pA c) sample temperature 50 °C, 500x370 nm$^2$, $V_{bias} = 4.15$ V, $I = 20$ pA d) sample temperature 200 °C, 350x350 nm$^2$, $V_{bias} = 4$ V, $I = 20$ pA

kHz with tunneling currents ranging from 20 pA to 100 pA. Simultaneously, $\Delta z(V_{bias})$, i.e. tip displacement curves were recorded. During the spectroscopic measurements on the Ag(100) substrate and on NaCl/Ag(100), care was taken of preserving identical tip conditions.

The STM experiments are performed at 5 K (liquid He) and at 50 K (solid $N_2$). The temperature dependence of the piezo displacement is corrected by the height of the substrate step heights which is for Ag(100) 204.5 pm as deduced from X-ray diffraction experiments [54].

### 2.1.2 Growth mode of NaCl on Ag(100)

NaCl layers on semiconductors or metal substrates are studied by STM in several cases. The focus lies on special aspects like a particularly rare (111) layer termination [56], attribution of the atomic resolution to the Cl ions [57], initial growth at low temperature on Ge(100) [58], special binding with the substrate [59], a work function moire for specially oriented NaCl islands [55], or the influence of NaCl overlayers on an electronic surface

state [60]. In other cases the NaCl was used as a spacer layer to separate molecules or atoms from the underlying metal substrate [61–63]. In this section the focus will lie on the growth of NaCl on Ag(100) as a function of sample temperature during deposition.

Fig. 2.1 shows NaCl islands prepared on a Ag(100) substrate hold at different temperatures. Fig. 2.1a shows a sample prepared at RT with islands of 1-3 ML thickness. Samples at RT are the only ones where the 1 ML growth is observed. These special islands are rarely found and have a different shape than the thicker islands. Their borders are round, in contrast to the straight ones of the square or rectangular islands that consist of several NaCl layers. A similar behavior is observed on Cu(311) where the 1 ML islands have partially polar and non-polar edges [59]. After completion of the first layer the following layers grow in the island mode and have only non-polar edges. In Fig. 2.1b another image on a sample prepared at RT is depicted that shows the presence of 2 ML and 3 ML islands of relatively small size. On almost all of the islands patches of the next layer are found. This behavior is still visible on Fig. 2.1c where the sample is prepared at 50 °C. The relatively small islands have all a thickness of 2 ML. Some third layer patches are visible. Going to even higher preparation temperatures, one sees on Fig. 2.1d—a sample prepared at 200 °C—that the thickness is still 2 ML with a third layer patch present. But the island size has increased strongly. The NaCl grows on Ag(100) in an island growth mode (Vollmer-Weber growth) for all substrate temperatures studied during this thesis (RT to 200 °C). With increasing temperature the ratio of the island height to the island area decreases for a given amount of NaCl deposited on the surface. Or, expressed in another way, with increasing sample temperature the covered area by a given amount of NaCl increases. That is in agreement with [64] where the authors state that no closed NaCl film can be prepared on Ag(100) and Ag(1 1 19) with thicknesses below 4 ML at RT.

The NaCl islands grow all with the exception of the moire islands [55] oriented in the same way. The (100) terminated islands [57, 58, 65] are oriented with their [110]-direction parallel to the [100]-direction of the substrate [66]. It is known from other substrates that the growth of NaCl follows the symmetry of the substrate even if the growth is not epitaxial [67]. On Ag(100) the grown islands are not all perfectly aligned with the substrate, the angles vary slightly around the expected value for perfect alignment. The angular distribution is smaller on the steps ($\pm 5°$) than on the terraces ($\pm 13°$) because the steps with the dipole due to the Smoluchowski smoothing [68] give a preorientation for the island growth [66].

The above values for the angular distribution are given for samples prepared at 50 °C. Higher substrate temperatures favor a better alignment between the NaCl islands and the substrate. The angular distribution at 150 °C is $\pm 4°$. Presumably, the higher thermal energy allows for a reorientation of partially formed islands up to a bigger size, which means that the island orientation is fixed later during the growth process. No distinction between terrace and step growth is made in the high temperature case as the islands cover more than one terrace under these growth conditions (see Fig. 2.1d). The angular distributions are in agreement with previous LEED studies [64].

## 2.2 Imaging of NaCl in STM

The astonishing fact of being able to "see" NaCl islands on STM images despite their "insulating" character—at least for the bulk case—is worth a discussion. When the tip scans over the metal surface and reaches the border of a NaCl island it should only retract in order to hold the current constant if either the LDOS in the sample increases or the

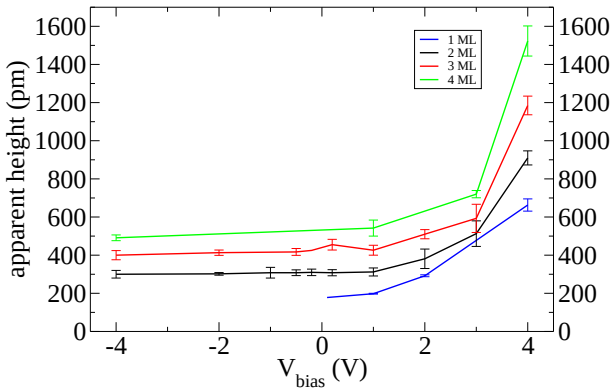


| layers | app. height (pm) |
|---|---|
| 1 ML | 180 |
| 2 ML | $310 \pm 16$ |
| 3 ML | $455 \pm 28$ |
| 4 ML | $542 \pm 42$ |

**Figure 2.2** The apparent heights of NaCl layers on Ag(100) at different voltages. The strong increase at higher voltages is due to the presence of the first FER that increases the conductance in that voltage regime. Apparent heights above 4 V are ill-defined as they depend strongly on the tip conditions. The more FERs are lying below $V_{bias}$ the higher will be the apparent height. The table gives the values for voltages close to $E_{F,s}$, except for 4 ML where the value corresponds to 1 V.

transmission coefficient increases (see Eq. 1.5).

DFT calculations [57] show that for the system NaCl/Al(100) a finite LDOS at $E_{F,s}$ exists which finally leads the authors to the conclusion that this is the reason for STM imaging of NaCl layers. Moreover, the experimental finding of imaging only one atomic species in atomically resolved STM measurements agrees with the result of the calculation that the LDOS is mainly increased on one specific site which are the Cl sites.

However, it is interesting to check how the change in apparent barrier height $\bar{\phi}_0$ (Eq. 1.12) due to the lower work function on the NaCl islands influences the measurement of a NaCl covered metal sample supposing for a moment that the NaCl layers are insulating without LDOS at $E_{F,s}$. Eq. 1.8 can be rewritten with the average barrier approximation, if $\bar{\phi}_0$ is given in eV and z in Å, in the well-known form

$$T(E_{F,s}, V_{bias}, z) = \exp\left\{-1.025\sqrt{\bar{\phi}_0}\, z\right\} \tag{2.1}$$

for small voltages $V_{bias}$.

In order to calculate the changes in tip-sample distance due to a local change of the apparent barrier height, we can already take the results of Sec. 2.6 and suppose a work function for the tip of 4 eV and for the NaCl islands of 3.4 eV. The work function of Ag(100) is taken as 4.64 eV [69]. That results in average barrier heights over Ag(100) of 4.32 eV and 3.7 eV for the NaCl covered parts in the trapezoidal tunnel barrier approximation. As $\rho_s$ in Eq. 1.6 is supposed to be constant in order to see the influence of the barrier in the present example when passing from the substrate to a NaCl island, the change in transmission coefficient has to be compensated entirely by a change in the tip-sample distance. A tip-sample distance of 10 Å over the substrate leads to $T = 5.6 \cdot 10^{-10}$. To recover that value when the apparent barrier decreases from the value on Ag(100) to the one on NaCl, the tip has to retract by 0.8 Å as calculated by Eq. 2.1. This simple calculation, while comparing with the apparent heights in Fig. 2.2, suggests that the observed apparent heights of the NaCl layers cannot be exclusively described by a decrease in apparent barrier height but that the fact of "seeing" the NaCl in STM images is indeed—at least partially—caused by an increased LDOS at $E_{F,s}$, in aggreement with the DFT calculations [57].

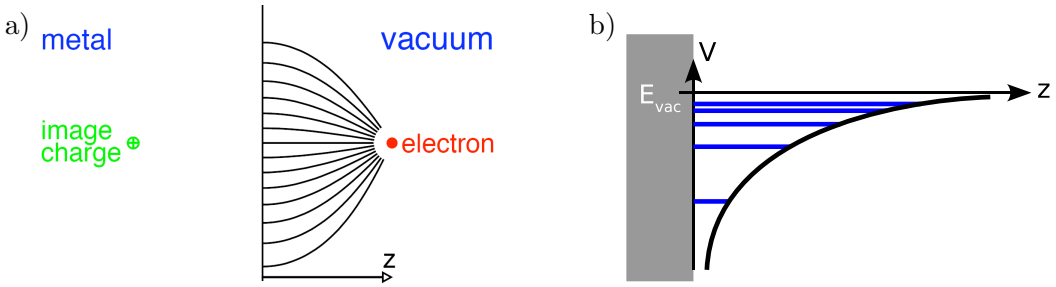


**Figure 2.3** a) The electric field distribution caused by an electron in front of a metal surface (Calculation and image by T. Fauster, Erlangen). b) The related electric potential for the electron moving perpendicular to the metal surface. The blue lines indicate schematically the energy of the image potential states.

Fig. 2.2 shows the apparent heights for the first 4 layers of NaCl on Ag(100). Two features are obvious: (i) the strong increase in apparent height for high positive voltages and (ii) the almost constant increase in apparent height for every additional layer. The first point is mainly due to the increased conductance on the NaCl islands for voltages above 3 V when one tunnels into the first FER (see Sec. 2.5). However, the apparent height starts already to rise at ∼2 V which is due to the increasing transmission coefficient with increasing voltage and probably to an increased density of states 2 eV above $E_{F,s}$ as it was found for NaCl/Al(100) [57]. The second observation is not obvious to explain but apparently the hybridization of the NaCl states with the substrate states is stronger on Ag(100) than on Al(100) where the apparent height decreases rapidly with the number of layers (280 pm, 120 pm, and 90 pm for 1 ML, 2 ML, and 3 ML, respectively [57]). However, one has to keep in mind that no precise reason is given in [57] why the first layer (280 pm) should be a monolayer. For the system NaCl/Cu(311) the apparent height per layer decreases only slightly from the first layer to the third (160 pm to 130 pm [70]).

## 2.3 Image potential states and electric field

An electron that is placed close to a metal surface experiences an attractive force towards the metal due to the polarization of the metal. Fig. 2.3a shows the resulting electric field of that arrangement. The electric potential for different distances $z$ of the electron to the metal surface is given in Fig. 2.3b. It is a Coulomb-like potential with a factor of $\frac{1}{4}$ to take into account the response of the conduction electrons in the metal to the displacement of the electron:

$$V(z) = -\frac{1}{4\pi\epsilon_0}\frac{e^2}{4z}. \tag{2.2}$$

It can be easily deduced by the method of images [71] as indicated in Fig. 2.3a. The boundary condition of the problem is that the potential at the metal surface has to be zero, i.e. that the metal surface is an equipotential surface. Placing a positive charge of equal magnitude as the one of the electron at the mirror position with respect to the metal surface fulfills the requirement as the potential is zero at all points of equal distance to both charges. Then the potential of the electron in front of the metal surface can be easily calculated by the Coulomb interaction with the image charge.

If one approximates the potential at $z = 0$, i.e. at the metal-vacuum interface, by an infinitely high barrier, the solutions for the bound states in that potential well can be

written as a Rydberg series:

$$E_n = -\frac{0.85\,eV}{n^2}, \tag{2.3}$$

where $n$ is the quantum number. These states are called image potential states. They are schematically shown in Fig. 2.3b. For real metals, where the band structure of the supporting surface affects the binding energy of the image potential states, this simple formula has to be extended by the quantum defect $a$, which has to be determined experimentally:

$$E_n = -\frac{0.85\,eV}{(n+a)^2}. \tag{2.4}$$

The reflective effect of the infinitely high barrier at the crystal side that is responsible for the confinement of the electrons in the image potential states, is realized in real metals by a projected band gap around the vacuum level. Consequently, the electron can not penetrate into the bulk. However, image potential states could be measured by inverse photoemission [72] and by 2PPE [73, 74] on substrates without a projected band gap around the vacuum level. This is possible due to the increased lifetime of the image potential states compared to the bulk states at similar energies. The reason for this lies in the relatively small overlap of the image potential states with the bulk states as their main electronic density is located in front of the surface (e.g. [75]). The intrinsic width of the image potential state with $n = 1$ on Au(111) which has no projected band gap around $E_{vac}$ lies below 100 meV (130 meV theoretically [76]), while typical intrinsic widths of noble metal bulk states around the vacuum level are around 0.5 eV [72]. STM resolved the FERs on a Au(110) surface [21], which does not have a projected band gap neither. This is a result of the lifetime effect but also from the principle of the tunneling experiment that is sensitive to the spatial distribution of electron density perpendicular to the surface, which reaches a few nanometer further in the vacuum for the image potential states than for the bulk states.

The energies of the image potential states are strongly altered by the Stark effect [31] if an electric field is applied between the metal surface and a counter electrode. An additional linear component—for the approximation of a homogenous electric field—is added to the potential of Fig. 2.3b which results for the limiting case of large electrode separations and high voltages in a trapezoidal potential curve (compare Fig. 1.2 and [20]) the origin of which lies at $E_{vac,s}$. The analytic solutions for the quantum mechanical problem of a triangular potential well, described by a potential as

$$V(z) = \begin{cases} \infty & ;z \le 0 \\ eFz & ;z > 0 \end{cases}, \tag{2.5}$$

are the Airy functions [77]. The origin for the $z$ coordinate lies at the metal-vacuum interface and $F$ is the applied electric field. The energy eigenvalues of the solutions are

$$E_n = \left(\frac{\hbar^2}{2m}\right)^{\frac{1}{3}} \left[\frac{3\pi eF}{2}\left(n+\frac{3}{4}\right)\right]^{\frac{2}{3}} \quad ;n = 0, 1, 2, \ldots \tag{2.6}$$

which is the limiting case for high $n$. For the exact eigenvalues the expression $n + \frac{3}{4}$ in Eq. 2.6 has to be replaced by a numerical factor $c_n$. It is 0.7587, 1.7540, and 2.7575 for $n = 0, 1$, and 2, respectively. It is easy to see that the approximation in Eq. 2.6 is indeed good.

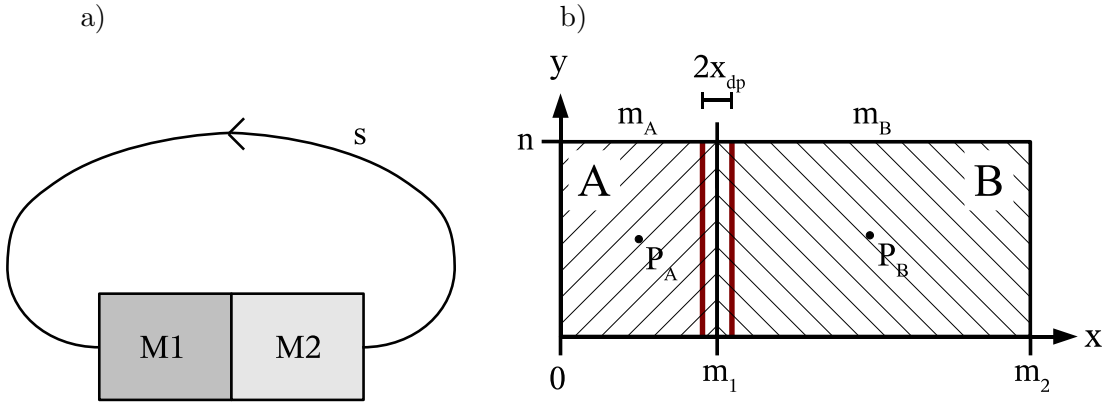


**Figure 2.4** a) Two metals with different work functions $\phi_{M1} > \phi_{M2}$ that are in contact and thermodynamic equilibrium. The black curve s follows an electric field line along which an electron is accelerated (slowed down) when brought from M1 to M2 (from M2 to M1). The arrow indicates the orientation of the electric field. b) The same situation as in a) in 2D. Areas A and B have different work functions and lie in the xy-plane. The red lines represent the dipole consisting of two line charges between the two areas.

Eq. 2.6 has two consequences. First, the image potential states are shifted to higher energies for a given electric field $F$. To include the fact of resonances in an electric field [20] in the name, the states are called field emission resonances in this context. The absolute shift in energy is higher for states with high $n$ than for states with small $n$. The energies of the image potential states evolve like $n^{-2}$ while the FERs's energies evolve like $n^{2/3}$. Consequently, the difference $n^{2/3} - n^{-2}$ is a monotonically increasing function with $n$, i.e. the higher states will show a stronger shift in energy than the lower ones for the same electric field. The second point to mention is that the higher the field is, the higher is the energy of the FERs and the further they are separated in energy. That will later in this thesis be obvious in the experiments.

## 2.4 The local work function

The work function of a metal can be defined as the energy that is needed to take an electron at the Fermi level out of the metal into the vacuum up to a distance where it does not feel anymore the influence of the image potential:

$$\phi = E_{vac,s} - E_{F,s}. \tag{2.7}$$

The crucial point is here the definition of $E_{vac,s}$. Theoretically, $E_{vac,s}$ is only well defined and fixed if one has a system where one half space is filled by the metal under consideration and the other is empty, i.e. vacuum. In more realistic cases where other objects like, e.g., a photoelectron analyser, are present, $E_{vac,s}$ will not be constant anymore but depend on the distance to the different objects. The following example will clarify this.

If two different metals M1 and M2 with different work functions $\phi_{M1} > \phi_{M2}$ are connected so that an electrical contact between both is established and thermal equilibrium is achieved (see Fig. 2.4a) then the chemical potential on both metals is the same. For the low temperature limit that means that the Fermi levels are aligned. If, in this situation, an electron is taken out from M1 the energy $\phi_{M1}$ is needed. By bringing the electron to the other side and putting it back into M2, one would gain only $\phi_{M2}$. As $\phi_{M1} > \phi_{M2}$, this

would violate the energy conservation law in thermodynamics. This is indeed impossible. In reality, the alignment of the Fermi levels is achieved by the presence of surface charges due to the work function difference between M1 and M2 (contact potential) [78–80]. In this way, the potential in the interior of the metals is adjusted so that the Fermi levels are aligned. But additionally, a macroscopic electric field in the exterior is created. By going from the surface of M1 to the surface of M2, an electron gains kinetic energy, because it is accelerated in the electric field. The gain in kinetic energy is equal to the contact potential times $e$. The potential associated with that electric field will determine the vacuum level which is now a function of position. Concerning the interface between the two metals, the contact potential manifests itself by a dipole layer at the contact area.

The same situation is present on a patchy surface where the different patches have different work functions. The only difference is that the different surface areas with different potentials lie in the same plane, i.e. the dipole layer between the two metal blocks in Fig. 2.4a becomes a linear dipole at the surface [81–84]. The consequences can be illustrated by a simple model that consists of a sample surface containing only two different areas with different work functions (see Fig. 2.4b). It consists of two surface areas A and B on a rectangular model sample.

To calculate the charge density on the surface, that is created by the contact potential between the two areas, two conditions have to be respected. First, the total charge on the sample has to be zero:

$$0 = \sigma_A A_A + \sigma_B A_B \tag{2.8}$$

$$\frac{\sigma_A}{\sigma_B} = -\frac{A_B}{A_A} \tag{2.9}$$

$$\sigma_B = -\frac{A_A}{A_B}\sigma_A, \tag{2.10}$$

where $\sigma_A$ and $\sigma_B$ are the charge densities on the two surfaces of area $A_A$ and $A_B$. Secondly, the potential difference between points on the two areas has to be equal to the contact potential.

Eq. 2.9 shows that the ratio of the areas determines the ratio of the surface charge densities in the two regions, the absolute value of which is determined by the contact potential as shown in the following. The potential at a point $P(x, y, z)$ can be calculated as

$$V_{el}(x, y, z) = -\frac{1}{4\pi\epsilon_0}\int_0^{m_1}\int_0^{n}\frac{\sigma_A\, dxdy}{r} - \frac{1}{4\pi\epsilon_0}\int_{m_1}^{m_2}\int_0^{n}\frac{\sigma_B\, dxdy}{r} \tag{2.11}$$

$$= -\frac{1}{4\pi\epsilon_0}\int_0^{m_1}\int_0^{n}\frac{\sigma_A\, dxdy}{r} - \frac{1}{4\pi\epsilon_0}\int_{m_1}^{m_2}\int_0^{n}\frac{-(A_A/A_B)\sigma_A\, dxdy}{r}, \tag{2.12}$$

where the integration runs over the whole surface (compare Fig. 2.4b for the definition of the boundaries) and $r$ is the distance of the point $P$ to an infinitesimal charge $\sigma dxdy$. For each point of the surface $V_{el}$ converges to a finite value when $z$ goes to zero. For the calculation of the contact potential the coordinates $x$ and $y$ are chosen in the middle of the corresponding area in order to minimize the influence of the neighboring area of opposite charge. On a real surface with patches of different work functions, the potential is constant over each patch except a very small transition region (dipole layer) at the interfaces. In the present model this value corresponds to $V_{el}(\frac{m_1}{2}, \frac{n}{2}, z \to 0)$ for region A and to $V_{el}(m_1 + \frac{m_2}{2}, \frac{n}{2}, z \to 0)$ for region B, if one supposes that the potential is zero far away from the surface.

$\sigma_A$ can now be determined by the second condition, the contact potential $V_{CP}$:

$$V_{CP} = V_{el}(P_A) - V_{el}(P_B). \tag{2.13}$$

By solving Eq. 2.13 one obtains $\sigma_A$ and, consequently, by Eq. 2.10 $\sigma_B$. These are the charge densities that respect the two boundary conditions imposed in the beginning of the section.

The dipole layer that separates the two regions A and B from each other is not included in the model up to here. A detailed calculation of the real dipole layer that reproduces a potential similar to a step potential between two charged surfaces would be cumbersome [82–84] but its effect can easily be illustrated in a simpler manner. The model dipole layer is depicted in Fig. 2.4b. It consists of two line charges of opposite sign with a charge density $\lambda$, centered around the interface between the two surfaces with a distance between the line charges of $x_{dp} = 0.2$ nm, which is of the same order of magnitude as the screening length in metals. It creates an electric potential at a point $P(x, y, z)$ which is calculated by

$$V_{dp}(x, y, z) = -\frac{1}{4\pi\epsilon_0} \int_Q \frac{dq}{r} \tag{2.14}$$

$$= -\frac{1}{4\pi\epsilon_0} \int_0^n \frac{\lambda dy}{r_1} + \frac{1}{4\pi\epsilon_0} \int_0^n \frac{\lambda dy}{r_2}. \tag{2.15}$$

$|\lambda|$ is taken as 1.3 $e$/nm in order not to produce a higher potential than the one created by the surface charges. The variables $r_1$ and $r_2$ are the distances of $P$ to the infinitesimal charge $\lambda dy$ on the two line charges representing the dipole.

Fig. 2.5 shows the results of the model calculation. The parameters are $m_A = 100$ nm, $m_B = 200$ nm, $n = 100$ nm, $\phi_A = 4.5$ eV, and $\phi_B = 4.0$ eV. The contact potential is therefore 0.5 V. The charge densities that correspond to that arrangement are $\sigma_A = -7.6 \cdot 10^{-4} e/\text{nm}^{-2}$ and $\sigma_B = 3.8 \cdot 10^{-4} e/\text{nm}^{-2}$. Fig. 2.5a shows the electrostatic potential $V_{el}$ along a line in x-direction at $y = 50$ nm and $z = 0.1$ nm. One sees that the transition between both regions is smooth if one considers only the contribution of the surface charges. That is due to the influence of the charges on the neighboring surface area. The transition is much more abrupt if the dipole layer between both regions is taken into account.

Fig. 2.5b shows the electrostatic potential along lines in x-direction at different distances from the surfaces. The further away one probes the potential the smoother the transition becomes until at a distance of the order of the dimensions of the areas with differing work functions almost no difference is noticeable anymore between the two regions: a common vacuum level is reached. The influence of both regions averages out at that distance as the distance $r$ of a point $P$ to both areas becomes approximately equal. At that point the model sample can not be distinguished anymore from a sample which has the average work function of the two regions present on the model sample. The lateral resolution is lost far away from the sample. This variation in electrostatic potential reflects directly the variation of the vacuum level. Far away from the surface—neglecting the influence of other objects possibly nearby—the potential reaches zero, which is called the common vacuum level [32].

This transition becomes even clearer on Fig. 2.5c where the electric potential curve is traced for the two points indicated in Fig. 2.4b as a function of $z$. The insert shows clearly that as long as $z$ is small compared to the dimensions of the charged surface areas A and B, the potential is linear as for an infinite charged surface the electric field of which is

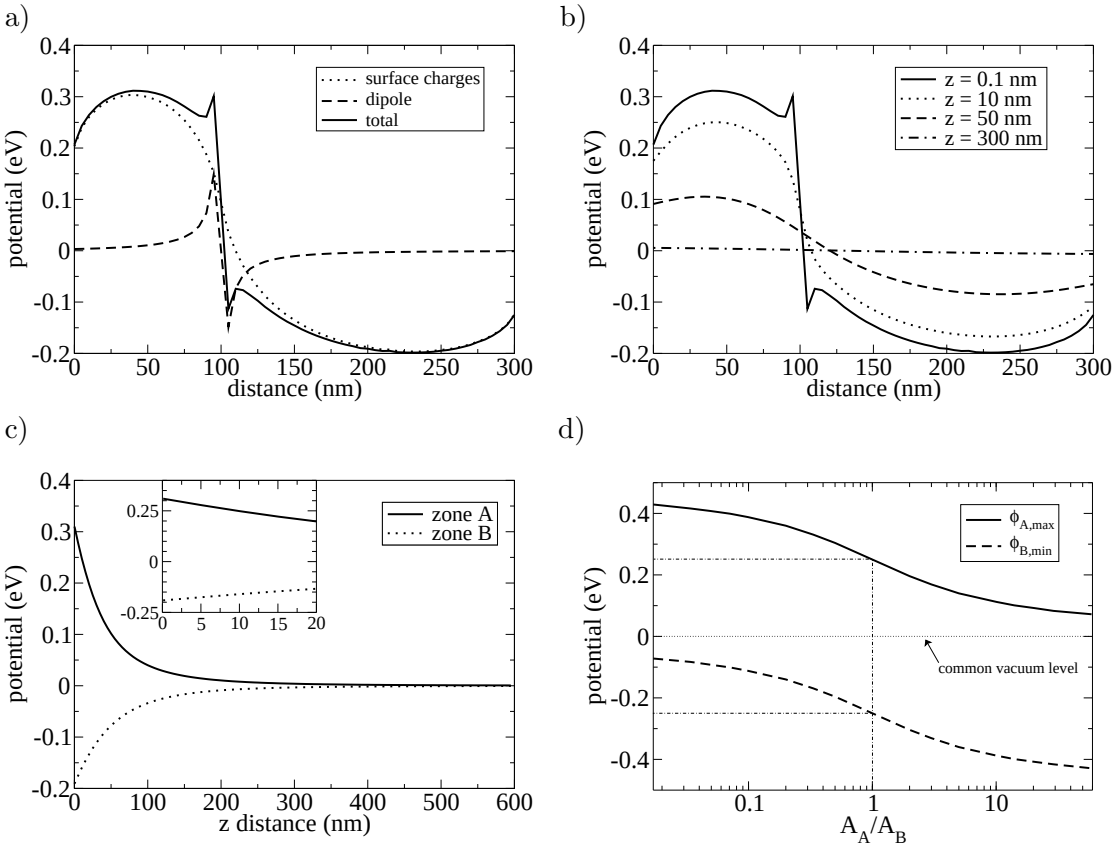


**Figure 2.5** a) The electrostatic potential along the $x$-direction on the model sample of Fig. 2.4b. The dipole sharpens the transition between the two regions considerably. b) Electrostatic potential along the same line, but at different distances from the surface. c) The electrostatic potential as a function of z. The solid line corresponds to the point marked in Fig. 2.4b on region A, the dashed line to the point marked on region B. The inset shows a zoom of the potential close to the surface. d) The electrostatic potential on the two regions as a function of area ratio. The potential of the bigger region approaches the common vacuum level with increasing ratio.

$F = \frac{\sigma}{2\epsilon_0}$ [85]. But when $z$ becomes comparable to the dimensions of the model sample the influence of the other surface sets in and the potential approaches zero, i.e. the common vacuum level, for large distances.

Fig. 2.5d shows how the maximum and minimum in curves like the dotted one on Fig. 2.5a vary as a function of the ratio of the areas $A_A$ and $A_B$. The maximum and minimum values are taken for a contact potential of 0.5 V and drawn as a function of $A_A/A_B$. If one region is much bigger than the other its potential gets closer to the value of the common vacuum level, i.e. zero, which is intuitive as for a sample without patches the common vacuum level is identical to the local one close to the surface.

Upon these considerations one can define the local work function as the energy that is needed to take out an electron of a metal up to a distance away from the surface where the influence of the image potential is not significant anymore (5-10 nm):

$$\phi_{loc} = E_{vac,loc} - E_{F,s}. \tag{2.16}$$

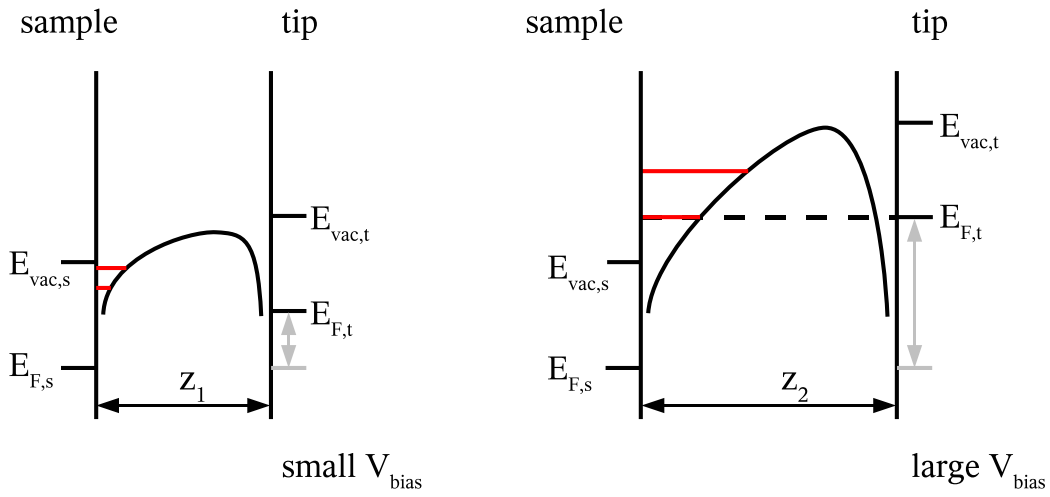


**Figure 2.6** The FERs in the tunnel junction of an STM (red lines). When $E_{F,t}$ reaches the energy of a FER a peak is observed in the dI/dV spectrum. But this is not a static procedure as the energetic positions of the FER depend on the barrier potential in the tunnel junction which changes as a function of $V_{bias}$ and tip-sample distance.

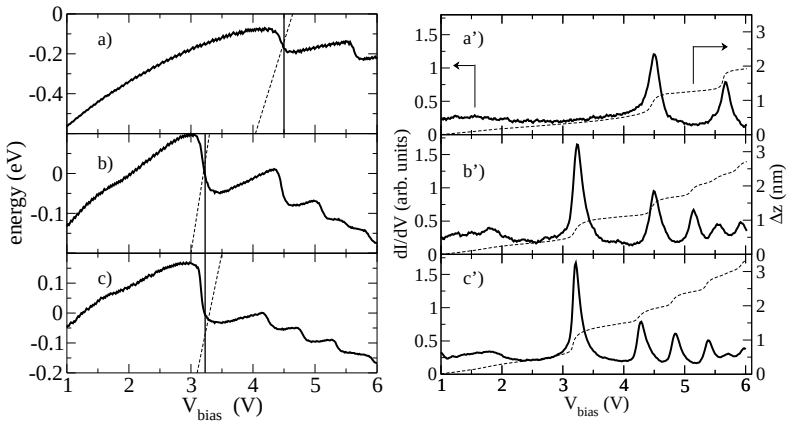


**Figure 2.7** a) Energy of the first FER as a function of bias voltage for the simulation of spectrum a', measured on Ag(100). The dashed line represents $E_{F,t}$ and the vertical line indicates the position of the first FER peak in a'. b),b') on 2 ML NaCl/Ag(100). c),c') on 3 ML NaCl/Ag(100). In each case the 0 in energy corresponds to $E_{vac,s}$.

## 2.5 Field emission resonances and dI/dV spectroscopy

The principle of the dI/dV measurement of the FERs is depicted in Fig. 2.6. It shows the situation in the tunnel junction for a low bias voltage and for a higher bias voltage where $E_{F,t}$ equals exactly the energy of the first FER. The latter configuration of the tunnel junction leads to a peak in the dI/dV spectrum as a new tunnel channel through the FER opens up. During the dI/dV measurement, the voltage is ramped between given limits. As a consequence of the enabled feedback loop the tip retracts to hold the current constant. These two effects change the potential in the tunnel junction. Hence, the energies of the FERs vary as well. With increasing electric field the FERs are shifted to higher energies

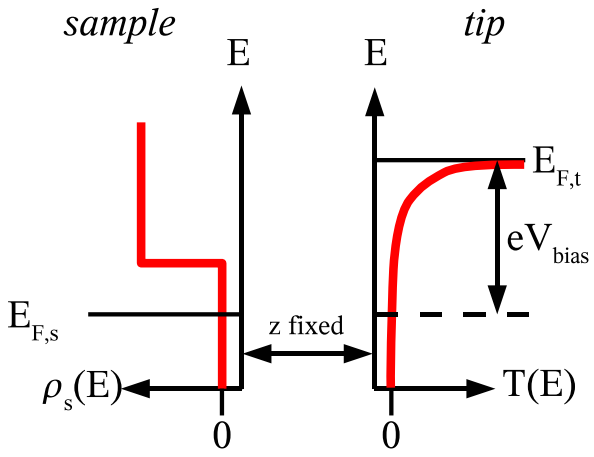


**Figure 2.8** The tunnel junction for the virtual dI/dV experiment. Thick red lines represent as a function of energy on the sample side the density of states of the FER and on the tip side the transmission coefficient. The tip-sample distance is fixed.

and spread, i.e. the energy of the FERs and the energy difference between the FERs increase. At this point it is important to note that as the FERs are located very close to the surface, $E_{vac,s}$ as denoted in Fig. 2.6 corresponds directly to the local vacuum level. That establishes the direct relationship between FERs and the local work function.

The variation of the energy of the FERs can be seen exemplarily for the $n = 1$ state in Fig. 2.7. It shows the evolution of the energy of the first FER as function of bias voltage. The curve in Fig. 2.7a corresponds to the simulation of the spectrum Fig. 2.7a' measured on Ag(100). The energy of the first FER is increasing until the first dI/dV peak is reached. There the energy drops due to the retracting tip. The dotted line represents $E_{F,t}$ ($V_{bias}$) in this energy range, which is crossing the curve at the simulated peak position and the vertical line indicates the position of the peak in the corresponding dI/dV spectrum. In the curve Fig. 2.7b, that corresponds to a spectrum measured on 2 ML NaCl/Ag(100) (Fig. 2.7b'), five peaks are included which allows for a more complete view of the behavior of the first FER during the dI/dV measurement. As an overall trend, the energy decreases with increasing voltage due to the increasing tip-sample distance after a short increase until $E_{F,t}$ reaches the energy of the first FER. This indicates that the trapezoidal barrier approximation is not sufficient to describe the tunnel junction, especially because the ratio $V_{bias}/z$ decreases during the spectrum acquisition. Fig. 2.7c, a spectrum measured on 3 ML NaCl/Ag(100), exhibits the same characteristics. The general trend is an energy decrease of the first FER with increasing voltage, contrary to what was stated in [86], where a linear increase with energy with increasing voltage is assumed.

The width of the dI/dV peak of a FER can not be smaller than 100–200 mV [87, 88] which is in the field emission regime the energy window of the tip states that contribute significantly to the tunnel current. As soon as $V_{bias}$ exceeds the work function of the sample measurements are performed in the field emission regime which means that the transmission coefficient for the states close to $E_{F,t}$ is strongly peaked. This is obvious from the change of $\log_{10}(T)$ in Fig. 1.3 for voltages above 4.64 V.

A visualization of that effect is depicted in Fig. 2.8. An imaginary dI/dV experiment is shown, that consists of the measurement of a FER with open feedback loop. The unrealistic

but very helpful assumption is that the transmission coefficient does not depend on the bias voltage but only on $E$ and can be written as an exponential:

$$T(E,V,z) = \exp\left\{\frac{E-eV}{\epsilon_1}\right\}; \quad E \leq eV. \tag{2.17}$$

The energy is given with respect to $E_{F,s}$. $\epsilon_1$ is a decay constant, that describes the decrease of $T$ with $E$. This assumption for $T$ allows for a qualitative understanding of the influence of the strongly decaying transmission coefficient on the dI/dV spectrum. As the tip retracts during the dI/dV measurement to compensate for the increase in $T$ (and the variations in $\rho_s(E)$), this assumption is also helpful to understand closed feedback loop measurements. It follows directly from Eq. 2.17 that

$$\frac{\partial T(E,V,z)}{\partial V} = -\frac{e}{\epsilon_1}\exp\left\{\frac{E-eV}{\epsilon_1}\right\}. \tag{2.18}$$

With these assumptions the dI/dV signal can be calculated as follows. If one drops the proportionality factor implied in Eq. 1.16 and sets $\rho_t$ constant and equal to 1 then one can write

$$\begin{aligned} I(V_{bias}+\Delta V) - I(V_{bias}) &= e\Delta V \rho_s(eV_{bias})T(eV_{bias},V_{bias},z) \\ &\quad + \int_0^{eV_{bias}} \Delta V \rho_s(E)\frac{\partial T(E,V_{bias},z)}{\partial V}dE. \end{aligned} \tag{2.19}$$

Dividing by $\Delta V$ and inserting Eq. 2.18 leads for small $\Delta V$ to

$$\begin{aligned} \frac{dI(V_{bias})}{dV} &= e\rho_s(eV_{bias})T(eV_{bias},V_{bias},z) \\ &\quad + \int_0^{eV_{bias}} \rho_s(E)\left(-\frac{e}{\epsilon_1}\right)\exp\left\{\frac{E-(E_{F,s}+eV_{bias}}{\epsilon_1}\right\}dE. \end{aligned} \tag{2.20}$$

Here, $\rho_s(E)$ is the density of states of the FER, supposed to be the only important influence on $\rho_s(E)$, which is taken as a step function like the one for a 2D free electron surface state. The decreasing tunneling probability into states with $k_\parallel > 0$ is neglected here, as well as the fact that the energy of the FER changes during the voltage ramp at fixed tip-sample distance (see Fig. 2.8). It is expressed as

$$\rho_s(E) = \frac{1}{1+\exp\left\{\frac{E_{FER}-E}{\epsilon_2}\right\}}, \tag{2.21}$$

where the broadening of the state is included through $\epsilon_2$. In the examples shown in Fig. 2.9 the constants are taken as $\epsilon_1 = 0.1$ eV and $\epsilon_2$ is varied as indicated in Fig. 2.9. If the broadening of the FER is larger than the width of the energy window containing the states contributing significantly to the tunneling current, no asymmetry is observed any more. The peak shape is dominated by $\rho_s$. In opposition to that, for smaller broadening of the FER the peak is asymmetric due to the peaked transmission coefficient at $E_{F,t}$.

If one compares the shape of the solid line in Fig. 2.9 with the measured spectra on Fig. 2.10 one sees an intriguing similarity. Although the assumptions for the calculation—open feedback loop, $T$ independent of $V$—do not correspond to the experiment—closed

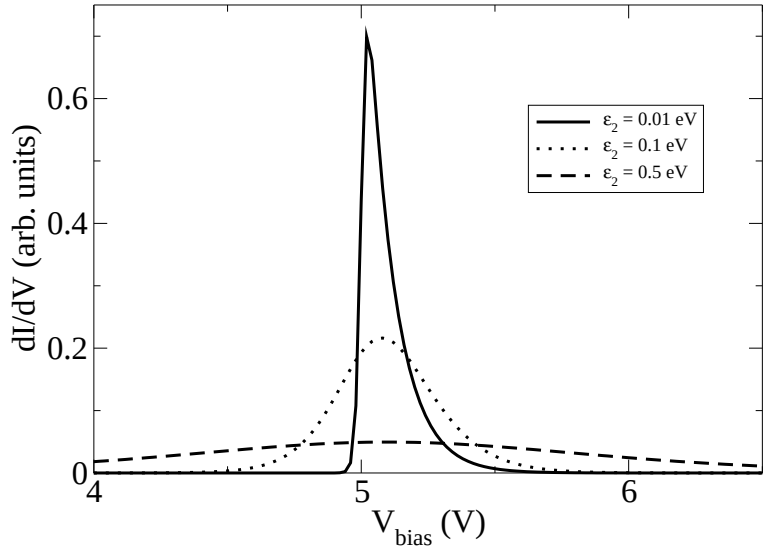


**Figure 2.9** A simulated dI/dV spectrum with open feedback loop of a field emission resonance at 5 eV above $E_{F,s}$ under the assumption that the transmission coefficient $T$ does not depend on the bias voltage. This gives an idea of the effect of the retracting tip during the measurement that compensates for the increase of $T$ with $V_{bias}$.

feedback loop, $T$ depends on $V$ and $z$—the main features of the experimental peaks are reproduced. This suggests that increase in $z$ with closed feedback loop compensates for the increase in $T$ with $V$. That means that the asymmetry in the dI/dV peaks is to a large extent due to the strongly varying transmission coefficient for energies below $E_{F,t}$ [88]. The influence of the varying tip-sample distance on the energy of the FERs (see Fig. 2.7) seems not to be big concerning the peak shape. As the FERs decrease in energy every time the tip retracts fast at a dI/dV peak, the corresponding tunnel channel remains open. Hence, no change in tunnel conductance is expected from the change in energy of the FER. Basically, the two initial assumptions made for the calculation, that are the constant $T$ with respect to $V$ and the fixed energy of the FER with $V$ approximate the peak shape of a closed feedback loop measurement, as they include both qualitatively the effects caused by the retracting tip with increasing voltage.

In Fig. 2.10, typical dI/dV spectra together with the corresponding $\Delta z$ data are presented. Prominent peaks due to the FERs are noticeable [30, 46]. Clearly visible is the difference in the voltage onset for the FERs on the clean Ag(100) and the NaCl islands. As the FERs start to appear for voltages around the sample work function [20], this large shift towards lower energy is closely related to the difference in local work functions between the two surfaces.

However, to extract the local work function difference between two different domains on the surface the following points are important and are incorporated into a simple 1D model for a quantitative description of the FER levels. (i) The image potential itself, which determines the image potential state binding energies (at zero field), is different in the two cases. (ii) For a given voltage and tip-sample distance the electric field in the junction is not the same in the two cases due to the presence of the dielectric layer. Therefore the Stark effect due to the electric field between tip and sample shifts the FERs to different energies. (iii) As $\Delta z$ varies with $V_{bias}$, the entire FER spectrum evolves upon

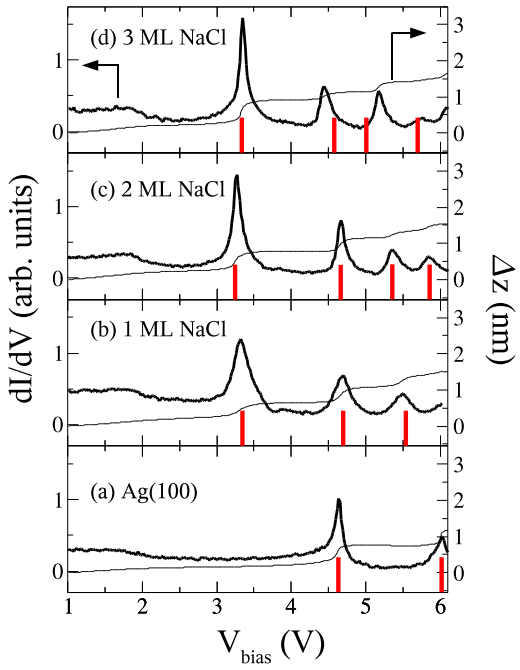


**Figure 2.10** Typical dI/dV spectra (full black line). The light black line shows $\Delta z(V_{bias})$ data, i.e. the distance the tip was retracted during the dI/dV measurement. The red bars indicate the simulated FER energies. The lower edge of the projected band gap of the Ag(100) surface is located at ∼2 V which leads to the increased conductance between 1 and 2 V. The point of steepest slope in the $\Delta z$ curves is systematically found to be ∼50 mV lower than the corresponding peak position in the dI/dV curves.

the Stark effect in a non-linear manner with $V_{bias}$ and has no simple relation with respect to the local vacuum level of the sample, in contrast to previous assumptions [86].

## 2.6 Model calculation of FERs

As the image potential states are free-electron-like for electron motion parallel to the surface but localized in the direction perpendicular to the surface, the model consists of a single particle 1D Schrödinger equation in the z direction:

$$-\frac{\hbar^2}{2m}\frac{d^2\psi(z)}{dz^2} + V(z)\psi(z) = E_n\psi(z).$$

The electronic structure of the substrate is described by a nearly free electron model [89] which reproduces the Ag(100) band gap at the known energies [69, 90] (for the surface projected band structure of Ag(100) see [91]). The corresponding NFE parameters are the amplitude of the periodic potential $V_g = 2.225$ eV, its energy level below $E_{F,s}$ $V_0 = 4.505$ eV, with a 204.5 pm period $d_{Ag(100)}$ (distance between (100) planes in the Ag bulk crystal). The Ag(100) work function is $\phi_s = 4.5$ eV, as deduced from UPS experiments performed on the same sample, which is in good agreement with the literature [92]. In the probed energy range all the observed FERs lie in the projected band gap. The electric potential between tip and sample (green in Fig. 2.12) is calculated by assuming a spherical tip apex of radius $R$.

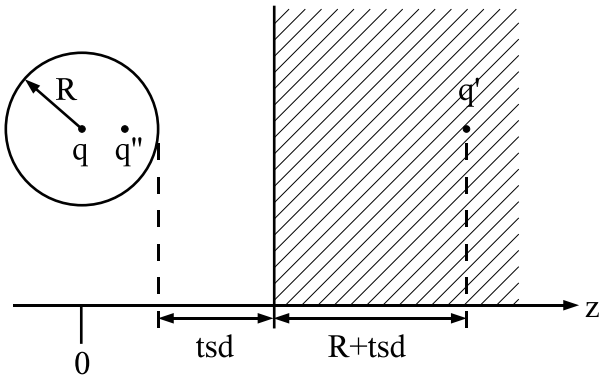


**Figure 2.11** The first set of image charges necessary to converge the potential at the sphere surface, which represents the tip, and at the substrate surface.

The electric potential between tip and sample is most easily calculated by the method of images [93]. To do so the sphere surface is set to the desired potential $V_{bias}$ by placing a charge at the center of the sphere of magnitude $q$ (see Fig. 2.11)

$$q = -V_{bias}\, R\, \frac{4\pi\epsilon_0}{e}. \tag{2.22}$$

Then an image charge $q'$ of opposite sign and equal charge has to be placed at $2(R{+}tsd)$ in order to make the substrate surface an isopotential surface ($V = 0$). Then again an image charge has to be placed inside the sphere to bring the potential on the sphere surface back to its initial value after the perturbation by $q'$. Its charge is

$$q'' = -\frac{R}{2(R+tsd)}q' \tag{2.23}$$

and its position is

$$z = \frac{R^2}{2(R+tsd)}. \tag{2.24}$$

That charge in turn perturbes again the potential at the metal surface which is not an equipotential surface anymore. The next cycle starts and the whole procedure has to be run through until the potential at the sphere and the substrate surface converges.

The calculations of the dI/dV peak positions show that the plane electrode approximation for the tip is not appropriate to describe correctly high-order FERs because the tip-sample distance is not negligible anymore compared to R. The image potential of the tip is taken into account. It is multiplied by a factor of 0.5 in order to take into account the reduced image potential due to the geometrical shape of the tip, i.e. its strong deviation from the plane electrode which is the basis for the image potential calculated by Eq. 2.2 [6, 94, 95].

For Ag(100), $V(z)$ consists of (i) the image potential of the sample with respect to the mirror plane at $z_m$ (free parameter [6, 90]), which is set constant at $z$ values where it would be below the minimum bulk potential, (ii) the image potential of the tip, and (iii) the electric potential between tip and sample.

a)

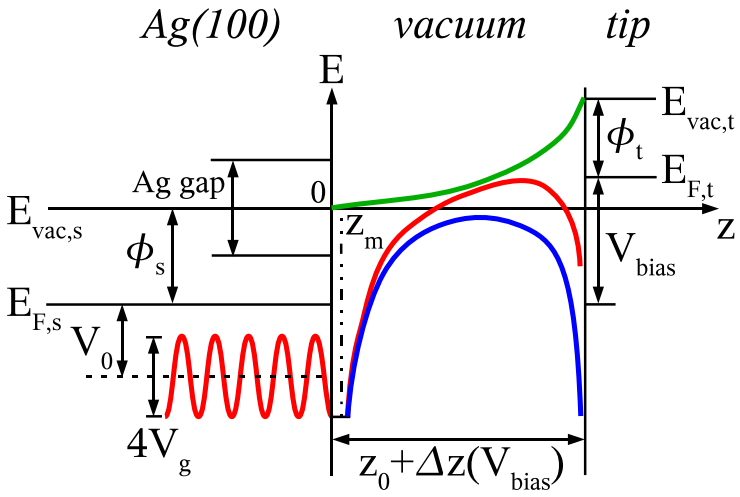


b)

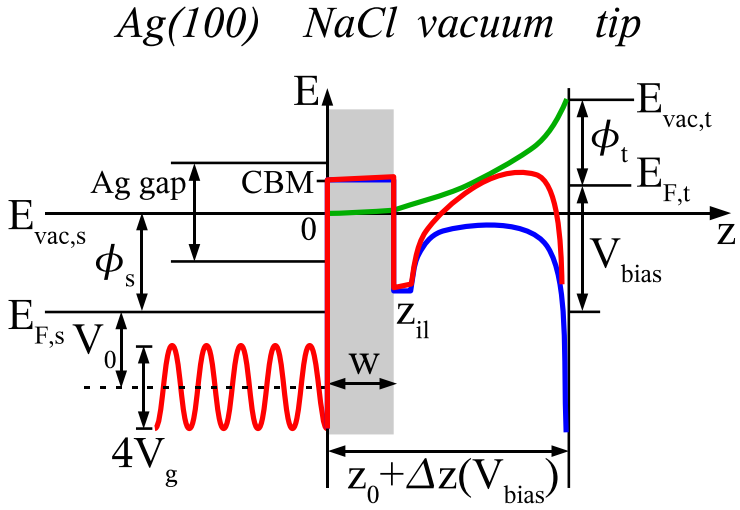


**Figure 2.12** Components of the potential $V(z)$ calculated to simulate the FER levels on a) Ag(100) and b) NaCl/Ag(100): image potential without electric field (blue), electric potential between tip and sample for an applied bias voltage $V_{bias}$ (green), sum of both components (red).

Without the electric potential, that is calculated as described above, $V(z)$ can be written as follows:

$$V(z) = \begin{cases} -\phi_s - V_0 + 2V_g \cos\left\{\frac{2\pi}{d_{Ag(100)}} \cdot \left(z - \frac{d_{Ag(100)}}{2}\right)\right\} & ; \quad z \leq 0 \\ -\phi_s - V_0 - 2V_g & ; \quad 0 < z < z_{mini} \\ -\frac{1}{4\pi\epsilon_0}\frac{e^2}{8(tsd-z)} - \frac{1}{4\pi\epsilon_0}\frac{e^2}{4(z-z_m)} & ; \quad z \geq z_{mini} \end{cases} . \tag{2.25}$$

The value of $z_{mini}$ is determined by the point where the value of the image potential of the substrate calculated with respect to $z_m$ reaches $-\phi_s - V_0 - 2V_g$.

The tip-sample distance is given by the sum of the initial distance $z_0$ (free parameter) and $\Delta z(V_{bias})$. The Schrödinger equation for the bare surface is then solved for the eigenvalues $E_n(V_{bias})$ for every $V_{bias}$ value and corresponding $z_0 + \Delta z(V_{bias})$ distance en-

| Ag(100) | |
|---|---|
| R (nm) | 5.6 (3 to 10) |
| $z_m$ (nm) | $0.015 \pm 0.004$ |
| $z_0$ (nm) | $1.17 \pm 0.07$ |
| $\phi_t$( eV) | $4.3 \pm 0.4$ |

| NaCl/Ag(100) | 1 ML | 2 ML | 3 ML |
|---|---|---|---|
| $\epsilon$ | $2.0 \pm 0.1$ | $3.2 \pm 0.2$ | $3.5 \pm 0.1$ |
| $\phi_s$ (eV) | $3.2 \pm 0.1$ | $3.2 \pm 0.1$ | $3.2 \pm 0.1$ |
| $z_0$ (nm) | $1.28 \pm 0.04$ | $1.48 \pm 0.06$ | $1.61 \pm 0.08$ |

**Table 2.1** Averaged parameters obtained by fitting the calculated FER spectra on the clean substrate and on the NaCl islands to all the measured dI/dV spectra like, e.g., Fig. 2.10. The given uncertainties correspond to the dispersion of the extracted parameters for all fitted spectra.

countered in the experiment. The condition $E_n(V_{bias}) = E_{F,t}$, i.e. $E_n(V_{bias}) = E_{F,s}+eV_{bias}$, determines the simulated FER spectrum. This first step allows us to extract $z_0$ and the tip parameters $\phi_t$ and $R$ by the best fit of the calculated FERs to all the experimental dI/dV spectra measured on Ag(100) (see Fig. 2.10 and Tab. 2.1).

The determined $z_0$ value is in overall agreement with values for typical tunneling resistances [96]. The $z_m$ value agrees well with those determined in [6, 69, 90]. The $R$ value is consistent with previous calculations [6]. The value for $R$ found in that reference equals 15 nm and is calculated for the simulation of the dI/dV spectrum showed in [46]. In their measurement, only two dI/dV peaks are found up to a bias voltage of 10 V. In our case, much more states are present in the range up to 10 V on the metal surface (see also Sec. 2.6.1), which indicates directly both a smaller tip radius and a higher tip work function.

The tip parameters $\phi_t$ and R extracted from the measurements on the bare surface are used to simulate the FER spectrum on NaCl/Ag(100). The potential is the one previously used to interpret 2PPE experiments [39, 97], extended by a term taking into account the electric potential between tip and sample [98] (see Fig. 2.12b and Appendix A). The NaCl film is modeled by a tunnel barrier with a height equal to the conduction band minimum (CBM) of bulk NaCl (0.8 eV above $E_{vac,s}$ [99]). Its thickness $w$ equals the number of monolayers multiplied by 282 pm, the distance between neighboring (100) planes in bulk NaCl. The potential in the vacuum region follows the dielectric continuum model developed by Cole [100]. It is set constant to its value at $z_{il} = w + 0.12$ nm until it reaches the mirror plane at the dielectric-vacuum interface. The only free parameters that are extracted are $\epsilon$, the dielectric constant of the NaCl layer, $z_0$, the initial distance between the tip and the metal surface, and $\phi_s$ (see Tab. 2.1).

Fig. 2.10 shows very good agreement between the measured and simulated peak positions up to 2 ML NaCl/Ag(100). For 3 ML the observed discrepancy between measured and calculated FERs points to the limits of the simple tunnel barrier model which does not take into account the microscopic electronic structure of the dielectric film [101–103] which becomes more important with increasing NaCl layer thickness. The parameter $\epsilon$ (Tab. 2.1) turns out to be smaller than the NaCl bulk value of 5.9 [104] and increases with layer thickness as confirmed by a local field model [105]. After formation of 1 ML islands the work function is found to be decreased by 1.3 eV and stays constant for additional

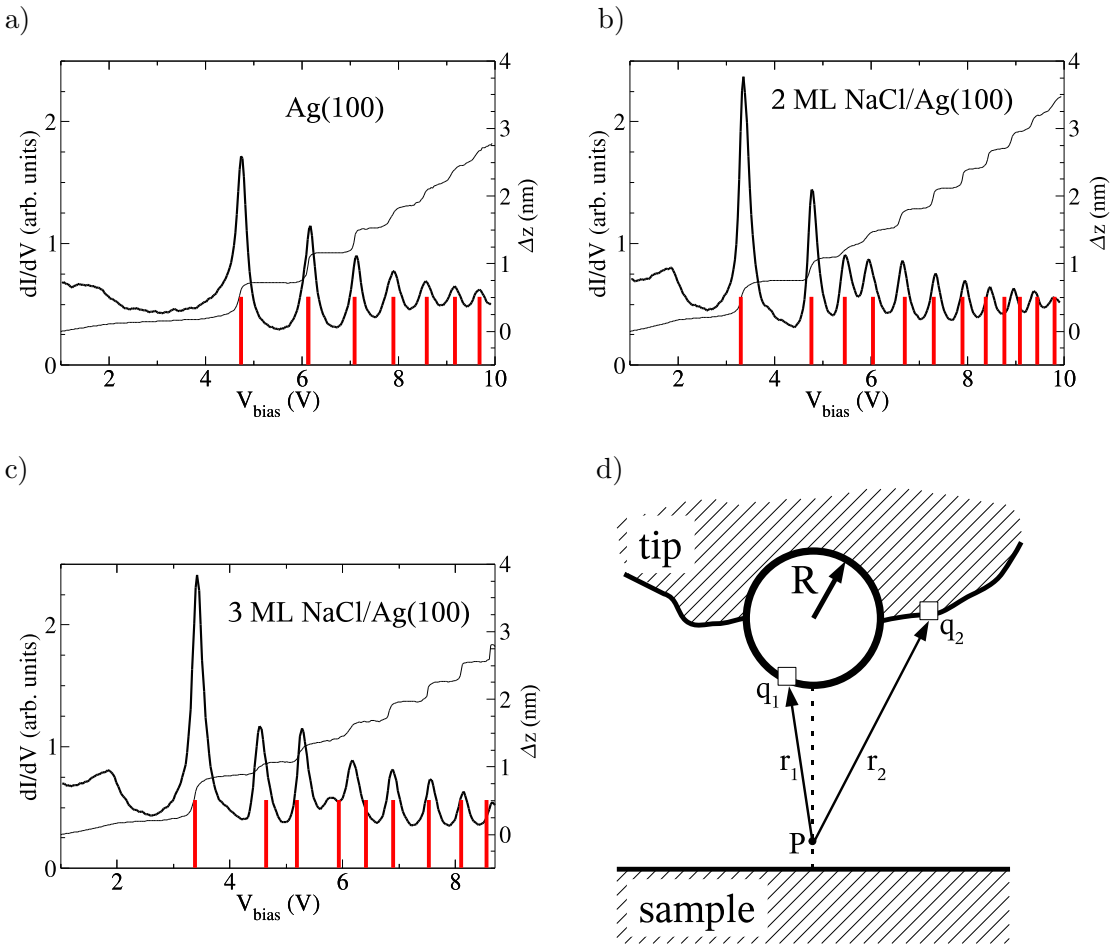


**Figure 2.13** a) dI/dV spectrum on Ag(100) simulated with the following parameters: $z_m = 0.01$ nm, $z_0 = 1.1$ nm, $R = 4$ nm, $\phi_t = 4.48$ eV. b) dI/dV spectrum on 2 ML NaCl/Ag(100) simulated with $\epsilon = 3.3$, $\phi_s = 3.2$ eV, $z_0 = 1.5$ nm. c) dI/dV spectrum on 3 ML NaCl/Ag(100) simulated with $\epsilon = 3.45$, $\phi_s = 3.2$ eV, $z_0 = 1.7$ nm. Bias voltages above 8.5 V destroy 3 ML NaCl films. d) Coulomb interaction of an electron at point P with a realistic tip.

NaCl layers. A UPS measurement of the work function as a function of the NaCl coverage yields a value of $3.5 \pm 0.1$ eV at saturation coverage. The difference of about 0.3 eV between the local STS measurement on an individual NaCl island and the macroscopic UPS measurement on a sample surface with varying morphology is ascribed to the inherent averaging over the probed sample area in UPS yielding an upper limit for the work function. The results are consistent with 2PPE results on various rare gas adlayers on Cu(100) showing that the major drop in $\phi$ occurs after deposition of 1 ML [39]. However, the reduction of $\phi$ for ionic adlayers is stronger than for rare gas adlayers where the change is below 0.5 eV [39].

### 2.6.1 dI/dV spectra up to $V_{bias} = 10$ V

Fig. 2.13a shows a dI/dV spectrum on a Ag(100) surface measured up to a tunnel voltage of 10 V. Seven peaks are visible that are well simulated with the parameters listed in the legend. Fig. 2.13b shows a dI/dV spectrum on 2 ML NaCl/Ag(100) measured under the same tip conditions as Fig. 2.13a. As the series of the FERs starts at lower voltages

due to the reduced work function, eleven peaks are measured up to 10 V bias voltage. In contrast to the case on Ag(100) the simulated dI/dV peak positions are too low for the high voltage regime above 8 V. The difference between measured and simulated peak positions increases monotonically for increasing bias voltage. Looking at the spectra Fig. 2.13a and Fig. 2.13b, one sees that the simulation works well until a $\Delta z$ value of $\sim$50% of R. That limit is most probably due to the Coulomb interaction of the tunneling electron with the tip that in reality does not consist only of a sphere but of the whole wire where the sperical apex is just a small part of it. As the simulation takes only into account the Coulomb interaction with the negatively charged sphere, the interaction with the other surface elements of the tip, that are at the same potential, is missing. That leads to a simulated electrostatic potential in the junction that is too low compared to the real one. The result are the high-order FERs lying too low in energy. As the tip-sample distance increases the interaction with the surface elements of the tip beside the apex becomes more and more important compared to the Coulomb interaction with the actual tip apex which leads to an increasing energy difference between simulation and measurement. In Fig. 2.13d the principle is depicted. The electrostatic potential at the point P is calculated by the integration over all infinitesimal surface charges $q_n$ at distances $r_n$. When the distance to the charges on the sphere (e.g. $r_1$) becomes comparable to the distance to charges on the other parts of the tip (e.g. $r_2$)—as it is the case for large tip-sample distances—then the tip cannot be approximated anymore by a simple sphere. More sophisticated approximations for the tip are needed in that case. The potential of a charged hyperboloid in front of a metal surface can be calculated analytically [106] for the case of a metallic sample. But no analytical solution to the problem of a charged hyperboloid in front of a dielectric covered metal surface is known. The problem could be circumvented by taking the sphere potential for small tip-sample distances and the hyperboloidal one without dielectric for large tip-sample distances. That is possible as the potential of a hyperboloid in front of a metal surface does almost not differ from the one of a sphere in front of a metal surface for small tip-sample distances. For large tip-sample distances (greater than $R$) and thin dielectric barrier widths (smaller than $R$) the influence of the dielectric layer on the electric field distribution in the junction becomes negligible [98] which also visible in Fig. A.5. In that case the potential can be taken as the one of the hyperboloid without dielectric. The critical point stays the treatment of intermediate tip-sample distances.

Fig. 2.13c shows a dI/dV spectrum measured on 3 ML NaCl/Ag(100). Nine peaks are visible which can be separated in two groups. The first group is formed by the first five peaks which are not perfectly simulated. That is due to the insufficient description of the electronic structure of the NaCl film which is important for these states as an appreciable part of the wave function is still in the dielecric layer. The proportion of the wave function in the dielectric layer is larger in the 3 ML case than for 1 ML or 2 ML. The higher the quantum number of the FERs, the less they are influenced by the exact electronic structure of the NaCl layer as their wave function reaches far into the vacuum. That is true for the peaks six to nine which are well simulated if one neglects the descrepancy due to the spherical model of the tip as discussed in the preceding paragraph.

## 2.7 FERs on NaCl island edges

As described in Sec. 2.4, there is a dipole layer separating the areas of different local work function on a patchy sample. To see how the FERs are influenced by that dipole layer STS measurements are performed across edges of NaCl islands.

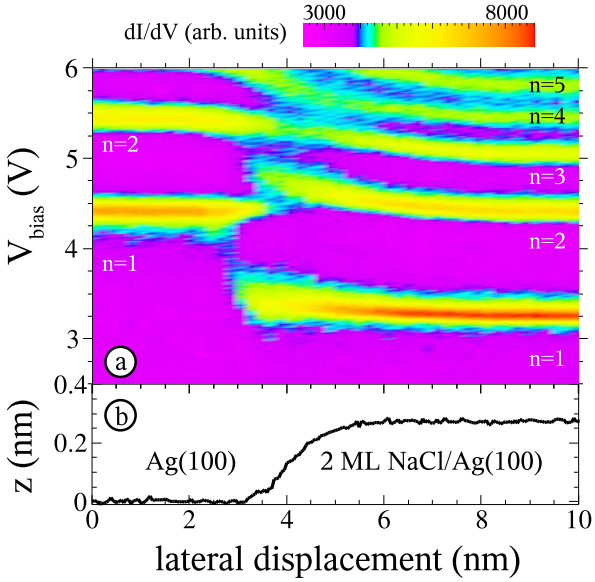


**Figure 2.14** a) dI/dV spectra taken across the step edge of a 2 ML NaCl island every 0.2 nm. b) Step profile scanned with $V_{bias} = 0.2$ V, $I = 20$ pA. The island edge is laterally offset by about 0.8 nm between topography (b) and FER spectra (a) as a consequence of the finite emission area of the tip. Note the bending of the FER energies over a length of ∼7 nm as a consequence of the local lateral contact potential.

Fig. 2.14 shows laterally resolved STS of FERs taken across the step edge of a NaCl island of 2 ML height. A discontinuous transition in the first FER energy is observed at the lateral interface between Ag(100) and NaCl/Ag(100), reflecting the lateral surface potential change on the nanoscale. The fact that transmission into the $n = 1$ and $n = 2$ FERs above both types of surfaces extends over a lateral range of 1 nm indicates an emission area of the tip apex of ∼1.5 nm$^2$, which determines the finite lateral resolution of the measurement. This value is in agreement with emission area calculations [6] when extrapolated to $R = 5.6$ nm (see Tab. 2.1).

The second feature that is visible on Fig. 2.14 is that the transition region for the first FER in the dI/dV spectra, i.e. the region where tunneling in both channels is possible at the same time, is shifted towards the Ag(100) part as visible by comparison with the profile. That can be explained by the measurement method itself (see Fig. 2.15). When the tip passes the edge of a NaCl island, coming from the NaCl and going to the Ag(100), the tip approaches the sample when it has passed the interface, i.e. the set point for a dI/dV measurement at that place lies closer to the sample than in the middle of a NaCl island. Therefore, electrons can still tunnel into FERs on the NaCl due to the finite emission area of the tip in the field emission regime and the proximity of the tip to the NaCl island surface. That is not possible when the tip is on the NaCl side of the edge as the tip is further away from the Ag(100) surface at that point. Although the tip has a finite emission area, the electrons will tunnel here mainly into the FERs on the NaCl as the tunnel barrier to the Ag(100) FERs is increased.

That can be seen on Fig. 2.15b, too. An island edge is depicted that is scanned at different $V_{bias}$. Starting at 3.3 V, the island becomes bigger—laterally as well as in apparent height—with increasing voltage. At the end, at 4.2 V, the first FER on the NaCl layer

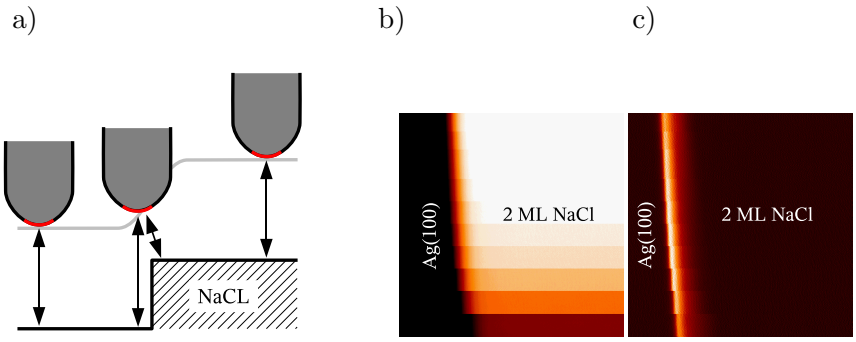


**Figure 2.15** a) Scheme of the path (light grey line) that the tip follows when it passes a NaCl island edge. Due to the finite emission area of the tip (red) transmission to the NaCl region is still possible at positions left from the actual step edge. b) Step edge of a 2 ML NaCl island scanned at voltages from 3.3 V (bottom) to 4.2 V (top) in steps of 100 mV. 22×22 nm$^2$, $I = 250$ pA. c) Derivative in $x$ direction of b).

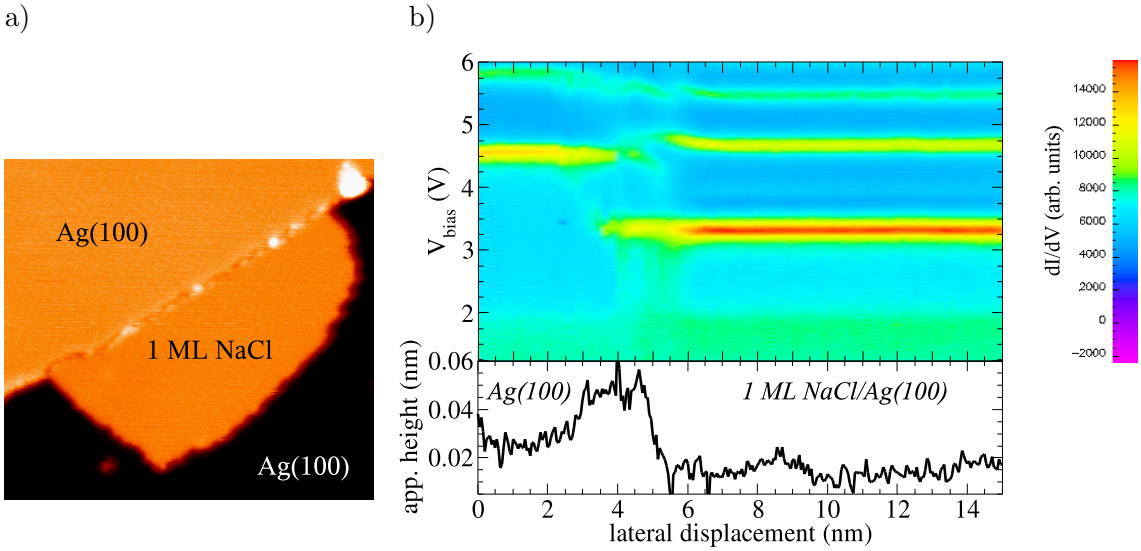


**Figure 2.16** a) STM image of a 1 ML NaCl island beside a step edge of the Ag(100) substrate. The apparent heights of a 1 ML island and the substrate terrace are almost the same. 31×29 nm$^2$, $V_{bias} = 1.0$ V, $I = 20$ pA. b) dI/dV spectra across the substrate step edge from the upper Ag(100) terrace to the NaCl island. Spectra taken every 0.2 nm. Profile scanned at $V_{bias} = 1.0$ V, $I = 50$ pA. The tip is unstable in the transition region.

is completely included in the tunneling process. As the electrons tunnel still in the FERs on the NaCl when the tip has passed the step edge (as scanned in the tunnel regime) the conductance is increased, which translates into an increased apparent height in constant current mode. That effect becomes stronger with increasing voltage as the emision area of the tip increases. On the STM image (see Fig. 2.15b) that gives the impression of a shifting edge of the NaCl island with increasing $V_{bias}$. The overall apparent height of the island increases necessarily as well.

Fig. 2.16a shows the topography STM image of a 1 ML NaCl island that is grown directly beside a substrate step without overgrowing it. As the apparent heights at low bias voltage are almost the same for a substrate step and a 1 ML NaCl island the dI/dV

spectrum can be studied without a displacement of the tip in $z$ direction due to topography changes when passing an edge. However, the profile in Fig. 2.16b shows a small bump at the interface between the two domains. The transition region for the first FER, i.e. the regime where tunneling in both channels is possible, lies on the bump of the profile. The bump is due to the Smoluchowski effect that is present to a small extent in this case due to the different geometric heights of the substrate terrace (204 pm) and the 1 ML NaCl island (282 pm). As the smoothing of the electron density reduces the local work function of the sample, the tunnel barrier is decreased, which translates in increased apparent heights in constant current STM images.

In Fig. 2.16 it is visible that there is no continuous transition between peaks of equal $n$ when going from the Ag(100) to the NaCl island. The measurement includes the first three FERs on NaCl, which permits to separate better the different peaks than in Fig. 2.14.

In [107] the scattering of image potential states at edges of Ar islands of finite size on Cu(100) are studied theoretically. The authors conclude that the image potential states on the islands are very efficiently scattered toward the continuum of image potential states on the clean substrate, leading to very broad states on small (diameter $\sim 5$ nm) islands. But as the authors suppose an aligned vacuum level on the whole sample, and therefore no dipole layer separating the islands from the clean substrate, this conclusion is not a definitive one. As the local work function on the Cu(100) ($\phi = 4.64$ eV [39]) substrate is higher than the one on 1 ML Ar/Cu(100) ($\phi = 4.38$ eV for a complete layer [39]), the scattering of image potential states on Ar islands towards image potential states on the substrate is restricted to states with $n \geq 2$ (as deduced from the binding energies for a complete Ar layer) on the islands that can be scattered toward the continuum of the $n = 1$ state of Cu(100) if one considers only energy conservation and not the probability for scattering processes at the dipole layer.

The scattering of the FERs is probably the reason why peaks of equal quantum number $n$ do not form continuous transitions in Fig. 2.14 and Fig. 2.16b. When the dI/dV measurement is done at a place where the dipole layer changes the local vacuum level the FER peaks are shifted—the NaCl peaks toward higher voltage and the Ag(100) peaks toward lower voltage. The decaying signal intensity for the dI/dV peaks towards the interface between the Ag(100) and the NaCl island is then due to a decreasing overlap of the tip emission area with the region where FER still has a non-zero probability density. Apparently, in the interface region with its strong surface potential change on a short distance, no FERs are present.

The fact that the peaks of the FERs with higher $n$ start to shift further away from the interface as the peaks with small $n$ is due to the higher sensitivity of the high-$n$ FERs to changes in the electric field, which is altered by the dipole layer (see Sec. 2.3).

## 2.8 Smoluchowski effect and FERs

The Smoluchowski effect [68] describes the smoothing of the electron density at edges of a metal crystal. That can be for instance at the step edges of a surface where the change in LDOS can be detected by dI/dV spectroscopy [108]. As the electron density has not the same spatial distribution in a unit cell at a step at the surface as in the bulk a dipole is created that lowers the local work function [109]. This local work function change can be followed by STM with apparent barrier height measurements [110]. But it can also be detected by FERs using dI/dV spectroscopy or the change in conductance visible in constant current STM images.

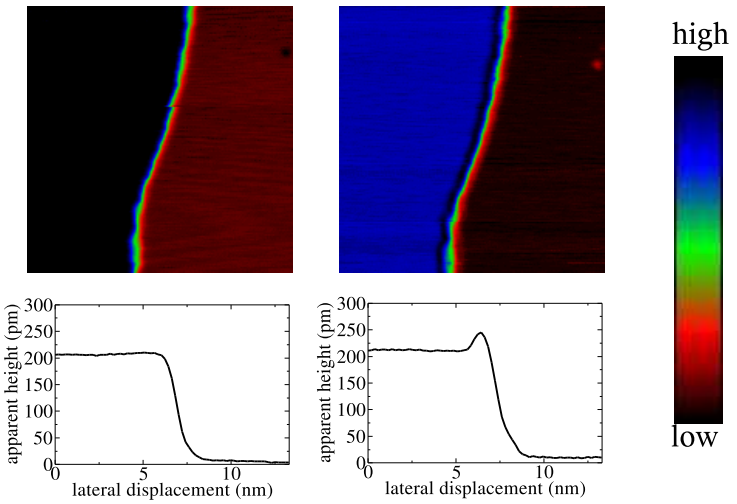


**Figure 2.17** A Ag(100) substrate step edge scanned at $V_{bias}$ = 2.0 V (left) and at $V_{bias}$ = 4.0 V (right). 34×34 nm$^2$, $I$ = 20 pA. The color scale is shown to the right. In the lower panel the corresponding profiles across the step are shown. Additionally to the Smoluchowski effect at the step the FER show also a contrast inversion at the impurity in the upper right corner indicating a reduced surface potential at that place. That is in agreement with the hypothesis that impurities most often reduce the work function of metals as most impurities are more electronegative than a metal which means that a work function increasing dipole layer is formed.

Fig. 2.17 shows the latter case. A Ag(100) step edge is scanned at 2.0 V and at 4.0 V bias voltage. The profile of the step shows clearly an increased apparent height at the step site when scanned at 4.0 V. That is due to the fact that at 4.0 V the first FER contributes already partially to the tunnel current which increases the conductance, i.e. the apparent height.

Fig. 2.18 shows several dI/dV spectra taken across a substrate step edge covered by a 2 ML NaCl island. On the step the first and second FER are shifted to lower voltage (by $\sim$ 0.1 V for the $n = 1$). The peak intensity becomes weaker. As the FERs are bound to the local vacuum level, the decrease in voltage is attributed to a decrease in local work function. The Smoluchowski effect takes place at the substrate step edges below the NaCl as the NaCl overgrows substrate step edges in the carpet mode [111] and therefore does not show any sharp step. As the change in voltage of the first FER is small it could also be a change in binding energy but there is no obvious reason why the image potential in front of a step should be altered as the polarizabilities of the substrate and the NaCl do not change.

## 2.9 Comparison with photoemission

### 2.9.1 Work function determination with photoemission

The work function of a sample can be determined by photoemission with the "low energy threshold" method [32, 112]. A complete photoelectron spectrum is recorded, i.e. the intensity distribution of the electrons from the Fermi level down to the low kinetic energy

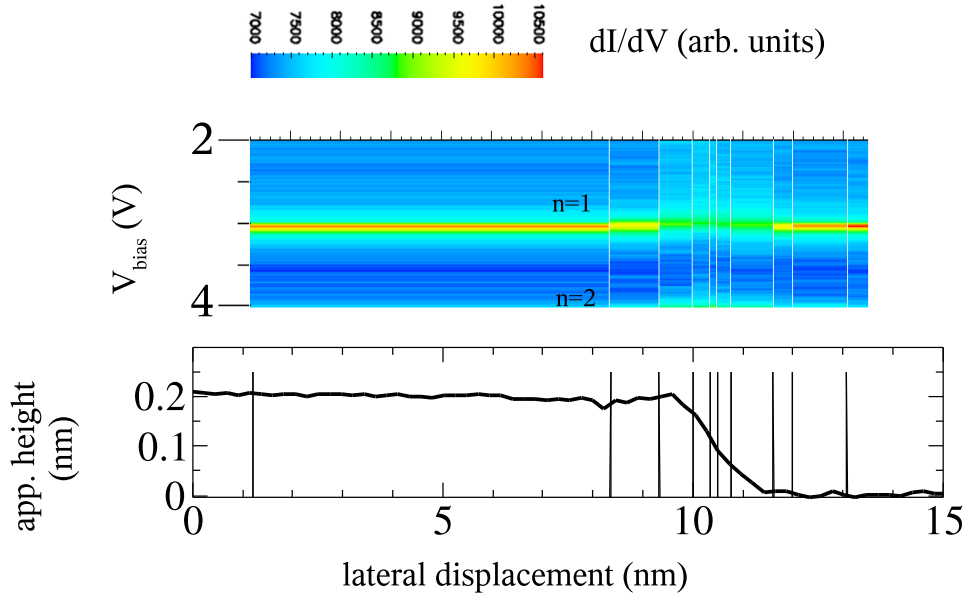


**Figure 2.18** dI/dV spectra across a substrate step edge under a 2 ML NaCl island. The vertical lines in the profile ($V_{bias} = 2.0$ V, $I = 20$ pA) are the positions where the spectra were measured. The shift of the FERs due to the work function lowering by the Smoluchowski effect is obvious.

threshold. The work function $\phi$ determined in that way is calculated by

$$\phi = h\nu - \Delta E, \tag{2.26}$$

where $h\nu$ is the photon energy and $\Delta E$ is the width of the photoelectron spectrum from $E_F$ to the low kinetic energy threshold. Here, it is supposed, before entering a more thorough discussion in the second part of this section, that there is no applied voltage on the sample and that the work function of the electron analyzer is $\phi_{far}$, i.e. the vacuum level of the analyzer is aligned with $E_{vac,common}$. Otherwise the applied voltage and the contact potential with the electron analyzer would create additional electric fields. The electrons that arrive at the electron analyzer are the ones that have just enough energy to overcome the common vacuum level of the sample as the analyzer is far away from the sample compared to the sample dimensions. In the case of a clean sample showing only one crystal facet the common vacuum level corresponds to the work function of that facet (neglecting the effects of the other parts of the experiment electrically connected with the sample, which is justified in the second part of this section). In the case of a sample that consists of different patches with different work functions the situation is different. The local surface potential as introduced in Sec. 2.4 of the different patches influences the potential far away from the surface. The common vacuum level $E_{vac,common}$ is then [33]:

$$E_{vac,common} = \sum_i f_i e V_i, \tag{2.27}$$

where $f_i$ is the fraction of the sample surface that is covered by patch $i$ and $V_i$ is the corresponding surface potential of that patch. As the surface potential plays the role of a local vacuum level, a similar equation holds for the work function of the sample far away

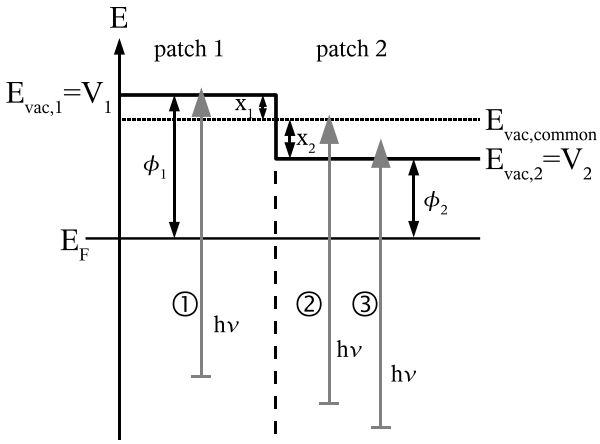


**Figure 2.19** Two patches of different work function on a sample. The numbers 1 to 3 denote electrons at different energies excited by a photon of energy $h\nu$.

from the surface $\phi_{far}$ relating it to the local work function of the patches $\phi_{i,loc}$:

$$\phi_{far} = \sum_i f_i \phi_{i,loc}. \tag{2.28}$$

The electrons leaving the sample are accelerated or slowed down on their way to the analyzer depending on the local work function (see Fig. 2.5c). The electrons arriving at the detector with the lowest kinetic energy are the ones that just come over the common vacuum level. That means that the work function measured in photoemission and determined by Eq. 2.26 is the one averaged over the whole sample and given by Eq. 2.28.

Fig. 2.19 shows the situation in the photoemission experiment. Two regions on a sample are depicted with different work functions $\phi_1$ and $\phi_2$. Electrons at three different energies are excited by a photon $h\nu$. The first one is excited and leaves the surface on patch 1 with almost zero kinetic energy. But while going to the analyzer it is accelerated by the electric field acting on it and gains the kinetic energy $x_1$ at a distance away from the surface comparable to the sample dimensions. A second electron is excited and leaves the surface at patch 2. Its kinetic energy when right in front of the surface is $\sim x_2$. But it will loose the kinetic energy $x_2$ when going to the analyzer as the retarding field slows it down. Those electrons are the ones that are measured at the low kinetic energy photoyield threshold. They come from patches the surface potential of which lies below the common vacuum level and leave the surface with a kinetic energy of $E_{vac,common} - V_i = x_i$. A third electron is excited and leaves the surface at patch 2 with a finite kinetic energy which is below $x_2$. This electron has not enough energy to reach the analyzer as it is repelled at the common vacuum level.

Up to here, the common vacuum level is seen as the one of the sample but as the analyzer is far away from the sample surface compared to the sample dimensions, the surrounding parts like sample holder etc. influence the common vacuum level, too. That problem is solved by applying a small voltage on the sample, as discussed in the following.

In a practical photoemission experiment the sample is negatively biased by several volts ($\sim$10 V) in order to detect all the electrons, even those that would have zero kinetic energy in the detector without an applied electric field and to separate them from the secondary electrons. That creates a Schottky-type barrier at the surface as shown in Fig. 2.20a. The

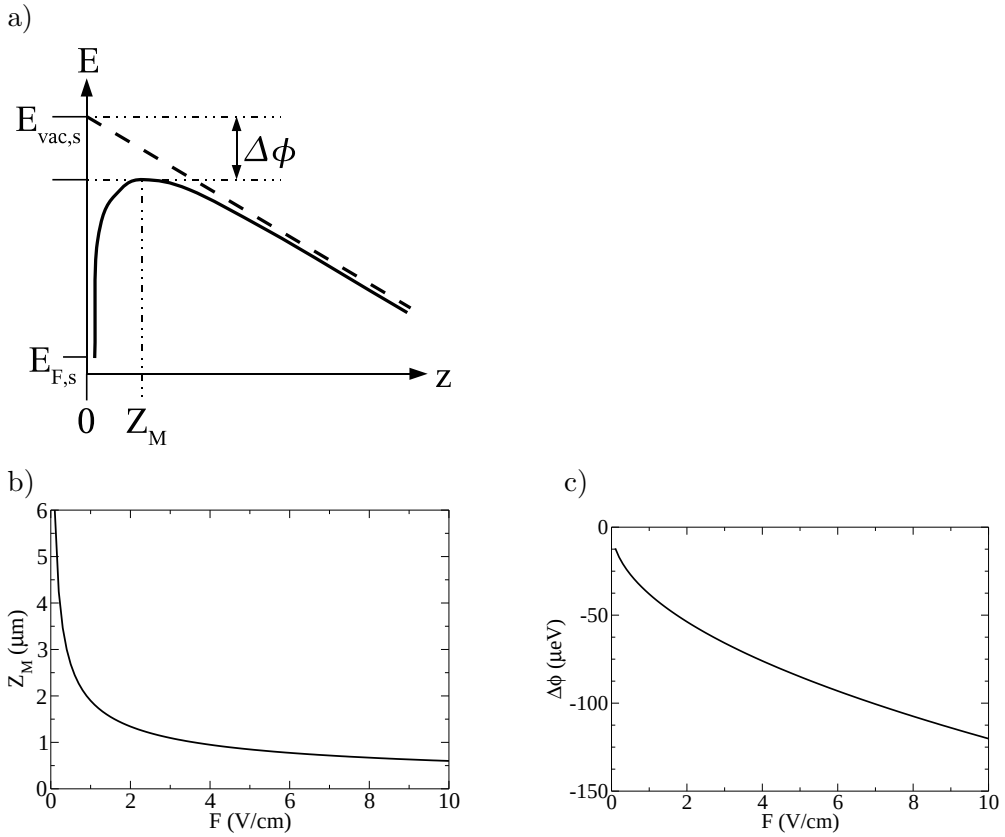


**Figure 2.20** a) The Schottky barrier created at a metal surface by an applied electric field. b) The position of the energy maximum $Z_M$ as a function of the electric field. c) The work function decrease $\Delta\phi$ as a function of the elecric field.

applied electric field $F$ bends the surface potential in a way that a maximum appears at $Z_M$. This maximum lies lower than $E_{vac,s}$ which means that the work function of the sample is decreased by $\Delta\phi$. If the surface potential is approximated by the sum of the image potential and the electric potential then $\Delta\phi$ is calculated as

$$\Delta\phi = -\sqrt{\frac{e^3 F}{4\pi\epsilon_0}}. \tag{2.29}$$

Fig. 2.20c shows the work function decrease as a function of field strength where the range for $F$ covers the typical values for a photoemission experiment. The work function decreases under the influence of the electric field only by a value in the $\mu e$V range, which is negligible for practical considerations. The position $Z_M$ of the maximum is calculated as

$$Z_M = \sqrt{\frac{e}{16\pi\epsilon_0 F}}. \tag{2.30}$$

Fig. 2.20b shows $Z_M$ as a function of electric field. It lies several $\mu$m in front of the sample surface for the typical electric fields used in photoemission experiments. That has an important consequence on the interpretation of the experiment. Fig. 2.21a shows the surface potential for a sample where the irradiated area is homogeneous concerning the work function. Every point in the area has the same work function $\phi_1$. To calculate the work function from the data of a photoemission experiment, $\Delta E$ of Eq. 2.26 is needed

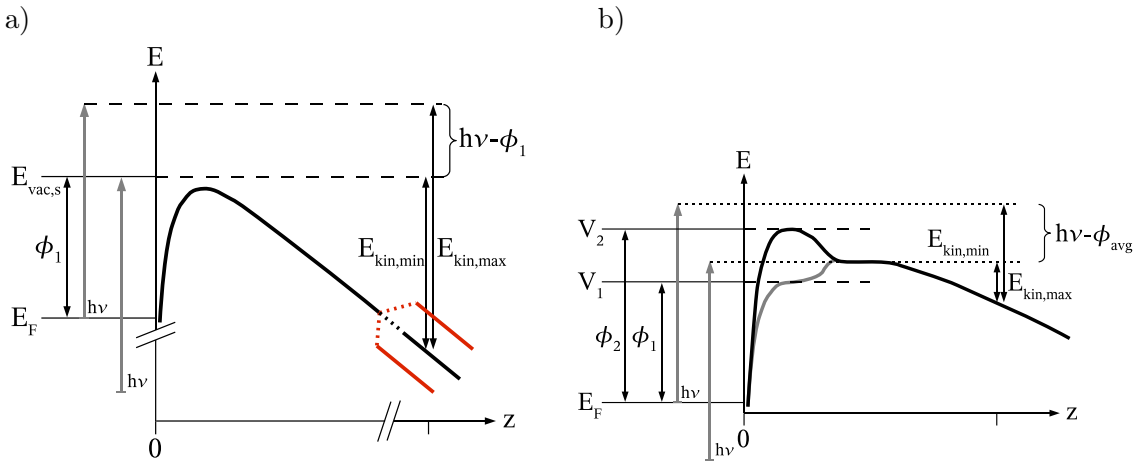


**Figure 2.21** a) The Schottky barrier at a metal surface. At distances from the sample surface comparable to the sample dimensions the common vacuum level is influenced by the other parts electrically connected with the sample, like e.g. the sample holder. Depending on their work function the common vacuum level lies either above or below (red lines) the common vacuum level of the sample alone (black line). The value of $\Delta E$ is not affected by this. b) The surface potential of a sample exhibiting two different types of patches with different work functions. The average work function is measured as long as the patches are smaller than $\sim$1 $\mu$m because then $Z_M$ lies further away from the sample surface as the point where the two surface potentials join to a common vacumm level. (The photon energies are not drawn at scale)

which is the difference between the highest kinetic energy $E_{kin,max}$ measured in the electron analyzer and the lowest kinetic energy $E_{kin,min}$. The electrons at $E_{kin,max}$ are the ones excited from $E_{F,s}$ and the electrons at $E_{kin,min}$ are the ones that just overcome the Schottky barrier which has, as shown in Fig. 2.20c, approximately the same height as the work function $\phi_1$. That means that the work function of the sample is calculated as

$$\phi_1 = h\nu - (E_{kin,max} - E_{kin,min}). \tag{2.31}$$

In that way the applied electric field, that is often only mentioned in the context of avoidance of secondary electrons of the spectrometer (see e.g. [113]), makes the measurement local, i.e. specific to the sample. The surface potential that has to be overcome has its maximum at a distance of several $\mu$m of the surface. That means that all other parts electrically connected with the sample, like the sample holder etc., that almost never have the same work function as the sample, do not influence the measurement of the work function. The effect of the present contact potentials that influence the common vacuum level far away from the surface is eliminated by taking the difference between $E_{kin,max}$ and $E_{kin,min}$. In Fig. 2.21a, the red lines indicate alternate possible potential curves far away from the surface, that both do not change the work function measurement on $\phi_1$ as only the difference $E_{kin,max} - E_{kin,min}$ is important.

In Fig. 2.21b the surface potential for a sample is shown that has two different types of patches inside the irradiated area with work functions $\phi_1$ and $\phi_2$. The size of the patches is supposed to be smaller than 1 $\mu$m which means that the surface potentials of the two different types of surface merge into a common vacuum level at a distance below 1 $\mu$m, i.e. before the maximum of the Schottky barrier is reached. In this case, photoemissin does not allow to discriminate between the two different work functions. Instead, the average work function $\phi_{avg}$ of that area is measured, corresponding to the difference between $E_{F,s}$ and the surface potential several $\mu$m in front of the sample surface.

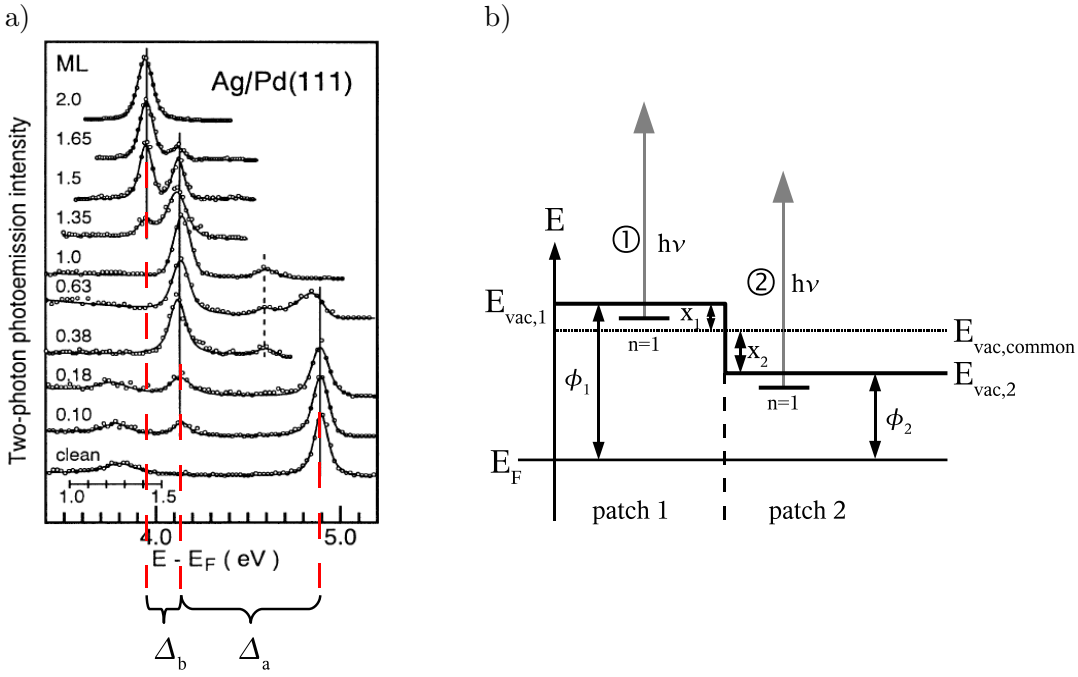


**Figure 2.22** a) The 2PPE peak intensities reproduced from [42]. $\Delta_a$ is the work function difference between Pd(111) and 1 ML Ag/Pd(111) minus the binding energy difference. $\Delta_b$ is the same for 1 ML Ag/Pd(111) and 2 ML Ag/Pd(111). b) The energy diagram for the image potential states on two patches with different work functions in 2PPE.

In [48] the energy of the first FER on benzene/Cu(111) was measured by STS as a function of coverage. But the full local character of STS was not used because the spectroscopic measurements were averaged over zones of a defined nominal benzene coverage without distinguishing the local environment, i.e. wether the spectroscopy measurement was done on a molecule or on the substrate. Due to the averaging process the results are then similar to usual photoemission work function measurements. STS would have allowed to determine the surface potential changes as a function of distance of an adsorbed benzene molecule. That quantity is independent of the coverage for low coverages and characterizes the surface locally.

### 2.9.2 2PPE

2PPE is used to study unoccuppied states of metals or semiconductors. Due to their relatively long life time [114, 115], and therefore small linewidths, image potential states at surfaces are ideally suited for the method. Being located close to the surface, they form a Rydberg series toward the local vacuum level which makes them a sensitive tool to study surface potential changes. These differences in surface potential—most easily introduced by a different number of layers of an adsorbate—are detectable by 2PPE on a single sample [34, 42, 116–119] exhibiting areas of different work functions.

In [42] the image potential states on different number of Ag layers on Pd(111) are studied. In Fig. 2.22a the 2PPE intensities are reproduced. The series of image potential states belonging to a certain coverage are easy to distinguish. Their energies with respect to $E_{F,s}$ differ by the contact potential as they are bound to their corresponding local vacuum level. A small deviation from the contact potential is introduced by the different

binding energies with respect to $E_{vac,s}$ on the different substrates domains. Fig. 2.22b shows how the kinetic energy of the electrons is related to the local work function on the sample. That link is important as in 2PPE kinetic energies are measured in order to deduce the energy of the image potential states with respect to $E_{F,s}$. To the left in Fig. 2.22b the energy levels on a patch with a work function $\phi_1 > \phi_2$ is depicted. $\phi_2$ is the work function of patch 2. When both image potential states $n = 1$ are populated by a first photon $h\nu$ they are probed by a second photon of energy $h\nu$ which is the situation depicted in the figure. Close to the surface both electrons have the same kinetic energy as they are excited by a photon of the same energy and as they are at the same energy below the corresponding local vacuum level (neglecting for a moment the different binding energies with respect to $E_{vac,s}$ on different domains). But on the way to the electron analyzer the electron coming from patch 1 gains the kinetic energy $x_1$ when it is far away from the sample. Here, it is supposed again as in the beginning of the preceding section that there is no applied voltage between the sample and the electron analyzer and that the electron analyzer has the work function $E_{vac,common} - E_{F,s}$ to avoid confusion with additional electric fields. In contrast to the first electron, the electron coming from patch 2 looses the energy $x_2$ when it is far away from the sample. That means that the electron 1 arrives at the analyzer with a kinetic energy of $x+x_1$, where $x = h\nu - E_1$ ($E_1$ is the binding energy of the $n = 1$ image state). Electron 2 arrives with the kinetic energy $x - x_2$. The difference of both is $(x + x_1) - (x - x_2) = x_1 + x_2$, the work function difference, as indeed found in the experiment. That means that 2PPE is sensitive to local surface potential changes as it can probe image potential states that are bound to the local vacuum level. The precondition for these measurements is an ordered layer growth, because the areas of interest should cover a significant part of the probed sample in order to get a signal. Otherwise the evolution of the image potential state energies as a function of coverage is difficult to explain as for instance for Na/Cu(111) [120, 121]. That case should be easy to study by STM as the local surface potential can be probed at any arbitrary place on the sample with this method.

### 2.9.3 PEEM

PEEM is a tool to monitor spatially and time resolved local work functions on a sample [122]. The method consists of a sample that is irradiated by ultraviolet light from which electrons are emitted which are then detected on a screen. The electrostatic lenses that guide the electrons from the sample to the phosphor screen fulfill two functions. First, they accelerate and guide the electrons to the screen in order to produce an image of the sample. But, secondly, by the strong electric field (tens of kV on a few mm) that is applied, they allow for the distinction between areas of different work function on the sample, which is called the Schottky effect [123, 124]. Fig. 2.23 shows the principle.

In Fig. 2.23a the surface potential of two patches 1 and 2 with different work functions $\phi_1$ and $\phi_2$ is depicted for the case of zero applied field. Electrons coming from different patches on the sample reach all the common vacuum level at a distance far away from the sample. At this point no distinct statement about the origin of the electrons is possible anymore, the information about the local work function is lost.

In Fig. 2.23b the same situation is shown with a strong applied electric field polarized in a way to "pull out" the electrons of the sample. The surface potential looks now very different for the two patches. In both cases the potential related with the electric field has to be added to the surface potential shown in Fig. 2.23a. But in the case of patch 1

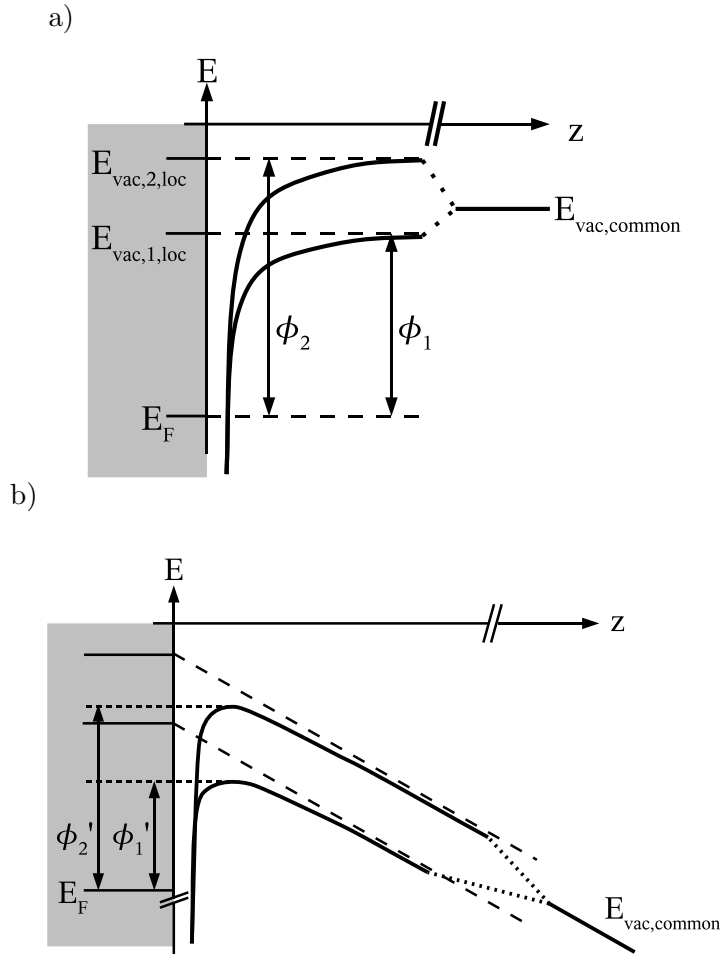


**Figure 2.23** a) The surface potential of two patches with different work functions. The half-space occupied by the metal is drawn gray. b) The surface potential of two patches with different work functions in the presence of an electric field. The surface barriers $\phi_1'$ and $\phi_2'$ are significantly different, given the strong applied field.

that leads to to a substantially lower barrier for electrons leaving the solid than for patch 2. As a consequence, the photocurrent is higher on patch 1 than on patch 2. That leads to brighter spots of the projection of the photoemission current on the phosphor screen without the need for scanning the sample. With that method an image of the sample can be recorded at once and the resolution in time is only restricted by the deexcitation time of the phosphor in the screen and the data transfer rate of the available data acquisition equipment.

The resolution of a photoemission electron microscope depends on the electric field at the sample. The higher it is the lower becomes the surface barrier for the electrons which means that the current increases and even very small patches can be resolved. The typical lateral resolution lies in the range of 10–100 nm. This is by far not sufficient to resolve structures of atomic size or transition regions between domains of different work function as it is possible with a STM. The main application of PEEM lies therefore in the real-time observation of chemical reactions at surfaces. The local work function serves here as a sensitive probe to distinguish areas of different chemical composition or crystallographic

structure on the surface.

### 2.9.4 Photoemission of adsorbed Xe (PAX)

Photoemission of adsorbed Xenon on different surfaces reveals an interesting feature: the binding energy of the $5p_{1/2}$ level with respect to $E_{vac,s}$ is within a good approximation constant for all tested surfaces [32] (the same holds for the other levels, too, but this is the one easiest to detect), where the binding energy $E_B^V$ with respect to the vacuum level equals the sum of the binding energy with respect to $E_{F,s}$ and the work function $\phi_s$:

$$E_B^V(5p_{1/2}) = E_B^F(5p_{1/2}) + \phi_s. \tag{2.32}$$

The substrate independent binding energy $E_B^V$ is due to the weak interaction of the Xenon atom [125] with any substrate. That changes the energy levels of the Xenon atom only little and allows for the vacuum level alignment of metal substrate and Xenon atom. If one sets up Eq. 2.32 for two different samples it can be concluded that

$$\Delta E_B^F(5p_{1/2}) = -\Delta\phi_s. \tag{2.33}$$

As the Xenon atoms are adsorbed at $\sim$2 Å in front of the surface, $\Delta\phi_s$ corresponds to the difference in surface potential at that point, i.e. the local work function difference. Therefore, PAX allows for the determination of differences in the local surface potential on a sample by measuring the difference on binding energies with respect to $E_{F,s}$ of the different Xe species on the sample. These species differ by their local environment.

Although the electron detector is far away from the sample surface the local information can be determined from the kinetic energy analysis because the binding energy of the electrons in the Xenon atom with respect to the local vacuum level is constant, in analogy to the 2PPE experiments of image potential states (see Fig. 2.24). The electron coming from Xenon atoms on patch 1 will gain the kinetic energy $x_1$ to the initial kinetic energy while the electron coming from patch 2 looses kinetic energy $x_2$ on its way to the electron analyzer. The difference is the contact potential times $e$ which is measured as the difference in binding energy with respect to $E_{F,s}$.

The PAX method is useful to study differences of the surface potential on a sample with a lateral resolution that is given by $\sim$1 nm [32]. It is true that PAX allows to distinguish patches on the surface with a size on the nanometer scale. But it is not known on what type of patch the Xenon is adsorbed. And, mainly, it is not possible to check the surface potential continuously along a certain trajectory on the sample surface. The relative location of the different patches detectable with PAX can not be determined which weakens the term "lateral resolution" in that context. In contrast to this, STM allows to address a certain point on the sample and any other arbitrary point the position of which with respect to the first one is known. Therefore, STM meets the requirements of a much stricter definition of the term "lateral resolution".

## 2.10 FER data in mechanical break junction experiments

In tunnelling experiments with mechanical break junctions, it is possible to measure the FERs spectrum as a dI/dV spectrum in constant current mode in the same way as with a STM. The only difference is that the location of the tunnel junction or the tunnel junctions is not exactly known. But if clean metal wires are used to form the break junction then

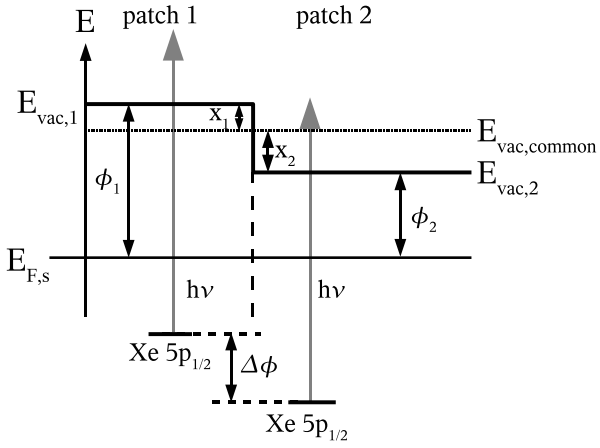


**Figure 2.24** The energy diagram on a sample with adsorbed Xe. The fixed binding energy of the Xe with respect to the vacuum level allows for the determination of local surface potential differences.

this problem is not important anymore as any junction will be made up between two electrodes of the same, well defined material at any place. Supposing a trapezoidal barrier between the two electrodes and a constant electric field in the junction during the dI/dV measurement, the peak positions $V_n$ of the FERs in the dI/dV spectrum can be described as follows for the limiting case of very high $n$ [126–128] (compare also Eq. 2.6):

$$eV_n = \phi_s + \left(\frac{3\pi\hbar e}{2\sqrt{2m}}\right)^{\frac{2}{3}} F^{\frac{2}{3}} n^{\frac{2}{3}}, \tag{2.34}$$

where $F$ is the electric field in the junction. That means that a linear interpolation of a plot of the high $n$ peak positions down to $n = 0$ should yield $\phi_s$ as the intersection with the voltage axis. Fig. 2.25a,c,e show the application of the method to dI/dV data obtained with an STM on Ag(100), 2 ML NaCl/(Ag(100), and 3 ML NaCl/Ag(100). Three dI/dV spectra are shown where the FER peak positions are plotted as a function of $n^{\frac{2}{3}}$. The dependence on $n^{\frac{2}{3}}$ is indeed linear for high $n$. For the lower $n$ peaks irregularities are seen on Fig. 2.25c and e. They appear at voltages where the $\Delta z$ data shows rounded steps for the FERs, i.e. low amplitudes in the dI/dV spectrum. These are most probably due to resonances in the dielectric layer [39,129]. The energy of a state is lowered if a half-cycle of the wave function perpendicular to the surface fits in the dielectric layer. That decreases in turn the amplitude of the wave function outside the layer which reduces the overlap with the tip states, i.e. the conductance.

The linear regression of the highest peak positions in the dI/dV spectrum leads to $\phi_s$ values of 5.05 eV on Ag(100), 4.10 eV on 2 ML NaCl/Ag(100), and 3.59 eV on 3 ML NaCl/Ag(100). The value for Ag(100) is higher than any other value found in the literature [92,130–132]. And, spurisingly, the values for 2 ML and 3 ML NaCl/Ag(100) are differing by ∼0.5 eV although the FER series start approximately at the same voltage in the dI/dV spectra for the two thicknesses which indicates similar work functions [20]. But the interpretation of the linear regression in Fig. 2.25a,c,e in terms of Eq. 2.34 is difficult as the basic assumptions for the derivation of that equation are not fullfilled in a STM experiment. The approximation of the trapezoidal barrier is not sufficient in that case. The electric field can not be taken as the one of two plane electrodes, especially not for

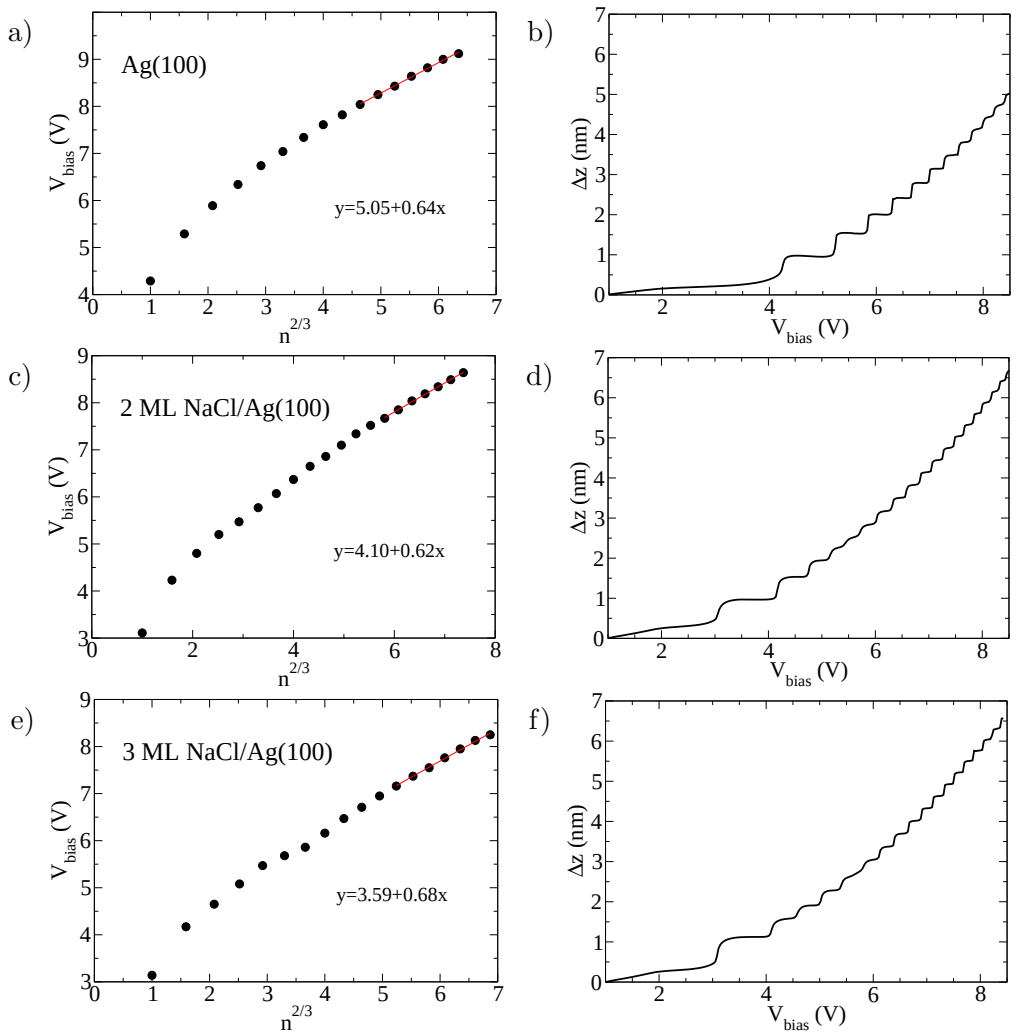


**Figure 2.25** a), c), and e) FER peak positions in dI/dV spectra plotted as a function of the quantum number $n^{2/3}$. The red line is a linear fit through the last seven points. The equations are given in the corresponding graph. A special feature is observed at $V_{bias} \approx 5.8$ V in (c,d) and (e,f). b), d), and f) The corresponding $\Delta z$ data, i.e. the distance that the tip retracted during the dI/dV measurement.

the large tip-sample distances present during the measurement of the high $n$ FERs. If the distance between tip and sample becomes comparable to the radius of curvature of the tip apex, the geometrical shape of the tip can not be neglected anymore. Additionally, the electric field is not constant during the dI/dV measurement with enabled feedback loop even if it is calculated with the plane electrode approximation. That is obvious in Fig. 2.25b,d,f where the $\Delta z$ data during the spectrum acquisition is plotted. A constant electric field calculated as $V_{bias}/(z_0 + \Delta z)$ would correspond to a straight line through the origin which is not the case. The $\Delta z$ data seems to follow a parabolic curve as a function of $V_{bias}$. In the case of the NaCl covered sample the electric field is partially screened in the dielectric layer. Therefore, the electric field cannot be constant along the tunnel junction in this case. The trapezoidal barrier approximation is invalid for a system containing dielectrics.

In the case of mechanical break junctions the situation is different than in STM,

the obtained work functions agree with the values obtained by other techniques and the $V(n^{2/3})$ plot becomes linear for high $n$. That is true even for dI/dV spectra where the FER peaks appear modulated due to interference of several tunnel channels [126] (as observed in STM experiments with blunt tips, too [133]). The trapezoidal barrier approximation is valid in that case as the electric field becomes more and more the one of planar electrodes as the electrode separation increases. For short distances between the electrodes the roughness of the electrode surface has still an influence on the distribution of the electric field in the junction. The constant field during the constant current dI/dV measurement is assumed but seems to agree with the experiments.

## 2.11 Conclusion

In conclusion, measurements of FERs with STS in combination with a calculation based on a simple 1D model of the potential well between tip and sample yield the local work function changes induced by ultra-thin dielectric NaCl islands of different height grown on a Ag(100) substrate. This method spatially maps the local work function with a typical lateral resolution of 1 nm.

The model itself can be used not only for the determination of the local work function changes but also for the attribution of states in constant current dI/dV spectra where other states in thin adsorbed layers exist beside the FERs [134–136].

# Chapter 3

# New molecular structures on Ag(100) and Ag(110)

## 3.1 Introduction

Adsorption of molecules on surfaces, especially transition metal surfaces, is an important process not only for the basic understanding of changes in the surface electronic structure but also for technological processes used to produce tons of chemicals every year. The huge interest in these adsorption processes stems from the ability of transition metal surfaces to catalyze chemical reactions. That means that the surface either decreases the activation energy of a chemical reaction or even makes a reaction possible at all, that would not occur without the catalyst. Heterogeneous catalysis, where one phase is gaseous and the other solid, has the big advantage of the easy recovery of the catalyst, which is much more difficult with homogenous catalytic techniques. In this way, a chemical reaction can be maintained almost continuously. The products desorb from the surface and leave a free adsorption site for the reactants. Famous examples are the Fischer-Tropsch process, where CO and $H_2$ react to higher alkanes and water mediated by a Co or Fe surface. These can either be used for the synthesis of well defined lubricants [137] or for new generations of synthetic fuels like gas-to-liquid (GTL) [138] where the gas for synthesis is extracted from biomass. The same reactants undergo a different reaction scheme on the Ni(111) surface with methanol and formaldehyde as the products [139]. Platinum is another important catalyst which is present in catalytic converters that free car exhaust gases from the toxic CO [140] and NO. CO is transformed in a catalytic reaction to $CO_2$ by the reaction with oxygen and NO is converted by the reaction with hydrogen to $N_2$ and water. An example where a complex alloy of several metals forms the catalyst for the reaction is the Haber-Bosch process. $N_2$ and $H_2$ react to form $NH_3$, an important step in the production of fertilizers [141].

A large part of catalytic research is done by empirical methods which shows that the interaction of small molecules, like for instance $H_2$ or CO, with transition metal surfaces often leads to surprising results. By far not all of the processes are yet understood at an atomic level.

As another example of these surprising results two new molecular structures formed on silver single crystal surfaces are found. After interaction of a gas mixture consisting of $H_2$, $H_2O$, CO, $CO_2$, and $N_2$ with the silver single crystal surfaces Ag(100) and Ag(110) especially beautiful symmetries are formed. The local structure is well resolved by STM,

while the lack of chemical sensitivity of STM does not allow for a definitive determination of the chemical species in the two new structures.

### 3.1.1 Experimental

In the preparation chamber, the Ag(100) and Ag(110) samples are cleaned by Ar sputtering and annealing cycles. Then the sample is cooled down to a temperature between 150 K and RT. A homebuilt evaporator is then heated up with the shutter closed. Due to a slight degassing of the heated parts ($p = 5 \cdot 10^{-9}$ mbar), which consist of a Macor piece surrounded by a coiled Ta wire and the Ta crucible, the partial pressure of all residual gases increased in the preparation chamber. These gases are mass spectrometrically identified as $H_2$, $H_2O$, CO, $CO_2$, and $N_2$. The cooled down sample is exposed to that gas mixture for 1–10 min and transferred into the STM [53] which is operated at 50 K with cut PtIr tips.

## 3.2 Pseudo hexagonal and double row structure

Fig. 3.1a shows an overview STM image of a Ag(100) sample prepared according to Sec. 3.1.1. The sample temperature during deposition was 150 K. As the same structures were observed after exposure to the gas mixture at all sample temperatures between 150 K and 250 K, no distinction is made in the following between samples prepared at different temperatures. Above 250 K no adsorption is observed anymore, the sample stays clean. On the overview image, the Ag(100) substrate terraces partially covered by the molecular layers can be seen. Cracks are visible in these layers, which have all approximately the same height. Fig. 3.1c shows a close-up of a terrace, exhibiting two different structures present on the sample under the same preparation conditions. They have slightly different apparent heights (see Fig. 3.1d). The higher one presents a pseudo hexagonal structure (see Fig. 3.2a) and the other one with the characteristic parallel lines has a double row structure (see Fig. 3.2b).

On samples where the terraces are not fully covered, the pseudo hexagonal structure is found in islands without any particular shape. The edges of these islands are round and curved. The structure itself consists of a slightly modified hexagonal lattice: due to an arrangement of neighboring rows by pairs, “corridors” appear that make the structure lose its translational symmetry (see Fig. 3.2c). The missing elements on Fig. 3.2a and Fig. 3.2c show that one spot on the STM image corresponds to one building block of the structure. There is no special orientation of the pseudo hexagonal structure with respect to the underlying substrate, neither on Ag(100) nor on Ag(110). The same holds for the double row structure (see Fig. 3.2b). As both structures and all their properties are the same on Ag(100) and Ag(110) surfaces, no distinction is made in the following between these two sample surfaces. If a particular surface is mentioned, it is only for the purpose of a correct image description.

The double row structure has a rectangular unit cell of a size of $1.6 \times 0.8$ nm$^2$. It consists of a structure made up by round spots of two different apparent heights in the STM images. The abundance ratio of the two type of spots is 1 : 1. The islands of the double row structure have a rectangular shape if their growth is not hindered in a certain direction by substrate step edges, which are never overgrown, or another island. Fig. 3.3c shows the edge of rectangular double row island. The edges of these islands are preferably either parallel or perpendicular to the direction of the dense double rows.

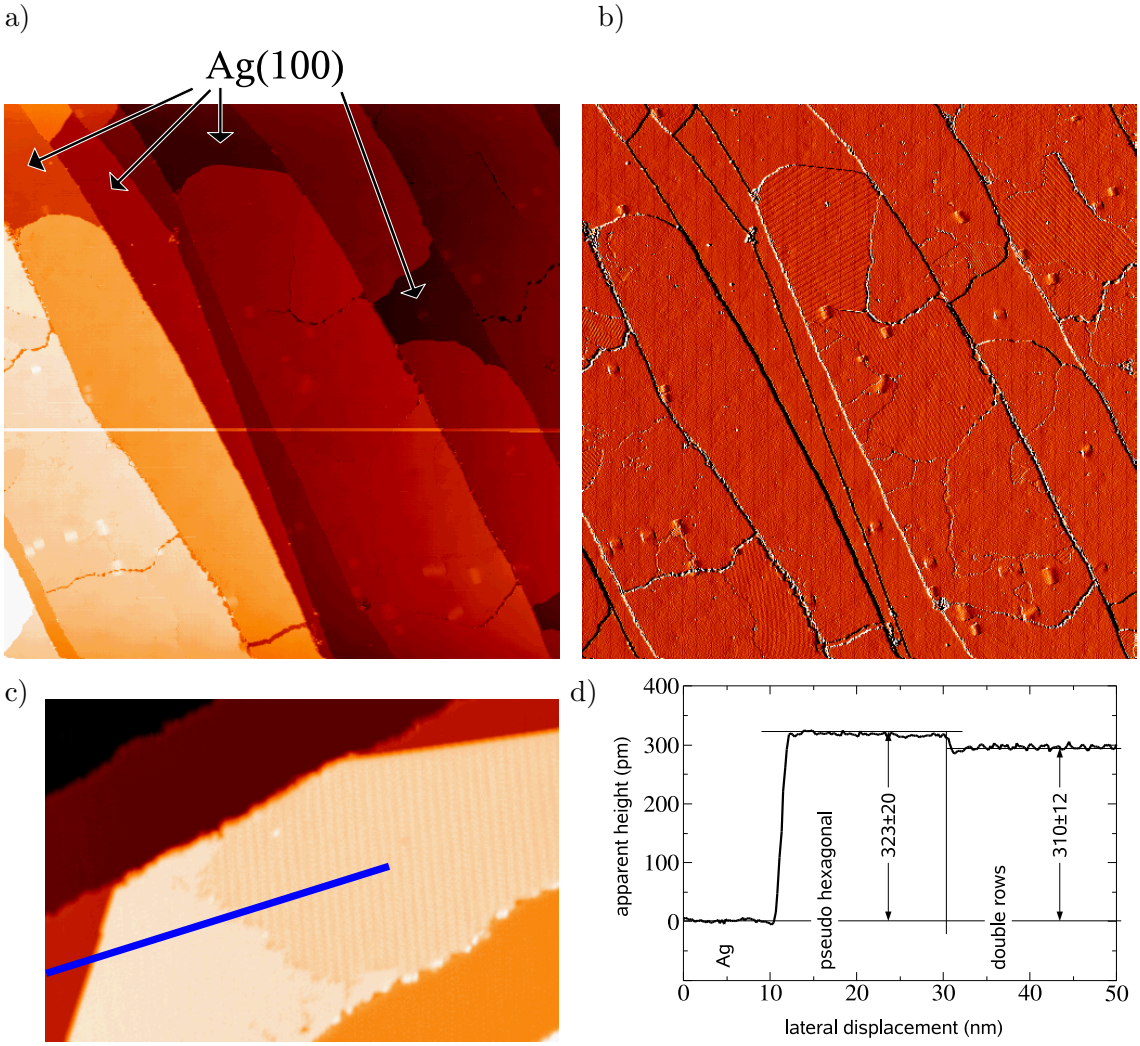


**Figure 3.1** a) Overview of a Ag(100) sample covered by the molecular layer. The bridge-like protrusions are growth defects of the underlying substrate [142]. 600×600 nm$^2$, $V_{bias}$ = 1.0 V, $I$ = 20 pA. b) Derivative in $x$ direction of a). The cracks between the growth zones are visible and the two structures are distinguishable. c) Close-up of the two structures. The double row structure is characterized by parallel lines even visible on large scale images. 45×67 nm$^2$, $V_{bias}$ = −2.0 V, $I$ = 20 pA. d) Profile along the blue line in c). The apparent height does not change in the range from −1 V to −4 V.

As the double row structure has no mirror plane perpendicular to the sheets on the substrate, one expects to have a structure exhibiting 2D chirality. Indeed, two different modifications of the double row structure are found, that behave like image and mirror image in the plane and that cannot be superimposed by translation and rotation in the plane of the substrate surface (see Fig. 3.3a,b). In Fig. 3.3a the row formed by four bright spots are inclined to the left with respect to the dense double rows while in Fig. 3.3b the row of bright spots is inclined to the right.

The pseudo hexagonal structure and the double row structure are both very sensitive to positive voltages and are easily destroyed under these conditions. Therefore, most of the images are scanned at negative voltages for which the apparent height of the structures is constant (see Fig. 3.1d). Although the structures are quite sensitive to a positive electric field, they are generally stable at 50 K. No diffusion of molecules was observed during

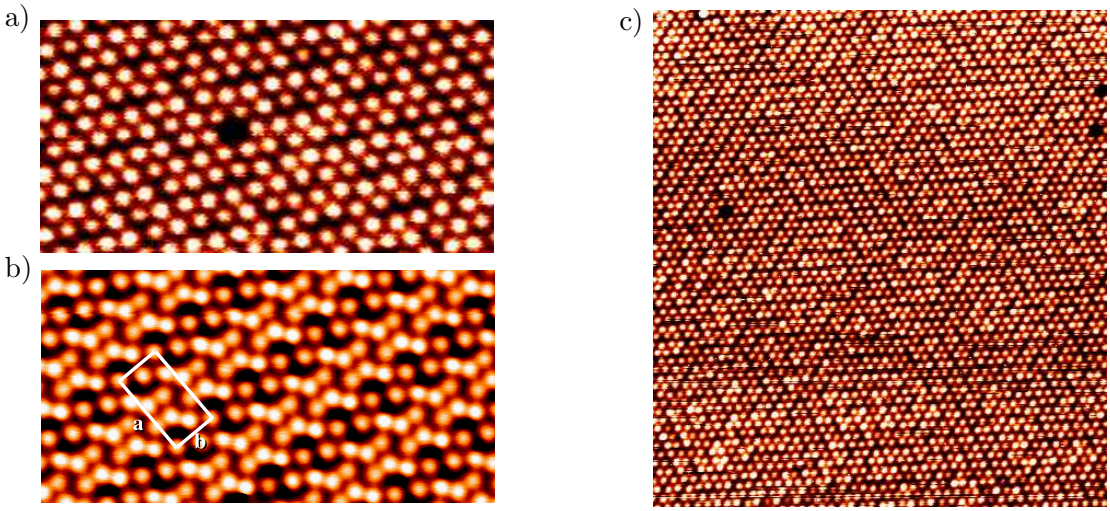


**Figure 3.2** a) The pseudo hexagonal structure. The lattice constant averaged over the whole structure is 440±20 pm. 8×4 nm$^2$, $V_{bias} = -2.0$ V, $I = 20$ pA. b) The double row structure. The unit cell dimensions are $a = 1.62 \pm 0.12$ nm, $b = 0.83 \pm 0.06$ nm. 8×4 nm$^2$, $V_{bias} = -0.5$ V, $I = 20$ pA. c) A larger view on the pseudo hexagonal structure that reveals the formation of "corridors". 19×19 nm$^2$, $V_{bias} = -2.8$ V, $I = 20$ pA.

subsequent scans of the same sample area.

The apparent height found for the two new structures is quite large and different to what has been found up to now in STM experiments on the molecules that are worth considering. Experiments with nitrogen lead mainly to nitride islands on transition metal surfaces, either formed by ion sputtering and subsequent annealing, see e.g. [143–145], or by dissociative adsorption of $N_2$ at the surface [146]. The nitride islands on transition metals appear generally as depressions. Only undissociated $N_2$ molecules appear as protrusions as measured on Cu(110) [147] which leaves them as a candidate for the new structures. CO molecules are generally imaged in STM as depressions, as single molecules [148] as well as ordered layers [149,150]. Water molecules, water clusters, and ordered water layers are imaged as protrusions in STM [151, 152] but the apparent heights for voltages close to $E_{F,s}$ lie in the range from 60 to 110 pm [152], i.e. much lower than what is found for the new structures. Molecular hydrogen is almost invisible in STM images [27] and is mainly characterized by its inelastic excitations in dI/dV spectra. Atomic hydrogen is imaged in STM on Cu(100) as a depression [153]. Concerning $CO_2$, STM experiments are performed on Ag(110). But in order to observe the chemisorbed $CO_2$ species, that appears as a protrusion in STM images, promoters as oxygen [154, 155] or cesium [156] are necessary. Both studied promoters are excluded to be present on the two Ag surfaces. Comparing with the literature, $N_2$ seems the only candidate among the possible molecules that corresponds to the characterization of the new stuctures by apparent height. But as the electronic structure of the surface influences strongly the density of states of the adsorbed species no final conclusion can be drawn from the comparison with other surfaces than silver.

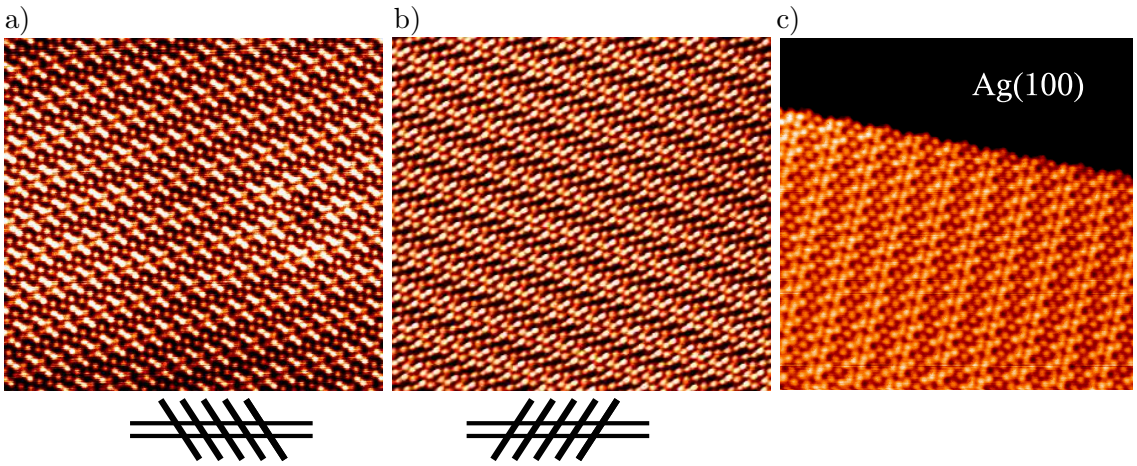


**Figure 3.3** Molecular resolution of the double row structure. a) 15×14 nm$^2$, $V_{bias} = 0.2$ V, $I = 20$ pA. b) 15×14 nm$^2$, $V_{bias} = -0.48$ V, $I = 20$ pA. a) and b) are the two chiral modifications of the double row structure. The scheme below shows the difference in orientation of the row of bright spots on the two images. c) Island edge of a double row island perpendicular to the double rows. This orientation and the one parallel to the double rows are the preferred orientations of the island borders. 14×14 nm$^2$, $V_{bias} = -0.5$ V, $I = 20$ pA.

## 3.3 Spectroscopy

### 3.3.1 dI/dV spectroscopy

Fig. 3.4 shows a dI/dV spectrum in constant current mode measured on the pseudo hexagonal structure on Ag(100) showing the first and second FER. As the structure is very sensitive to positive voltages both spectra are averages over several spectra measured with a short acquisition time, i.e. a fast scan through the voltage ramp. The shift of the first FER from ∼4.4 V on Ag(100) to ∼3.8 V on the pseudo hexagonal structure indicates a work function decrease of roughly half an electronvolt. The corresponding measurement on the double row structure yields a spectrum that is shifted by ∼50 mV to lower voltages compared to the pseudo hexagonal structure. Consequently, the work function change induced by the adorption for the two structures is approximately the same. In the following, a comparison with the literature concerning the work function change induced by the molecules under consideration is given.

The adsorption of water induces generally a work function decrease. On Ru(100) the work function decreases by up to 1.5 eV [157, 158] depending on the degree of coverage. Slightly smaller work function changes are observed for Ni(111) [159] and Cu(100) [160]. The value of the work function change varies from 0.2 eV to 1.0 eV until saturation. The same is observed even on the oxide compound $TiO_2$ [161, 162]. The work function change in the examples mentioned before is bigger than the one observed in the dI/dV measurements on the two new structures. That work function decrease has to be compared to the one at complete monolayer coverage when measured with a non-local method, which are in the mentioned cases the Kelvin Probe method and photoemission. But a different orientation of the water molecule can easily cause differences in the surface dipole layer and consequently in the work function. Water is therefore still a candidate for the new structures.

The adsorption of CO on metal surfaces generally introduces a work function increase.

That is observed for instance for $Ni_3Al(111)$ [163], an Al-Pd surface alloy [164], Co(0001) [165], and Mn covered Cu(100) [166]. The observed work function increase lies in the range from 0.2 eV on Co(0001) to 0.9 eV on the Mn covered Cu surface. These results agree with the view of the CO molecule adsorbing with the carbon atom bound to the metal surface because that creates a dipole that increases the work function, if one supposes that the oxygen atom is negatively polarized and the carbon atom positively. In the gas phase the dipole is oriented in the opposite direction [167]. This is due to the spatial extent of the HOMO, which is mainly a free electron pair at the carbon atom and reaches far away from the CO bond. This compensates for the polar bond between the carbon and the oxygen which is, as expected, positive on the carbon and negative on the oxygen. On a surface, the influence of the HOMO is reduced as it is involved in the bonding [168].

In special cases a work function decrease is observed after CO adsorption. During the adsorption on a Pt-Cu surface alloy a maximum decrease of 0.2 eV is found which is attributed to bridge-site adsorption. CO adsorption on Cu(332) causes a work function decrease, too, which is probably again related to the adsorption site but no final conclusion is drawn in [169]. On the stepped surface Cu(332) the work function decrease is strongly dependent on the adsorption temperature and the coverage and reaches a maximum value of 0.4 eV. As the new structures are incommensurate with the substrate, arguments on the adsorption site cannot play a role for Ag(100) and Ag(110). From the work function considerations, it is unlikely that CO forms the new structures.

Carbon dioxide is found to decrease the work function of Cu(110) upon adsorption by about 0.4 eV [170] and is therefore still a candidate.

The work function change of molecular hydrogen adsorbed on metal surfaces shows no general trend due to the multitude of surface layer phases of hydrogen (see, e.g. [148], and references therein). On W(110) hydrogen induces a work function decrease of about 0.5 eV at monolayer coverage [171]. But on Fe covered W(110), the work function increases with increasing hydrogen coverage [171]. On Pd(210) a decrease of 0.4 eV of the work function is observed after only 0.3 L of hydrogen [172]. Independent of the work function change, which is still still speaking in favor of $H_2$, hydrogen is too small for the observed structures. It is hence unlikely for hydrogen to be the single constituent of the new structures.

Molecular nitrogen causes a decrease of the work function on Ni(110) by up to 0.1 eV [173] and can therefore principally be considered for the new structures.

dI/dV spectroscopy performed with open feedback loop reveales no features of inelastic tunneling around the Fermi level in the voltage range from $-270$ mV to $+270$ mV. The measurements are performed with currents up to 1 nA on the pseudo hexagonal islands and up to 300 pA on the double row islands. These values correspond to the highest currents possible without destruction of the molecular layers. But that result does not exclude the presence of molecules that exhibit vibrational modes in that energy range. For instance, the CO hindered translation on Cu(100) and Cu(110) and the Cu-CO stretch vibration are not observed in dI/dV spectra on single molecules [174]. Additionally, the molecules in the layers do not necessarily exhibit the vibrational properties of the isolated molecule but the collective vibrational excitations of the layer.

As a summary, the dI/dV experiments leave $H_2O$, $CO_2$, and $N_2$ as possible candidates for the new structures as long as the adsorption of a single species is considered. The adsorption of $H_2$ and CO is unlikely to be the reason for the new structures given the dI/dV results.

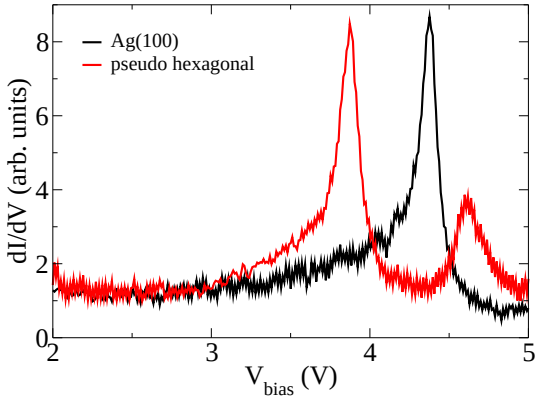


**Figure 3.4** dI/dV spectrum with the feedback looped enabled on the pseudo hexagonal structure. $I = 20$ pA, $V_{mod,pp} = 10$ mV.

### 3.3.2 Electron spectroscopy

In order to obtain more insight into the chemical nature of the adsorbed species, electron spectroscopy experiments are carried out. For that purpose, two types of samples are prepared. First, a Ag(100) single crystal is exposed, while held at 50 K, to the gas mixture produced by the heated evaporator for 30 min. The long exposure time is needed in order to get a significant signal from the measurement, but leads to multiple layers of the adsorbed species which is not necessarily the same as the one (or two) species observed in the monolayer regime. The second sample is Ag(100) surface exposed to CO for 100 s at $10^{-8}$ mbar and a sample temperature of 50 K. The EELS experiments are done with a primary electron energy of 30 eV. The UPS measurements are carried out with a He discharge lamp and a corresponding photon energy of 40.8 eV. All the measurements are done at a sample temperature of 50 K.

Fig. 3.5a shows the EELS spectrum measured on the Ag(100) sample exposed to the evaporator. Exactly the same peaks are observed on the Ag(100) sample exposed to CO as seen in Fig. 3.5c. Fig. 3.5b shows the UPS spectrum measured on the sample exposed to the evaporator. Four distinct peaks are visible. The same peaks are observed in Fig. 3.5d, the UPS spectrum measured on the Ag(100) sample exposed to CO. Only the relative intensities of the peaks are different. Apparently, the only species that adsorbs significantly on Ag(100) is CO. But as the sample temperature during deposition is lower than 150 K and the experiments are done with thick layers, the results cannot be transferred directly to the case of the monolayer adsorbed at 150 K.

## 3.4 Adsorption of single molecular species on Ag(100)

### 3.4.1 Water

The adsorption of water on Ag(100) is used to test wether one or perhaps both of the observed structure are formed by water molecules. To do so, water is dosed on a Ag(100) sample at 150 K at $1 \cdot 10^{-7}$ mbar for 100 s. The STM images of the sample show layers the structure of which cannot be determined due to a lack of resolution. Probably, the layer which shows a small irregular corrugation is amorphous. As the fine structure of the pseudo hexagonal and the double row structure can easily be resolved even on large

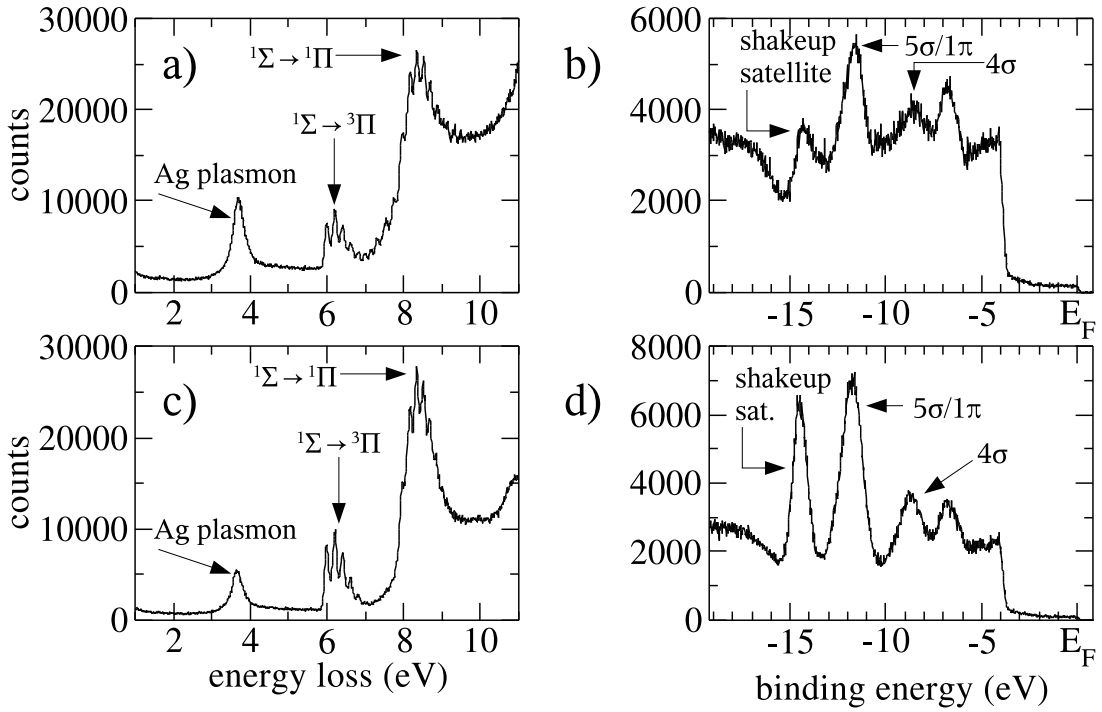


**Figure 3.5** a) EELS spectrum of Ag(100) exposed to the gas mixture of the evaporator. The assignment of the peaks is given according to [113]. The resolution of the vibrational fine structure indicates the formation of multilayers. b) UPS spectrum of Ag(100) exposed to the evaporator. Peak positions: −14.3 eV, −11.7 eV, −8.5 eV, −6.8 eV. Assignments of the peaks according to [175], but there is a discussion in the literature about the assignment of CO peaks in UPS and other attributions are proposed [113,176,177]. c) EELS spectrum of Ag(100) exposed to CO. d) UPS spectrum of Ag(100) exposed to CO. Peak positions: −14.5 eV, −11.7 eV, −8.7 eV, −6.7 eV.

scale images, water is excluded from the possible molecules, that form the new structures. These are not formed—at least not exclusively—by water molecules.

### 3.4.2 Carbon monoxide

To see if the new structures are made of carbon monoxide, adsorption experiments with CO are carried out. CO is dosed in the preparation chamber at a pressure of $1 \cdot 10^{-8}$ mbar. Under these conditions no adsorption of CO on a Ag(100) sample at 150 K is observed. The sample stays clean as checked by STM. That means that CO cannot be the only molecule forming the new structures. To verify the hypothesis that another molecule catalyzes the adsorption of CO on Ag(100) before the formation of the new structures, CO is dosed on the sample at 50 K to force the adsorption and to check the behavior of the CO molecules at higher temperatures by annealing. Fig. 3.6a shows an overview image of CO/Ag(100) where the adsorption temperature was 50 K. One sees a few single CO molecules that are imaged as depressions [148,149,178]. The other objects are either small clusters or big, disordered CO agglomerations. Fig. 3.6b shows a close-up of a sample area exhibiting three different types of objects: four circular depressions that are identified as CO molecules, a dimer as deduced from its similarity to dimers manually assembled on

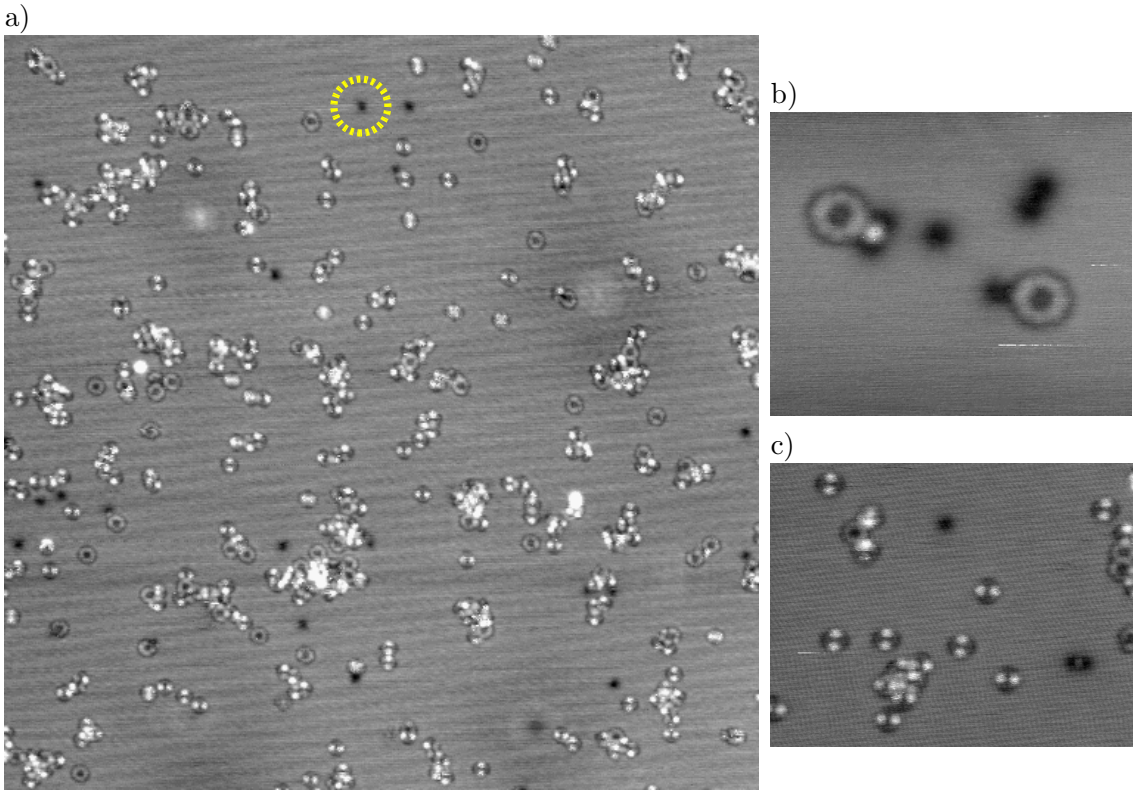


**Figure 3.6** a) Overview image of a Ag(100) sample exposed to CO at 50 K. Disordered structures are formed. The yellow dashed circle indicates one of the few single CO molecules, imaged as a depression (color code: black=low, white=high). The other objects are clusters of several CO molecules. 50×50 nm$^2$, $V_{bias} = 0.2$ V, $I = 20$ pA. b) Close-up STM image showing four CO molecules, one dimer, and two clusters imaged as rings. 7×5 nm$^2$, $V_{bias} = 0.1$ V, $I = 20$ pA. c) Close-up STM image showing a single CO molecule, a dimer, the ring-like clusters, and several clusters that appear as two protrusions in a circular depression. They exist in two different orientations, following the symmetry of the substrate lattice. 15×12 nm$^2$, $V_{bias} = 0.1$ V, $I = 5$ pA.

Cu(111) [148] that manifest itself by a bright spot with two black lobes, and two objects that are imaged as rings. It is not known how many CO molecules form the latter type of cluster. Fig. 3.6c shows another close-up STM image of the sample containing—among others—a single CO molecule, a dimer, some ring-like clusters, and several clusters that are imaged as two protrusions in a circular depression. Two orientations of these clusters are observed, differing by an angle of 90°. That indicates a twofold symmetry of the cluster that is oriented along two equivalent lattice directions on the underlying square lattice of Ag(100). The number of CO molecules forming these clusters is not known.

All the observed clusters as well as the single molecules are stable at 50 K. No differences between subsequent scans of the same image are observed. To check wether the CO molecules arrange differently when provided a higher thermal energy, annealing experiments are carried out. The sample is, after CO dosage at 50 K, warmed up to temperatures up to 280 K. After having reached the desired temperature, the sample is immediately transferred back into the STM. Fig. 3.7 shows a sample after annealing to 280 K. The trend found by that sample and other annealing experiments to lower temperatures is the following: The higher the sample temperature during the annealing, the more the disordered CO agglomerations dissolve until at the highest annealing temperature before

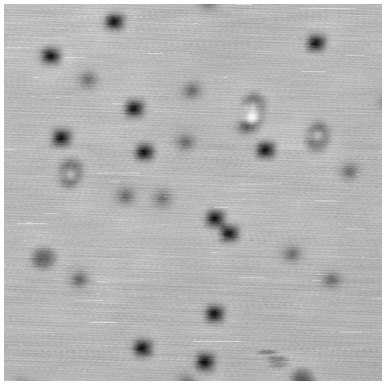

**Figure 3.7** The CO covered Ag(100) after annealing to 280 K. The clusters are not present anymore. Two types of single molecules exist, differing in the deepness of the depression on the STM image. 20×20 $nm^2$, $V_{bias} = 1.0$ V, $I = 20$ pA.

complete desorption of CO (280 K) almost only single CO molecules are observed on the sample. Two different types of depressions are observed on Fig. 3.7, ∼70 pm and ∼50 pm deep, respectively. Different adsorption sites could explain this as the sample was rapidly cooled down after the annealing, freezing the diffusing CO molecules probably in a non-equilibrium distribution of lattice sites. After adsorption at 50 K, only the 50 pm deep depressions are found as observed for adsorption at 15 K on Cu(111) [148]. But the main observation after the annealing experiments is that the CO molecules, while diffusing at higher temperatures on the sample, are not binding to each other and do not form packed structures, especially not the two new ones. Consequently, it is clear that CO is not the constituent—at least not exclusively—of the new structures.

## 3.5 Conclusion

The data available for the new structures do not allow for a final conclusion on their chemical composition. If one supposes that the structures are made up by molecules of only one species then $H_2O$ and CO can be ruled out. The adsorption experiments with $H_2O$ lead only to disordered structures at an adsorption temperature of 150 K. The CO adsorption experiments show that CO does not even adsorb at all at a sample temperature of 150 K on Ag(100). The next step would be to check if $N_2$ or $CO_2$ adsorb on Ag(100) or Ag(110) at 150 K sample temperature. Adsorption experiments are the easiest and fastest way to check which molecule of the gas mixture can form the new structures. But if these do not lead to the desired result, i.e. the formation of the new structures on a silver surface, then co-adsorption experiments have to be carried out. In that case the new structures would be formed by a catalytic reaction at the silver surface or by an intercalation compound. In both cases STM can only confirm the structures but not identify the chemical species on the surface. The chemical identification has to be done by a method that provides information about the detailed electronic structure of the surface layer. EELS and photoemission are two techniques that are in principle well suited for that task. The experimental difficulty is related to the thickness of the monolayer which does not provide enough molecules in order to get a good signal-to-noise ratio. The measurement time for a monolayer has to be increased in order to obtain a good signal-

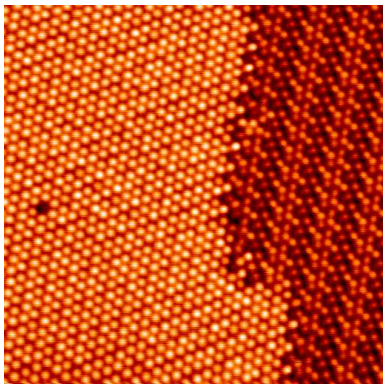

**Figure 3.8** A pseudo hexagonal and a double row domain right next to each other. The growth is continuous between both regions. 14×14 nm$^2$, $V_{bias} = -0.6$ V, $I = 20$ pA.

to-noise ratio. During this extended measurement time the layer must not be destroyed by the radiation. If the formation of the new structures is the result of a catalytic process at the silver surface, the exposure time for the gas mixture can not be simply increased as it is not sure that the chemical composition of the second and higher layers is the same as for the first one, which is the only one that is in contact with the metal surface.

The same holds for the sticking coefficient. Even if there is no reaction at the silver surface, the sticking coefficient of the small molecules can be different on silver compared to silver covered by a molecular layer, which in turn can result in different molecules adsorbing on the clean silver surface and on the molecule-covered silver surface. The interpretation of the electron spectroscopy data is then possibly complicated by the presence of signals from different molecules at the surface, if only the contribution of the first layer to the total signal is not completely buried under the rest. The same problem of overlapping signals can appear for intercalated compounds or in the case that the two structures are not made up of the same molecule. Fig. 3.8 shows the transition zone between two domains, one with the pseudo hexagonal structure, and the other with the double row structure. The structures are connected smoothly. The dense double rows lie in one of the three pseudo hexagonal main symmetry directions. That way of connection of the two structures is always found when there is a direct transition between both without a crack (see Fig. 3.1b). This behavior favors the interpretation of one molecule being present on the silver surface in two different modifications.

Finally, the new structures on Ag(100) and Ag(110) open up the possibility to study in detail molecular layers that are only weakly interacting with the substrate and form a structure that is completely independent of the substrate symmetry. STM is the ideal tool to discover the structural properties of these layers, as every domain is rotated arbitrarily with respect to the substrate, which makes these structures invisible in non-local experiments for structure determination like LEED.

# Chapter 4

# STM study of a $BC_3$ covered $NbB_2(0001)$ surface

## 4.1 Introduction

Recently, because of its peculiar atomic structure and its characteristic physical properties, compounds with a graphitic honeycomb structure consisting of boron, carbon, and nitrogen have attracted the attention of material scientists. In particular, boroncarbon honeycomb structures such as BC and $BC_3$ [179] are investigated theoretically in the expectation of high superconducting transition temperatures ($T_c$) of isomorphic compounds of $MgB_2$ ($T_c$ = 39 K) [180, 181]. Indeed, high $T_c$'s of 100 K and 70 K were predicted for LiBC [182] and $Mg_2BC_3$ [183], respectively. However, no experimental data have been reported because those specimens were not available so far.

In previous papers [184,185], the growth of a $BC_3$ sheet on $NbB_2(0001)$ is described. All data obtained by angle-resolved X-ray photoelectron spectroscopy, angle-resolved ultraviolet photoelectron spectroscopy, LEED, and high resolution electron energy loss spectroscopy indicated that the uniform $BC_3$ honeycomb sheet of monolayer thickness grows epitaxially and is incommensurate with respect to the substrate lattice [185]. The sheet presents an excellent crystalline quality on a macroscopic level [186].

In this chapter, the $BC_3$ covered $NbB_2(0001)$ crystal surface is investigated using STM and LEED to clarify the microscopic structure of the $BC_3$ sheet, and STS to obtain information on its possible superconducting properties. In particular, the high $T_c$ of $BC_3$ is predicted under the hole-doping conditions [187]. In the present case, the charge transfer occurs probably from the $BC_3$ to $NbB_2$ substrate similarly to intercalated graphite compounds.

### 4.1.1 Experimental procedure

The experiments are performed in two STM setups located in Tokyo and in Lausanne. In Tokyo, the system is composed of a main vacuum chamber with a base pressure of less than $1{\cdot}10^{-8}$ Pa housing a conventional RT STM (Omicron) and a preparation chamber equipped with micro-channel plate LEED optics and a CMA analyzer for AES. At Lausanne, the low-temperature experiments down to 5 K are conducted in a custom-built UHV STM [53]. The STM experiments are performed in constant-current mode. The probe tip is a cut PtIr wire of 0.3 mm diameter.

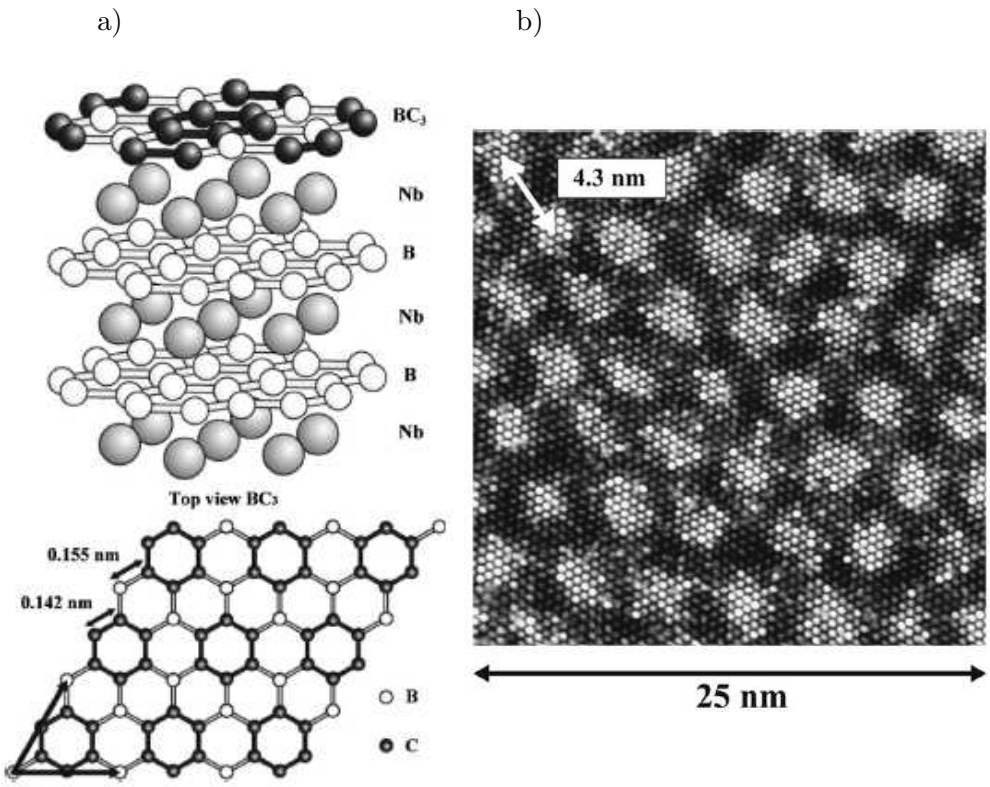


**Figure 4.1** a) Ball and stick model of the honeycomb structure of $BC_3$ on a $NbB_2(0001)$ single crystal surface. b) Typical STM image of a $BC_3$ covered $NbB_2(0001)$ surface taken at RT showing a moiré pattern with indicated periodicity. The bright areas exhibit a shorter periodicity (∼540 pm) than the dark areas (∼590 pm). 25×25 nm$^2$, $V_{bias} = 150$ mV, $I = 0.20$ nA.

The specimen used in this experiment is a $NbB_2(0001)$ disc cut from a crystal rod. One face of the specimen is polished mechanically by diamond powders and fixed in a Ta holder before mounting in the vacuum chamber. Finally, the specimen is heated in UHV by electron bombardment to clean the surface, and to fabricate the $BC_3$ sheet, as confirmed by AES and LEED. The $NbB_2(0001)$ crystal contains carbon impurities (180 ppm). These carbon atoms segregate to the surface at an elevated temperature, resulting in the formation of various boroncarbon sheets on the surface. In particular, annealing at 1300 K for several hours leads to the growth of an epitaxial $BC_3$ sheet on the $NbB_2(0001)$ surface lattice as shown in Fig. 4.1a and Fig. 4.1b.

## 4.2 Results and discussion

Fig. 4.1b shows a typical STM image of a $BC_3$ covered $NbB_2(0001)$. The sheet entirely covers the surface. The two different interatomic distances of the $BC_3$ sheet and of the substrate generate a moiré pattern, with a large periodicity of $4.3 \pm 0.3$ nm. The STM image shown in Fig. 4.2 has been taken at a temperature of 5 K and at a bias voltage of 20 mV. With a low tunnel voltage (approximately below 100 mV) another structure appears in the STM images in the low-contrast region of the moiré pattern. Different periodic distances are clearly recognized for the protrusions in the high contrast and in the low

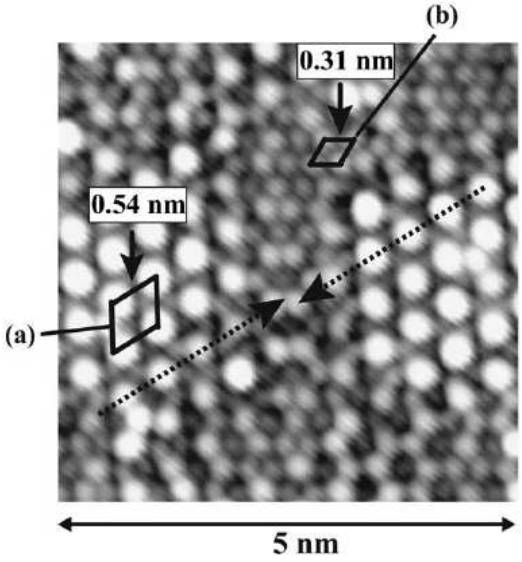


**Figure 4.2** Small area STM image of a $BC_3$ covered $NbB_2(0001)$ surface measured at 5 K. The periodic rows of bright protrusions inside a high contrast region shift with respect to the ones in a neighboring region (dotted arrows). The two rhombuses indicate two different periodicities. $V_{bias} = 20$ mV, $I = 10$ nA.

contrast surface regions. The periodic distance of the bright protrusions, indicated by the large rhombus (a) in the high contrast region, is 0.54 nm and then unchanged compared to the images at higher voltage like Fig. 4.1b. This corresponds to $\sqrt{3}a$, where $a = 0.31$ nm is the surface lattice constant of the substrate. On the other hand, as indicated by the small rhombus (b), the periodic distance of the protrusions in the low contrast region is simply the lattice constant of the substrate, $a = 0.31$ nm. As shown by two dotted arrows in Fig. 4.2, a periodic row of the bright protrusions inside a high-contrast region is slightly shifted compared to the neighboring high-contrast regions indicating that neighboring bright areas of the moiré pattern are shifted by one lattice constant $a$. It should be noted that no periodicity corresponding to the geometry of the $BC_3$ sheet was found directly in the STM images, independently of bias and temperature conditions.

Fig. 4.3 shows a LEED pattern and a 2D Fourier transform (FT) pattern of the STM image displayed in Fig. 4.2. The features of the FT pattern are consistent with those of the LEED pattern. In the LEED pattern, many satellite spots originating from electron diffraction by the $BC_3$ lattice and by the substrate lattice [184] appear. Sets of mainly three intense spots are arranged in a hexagonal manner. The wave vectors of those spots correspond to a wavelength of 0.52 and 0.59 nm, respectively, in real space; the value of 0.52 nm is exactly the in-plane lattice constant of the $BC_3$ sheet. The value of 0.59 nm is obtained by subtraction of the reciprocal lattice vector of the $BC_3$ sheet from those of the substrate. In the LEED pattern, the (20) spots of the $BC_3$ sheet are most intense, while the triple satellite spots are lower in intensity. An identical structure is observed in the FT pattern of the STM image (Fig. 4.2) shown in Fig. 4.3b, where the satellite spots are most prominent as the substrate lattice is not imaged with a perfect regularity. Only faint spots due to a 1×1 structure of the substrate are observed. Interestingly, in both the LEED and FT patterns, at the expected diffraction spot positions originating from a $\sqrt{3} \times \sqrt{3}$ structure, indicated by the crosses at the center of the triple satellite spots in the lower part of Fig. 4.3a and Fig. 4.3b, diffraction spots are absent. That confirms again

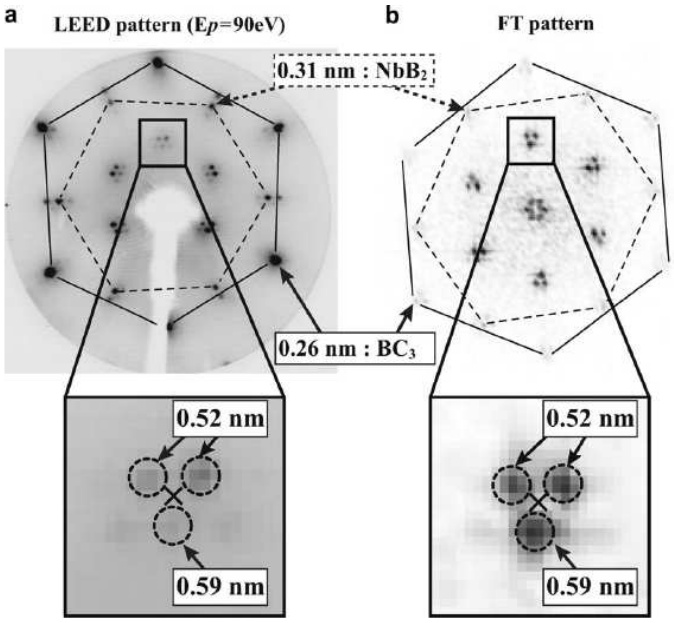


**Figure 4.3** a) LEED pattern of the $BC_3$ covered $NbB_2(0001)$ surface, b) Fourier transform pattern of the STM image shown in Fig. 4.2. The triple spots displayed in the lower part of the figure correspond to wave vectors with wavelengths of 0.52 nm and 0.59 nm, respectively.

the incommensurability of the $BC_3$ layer with the substrate.

Fig. 4.4 presents the reverse FT image calculated exclusively from the triple spots observed in the FT image shown in Fig. 4.3b. The distance of 0.54 nm between the bright protrusions as well as the shift in the periodic rows is clearly reproduced, as indicated by arrows. Hence, not only the large periodicity of 4.3 nm but also the short periodic arrangement of 0.54 nm between the protrusions in the STM images originate from the moiré pattern.

Similar kinds of moiré patterns were reported for the monolayer graphite covered Pt(111) surfaces [188, 189], but the periodicity of the overlayer of graphite was also detected directly in the STM images without Fourier transform, unlike the $BC_3$ covered $NbB_2(0001)$. Since no information such as electron transfer and orbital hybridization between the $BC_3$ sheet and a metallic substrate exists, the origin of the transparent property of the $BC_3$ sheet on $NbB_2(0001)$ is still unclear. However, it is presumably understandable by the low density of states of a $BC_3$ sheet around the Fermi level: a $BC_3$ sheet is predicted to be a semiconductor with an energy gap of 0.7 eV [190], and the low density of state leads to small contribution to the tunneling current around the Fermi level.

In an attempt to determine a superconducting energy gap and to verify the predicted high $T_c$ in the BC honeycomb compounds, we conducted STS measurements at a temperature of 5 K on the clean $BC_3$ covered $NbB_2$ surface. However, differential conductance (dI/dV) spectra measured on various locations of the surface under open feedback loop conditions with tunnel currents ranging from 0.04 to 0.4 nA, modulation voltages from 1 to 4 mV, and bias voltages from 20 to 100 mV around the Fermi energy showed no indication of an energy gap.

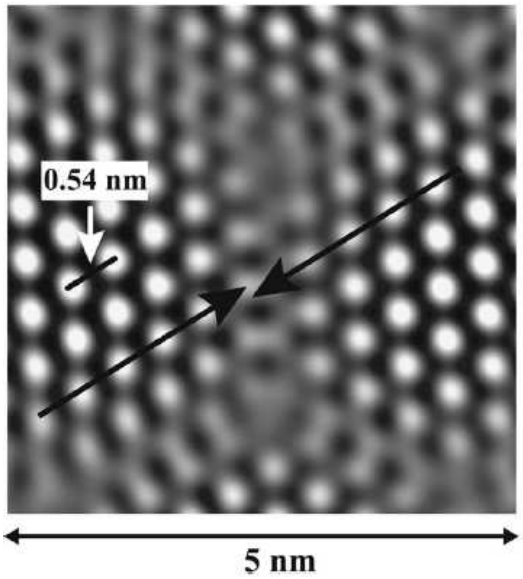


**Figure 4.4** Reverse Fourier transform image calculated exclusively from the triple spots in the FT image of Fig. 4.3b. The distance of 0.54 nm between the bright protrusions as well as the shift of the periodic rows is clearly reproduced.

## 4.3 Hydrogen on $BC_3/NbB_2(0001)$

### 4.3.1 Background

Hydrogen attracts a lot of interest due to its special properties which stem from its small mass and its simple electronic structure [191]. These special properties, for instance the ability to diffuse easily inside a metal, make it also the most common residual gas in ultra high vacuum systems [192]. It is incorporated as atomic hydrogen in the metallic parts composing the vacuum system. The hydrogen atoms can diffuse in the metal and reach the surface. Here, they recombine and molecular hydrogen is desorbed which is measured by the pressure gauges. In a simple model [193] it is assumed that there is only one energy state of the diffusing hydrogen atoms and that the rate-limiting step is the diffusion of the hydrogen atoms to the surface. While there is a good agreement with vacuum experiments at relatively high hydrogen pressures the model fails at low outgas rates, i.e. at low hydrogen coverage of the surface. It turns out that the experimental results cannot be reproduced for small numbers of hydrogen atoms on the surface. Another model assumes therefore that the diffusion of hydrogen atoms at the surface occurs with a finite speed, which was also observed for hydrogen atoms on Cu(100) with an STM [153]. Compared to the diffusion speed of the hydrogen atoms, the following recombination step and the thermally activated desorption [194] are fast.

In the experiment described here a $BC_3/NbB_2$ sample was cooled down to 5 K. Then, the cryostat of the STM was heated up to 20 K for about 2 min before cooling down to the normal working temperature of 5 K again. This procedure caused an increased degassing of the hydrogen on the surfaces of the cryostat. This is not only due to increased diffusion of hydrogen atoms to the surface but mainly to desorption of molecular hydrogen from the walls, which act as cryopumps at low temperatures. When the temperature of the cryostat was again at 5 K, it is assumed that part of the hydrogen is adsorbed on the

sample, too. STS measurement were performed at 5 K. The spectroscopic signatures correspond clearly to what was already found by Gupta et al. [27], who studied hydrogen on different metal surfaces. In the following, the spectroscopic results on the $BC_3/NbB_2$ sample are presented. They are well described by the inelastic tunneling spectroscopy (IETS) theory if saturation of the occupancy of the excited state is taken into account.

### 4.3.2 Inelastic tunneling spectroscopy

A thorough introduction to IETS is given in [26]. In the present case, the fact is stressed that the occupation of the excited state of the system can be up to 100%, i.e. until saturation is reached. Calculating the tunnel current as a function of voltage, taking into account different conductances for the excited state ($\sigma_1$) and for the ground state ($\sigma_0$) as well as additional contributions to the conductance due to inelastic scattering of the tunneling electrons which are either exciting the system in the ground state ($\sigma_{up}$) or relaxing it from the excited state ($\sigma_{down}$), one obtains

$$\frac{dI}{dV} = A + \frac{B}{\left[1 + (V - V_{mode})/V^*\right]^2} \quad \text{for } |V| \geq V_{mode} \tag{4.1}$$

$$\frac{dI}{dV} = \sigma_0 \quad \text{for } |V| < V_{mode}. \tag{4.2}$$

$A$, $B$, $V^*$, and $V_{mode}$ are voltage-independent parameters. $V_{mode}$ is the energy at which the transition occurs that leads to the excited state of the system. $A$, $B$, and $V^*$ include $\sigma_0$, $\sigma_1$, $\sigma_{up}$, $\sigma_{down}$, $V_{mode}$, and $S$, the rate of spontanous relaxation of the system. The particularity of the IETS spectra with saturation is the appearance of conductance peaks in the case that $\sigma_0 < \sigma_1$ and of negative conductance if $\sigma_0 > \sigma_1$. In the case of saturation the tunnel current passes only through the channel corresponding to the excited state if $V_{bias} > V_{mode}$ so that the current-voltage curve is described by a straight line through the origin with the slope $\sigma_1$. At $V_{mode}$ this line has to join the I-V curve of the ground state, which causes the new features in the STS spectra due to a jump in the I-V curve. Fig. 4.5 shows a dI/dV spectrum measured on the $BC_3/NbB_2$ sample. Additionally, a simulated spectrum using a formula taking into account the thermal broadening and the instrumental resolution is shown. That curve is calculated by a convolution of Eq. 4.1 with a gaussian distribution function:

$$\frac{dI}{dV} = N \int_{-\infty}^{+\infty} \exp\left\{-\frac{x^2}{2p^2}\right\} \left(A + \frac{B}{\left(1 + (-x + V - V_{mode})/V^*\right)^2}\right) dx \quad \text{for} \quad x - V < -V_{mode} \tag{4.3}$$

$$\frac{dI}{dV} = \sigma_0 \quad \text{for} \quad -V_{mode} \leq x - V \leq V_{mode} \tag{4.4}$$

$$\frac{dI}{dV} = N \int_{-\infty}^{+\infty} \exp\left\{-\frac{x^2}{2p^2}\right\} \left(A + \frac{B}{\left(1 + (x - V - V_{mode})/V^*\right)^2}\right) dx \quad \text{for} \quad x - V > V_{mode} \tag{4.5}$$

The parameter $p$ describes the broadening of the dI/dV spectrum. To avoid laborious numerical calculations the integrations are done from -50 mV to +50 mV instead of $\pm\infty$. The numerical error is negligible. $N$ is the normalization factor:

$$N = \left(\int_{-\infty}^{+\infty} \exp\left\{-\frac{x^2}{2p^2}\right\} dx\right)^{-1}. \tag{4.6}$$

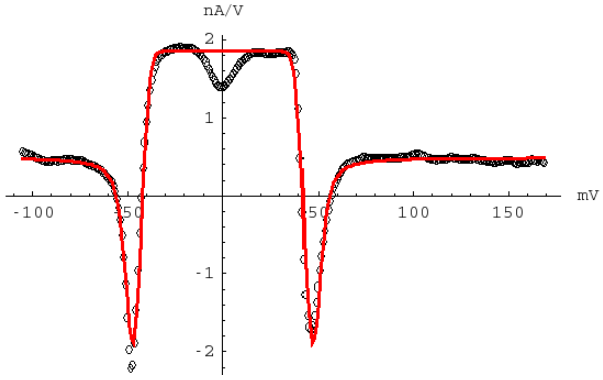


**Figure 4.5** The black circles show the dI/dV spectrum measured at a set point current of 70 pA (R=1.43 GΩ). The modulation voltage is 3 $mV_{pp}$. The red curve is calculated using Eq. 4.3 with the parameters $A = 0.49$ nA/V, $B = -21.23$ nA/V, $V^* = 1.6$ mV, $V_{mode} = 44.7$ mV, $p = 3.7$ mV.

The fit using Eq. 4.3 shows a good agreement between theory and experiment. The dip around $E_F$ is caused by another transition in the hydrogen which is not simulated by Eq. 4.1 and Eq. 4.3 , respectively. The negative conductance peaks indicate the energy of the transition which is $46 \pm 1$ mV. Gupta et al. [27] found that the spectroscopic features of hydrogen on different copper surfaces show a strong coverage dependence so that these features cannot be attributed easily to a specific transition known from other experiments. This example shows that measurements at low temperatures are not always straightforward to interpret. In the present case the obtained spectra have to be judged in the special context of the experimental preparation procedure of the sample. The measured spectra do not stem from the sample itself, i.e. the $BC_3/NbB_2$, but from adsorbates which contaminated the sample during the experiments. It is highly probable that this contaminant is hydrogen given the good agreement with [27] and the outgassing of the walls of the cryostat before the measurement. Additionally, all spectra obtained on a clean sample do not show any feature at all. Hydrogen contamination directly after the preparation of the sample can be excluded because the sample is the warmest part of the cryostat-STM system during the cool down.

## 4.4 Conclusion

A $BC_3$ covered $NbB_2(0001)$ surface has been investigated with STM, STS and LEED. A very good agreement has been found between the observed diffraction pattern in the LEED measurements and similar features in a pattern obtained by Fourier transform of STM images. This combined structural analysis proves that in the STM images both, the large periodicity of 4.3 nm between the high contrast areas and the short periodicity of 0.54 nm between the bright protrusions originate from a moiré pattern. Thus the epitaxial and incommensurate relationship between the $BC_3$ sheet covering the $NbB_2(0001)$ substrate has been clearly established. No evidence for a superconducting gap was found in the observed STS spectra measured at 5 K.

# Appendix A

# The electric potential of charged metal sphere in front of a dielectric covered metal surface

The calculation of the electric potential between tip and sample with the dielectric layer is done by the method of images and the multipole expansion method [98, 195, 196]. The basic problem is shown in Fig. A.1. It consists of a sphere representing the tip, a dielectric layer of thickness $t$ and the metal substrate. The boundary conditions that have to be respected are: (i) the surface of the sphere is an equipotential surface at a potential $V_{bias}$. (ii) The metal-dielectric interface is an equipotential surface at $V = 0$ as the sample is grounded. (iii) The electric potential in the vacuum $V_E$ and the electric potential in the dielectric $V_S$ have to satisfy the following boundary conditions at the dielectric-vacuum interface:

$$\epsilon_S \frac{\partial V_S}{\partial z} = \epsilon_E \frac{\partial V_E}{\partial z}, \tag{A.1}$$

where $\epsilon_S$ is the dielectric constant of the dielectric layer and $\epsilon_E = 1$ as there is vacuum between the tip and the sample, and

$$V_S = V_E \tag{A.2}$$

at the interface $S_A$.

The first step consists of placing a charge in the center of the sphere to set the potential at the surface to $V_{bias}$. Then the image charges have to be set to account for the boundary condition Eq. A.1. To stay general, multipoles will be used in the following where the zeroth order multipole represents a point charge. The potential of a point multipole $B_n$ of order $n$ located at $\mathbf{p}$ is given by

$$V_{B_n} = \frac{B_n}{r_p^{n+1}} P_n(\cos\theta_p), \tag{A.3}$$

where $r_p$ and $\theta_p$ are spherical coordinates centered around the point $\mathbf{p}$. The factor $\frac{1}{4\pi\epsilon_0}$ is included in $B_n$ to make the formulas simpler. The multipole of order 0 (point charge) has then the units Vm, a multipole of order 1 (dipole) the units $\mathrm{Vm}^2$, and so on. The initial point charge $B_0$ at the sphere center is calculated by

$$B_0 = V_{bias} \cdot R. \tag{A.4}$$

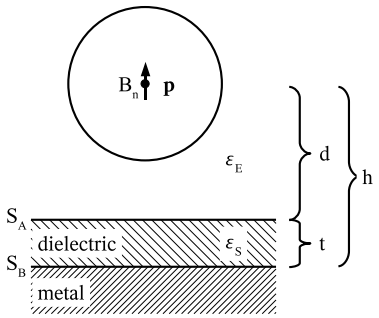


**Figure A.1** A multipole $B_n$ centered in a metal sphere in front of a metal surface covered by a dielectric solid with the dielectric constant $\epsilon_S$. $d$ is the distance between the multipole and the dielectric-vacuum interface $S_A$. The circle around $B_n$ represents the surface of the sphere.

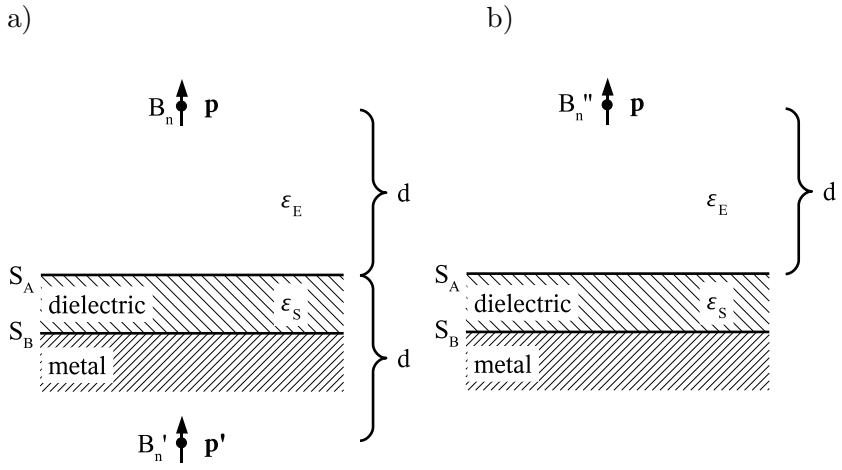


**Figure A.2** The multipoles needed to satisfy Eq. A.1 at $S_A$. a) The multipoles acting on the vacuum side and b) the multipole acting on the dielectric layer.

$P_n$ is the Legendre function. The first members of the series are:

$$P_0(x) = 1 \tag{A.5}$$
$$P_1(x) = x \tag{A.6}$$
$$P_2(x) = \frac{1}{2}(3x^2 - 1) \tag{A.7}$$
$$P_3(x) = \frac{1}{2}(5x^3 - 3x) \tag{A.8}$$
$$P_4(x) = \frac{1}{8}(35x^4 - 30x^2 + 3) \tag{A.9}$$
$$P_5(x) = \frac{1}{8}(63x^5 - 70x^3 + 15x) \tag{A.10}$$
$$P_6(x) = \frac{1}{16}(231x^6 - 315x^4 + 105x^2 - 5) \tag{A.11}$$

The higher order functions can be calculated by the following sum formula [197]:

$$P_n(x) = \frac{1}{2^n} \sum_{k=0}^{n} \binom{n}{k}^2 (x-1)^{n-k}(x+1)^k. \tag{A.12}$$

The following recursion formula is used to speed up the calculation of the binomial coefficients [198]:

$$\binom{n}{k+1} = \binom{n}{k} \frac{n-k}{k+1}. \tag{A.13}$$

An iterative procedure is needed to satisfy the boundary conditions at $S_A$ and $S_B$. In the following, $d^{(i)}$ and $h^{(i)}$ denote the distance from $S_A$ and $S_B$, respectively, at the $i^{th}$ iteration.

Two image multipoles have to be set to satisfy Eq. A.1 for the multipole $B_n$ at $\mathbf{p}$ (see Fig. A.2). $B_n$ and $B'_n$ act on the vacuum side (exterior) of the junction and $B''_n$ acts on the dielectric layer (interior). Their magnitude is given by

$$B'_n = (-1)^{n+1} K B_n \tag{A.14}$$
$$B''_n = (1-K) B_n, \tag{A.15}$$

where

$$K = \frac{\epsilon_S - \epsilon_E}{\epsilon_S + \epsilon_E}. \tag{A.16}$$

The potential in the vacuum is now $V_E = V_{B_n} + V_{B'_n}$ and in the dielectric layer $V_S = V_{B''_n}$. $V_{B'_n}$ and $V_{B''_n}$ are defined similarly to Eq. A.3, i.e. the sperical coordinate system of the potential is centered at $\mathbf{p}'$ for $V_{B'_n}$ and at $\mathbf{p}$ for $V_{B''_n}$. After having satisfied Eq. A.1 the potential at the metal-dielectric interface has to be adjusted as it is perturbed by $B''_n$. $B''_n$ acts on the dielectric layer, so a multipole $C_n^{(1)}$ has to be added as shown in Fig. A.3a. It is placed at $h^{(1)} = h$ inside the plane metal electrode as the image of $B''_n$ with respect to the surface $S_B$. $C_n^{(1)}$ is given by

$$C_n^{(1)} = (-1)^{n+1} B''_n. \tag{A.17}$$

The potential in the dielectric layer is now $V_S = V_{B''_n} + V_{C_n^{(1)}}$. The boundary condition on $S_B$ is satisfied but the potential at $S_A$ is perturbed by $C_n^{(1)}$. Two image charges have to be placed to satisfy Eq. A.1 again: $C_n'^{(1)}$ and $C_n''^{(1)}$ (see Fig. A.3b). $C_n'^{(1)}$ is placed at $d^{(1)} = d + 2t$ in the vacuum and $C_n''^{(1)}$ at $d^{(1)}$ in the sample electrode. Their magnitudes are

$$C_n'^{(1)} = (-1)^{n+1} K C_n^{(1)} \tag{A.18}$$
$$C_n''^{(1)} = (1-K) C_n^{(1)}. \tag{A.19}$$

$K$ is in this case $(\epsilon_E - \epsilon_S)/(\epsilon_E + \epsilon_S)$ because $C_n^{(1)}$ acts on the dielectric layer and not on the vacuum as $B_n$ did in Eq. A.14 and Eq. A.15. The potential in the vacuum is now $V_E = V_{B_n} + V_{B'_n} + V_{C_N''^{(1)}}$ and the potential in the dielectric layer is $V_S = V_{B''_n} + V_{C_n^{(1)}} + V_{C_n'^{(1)}}$. Because $C_n'^{(1)}$ is acting on the dielectric layer, the potential at $S_B$ is perturbed and has to be corrected by an image charge

$$C_n^{(2)} = (-1)^{n+1} C_n'^{(1)} \tag{A.20}$$

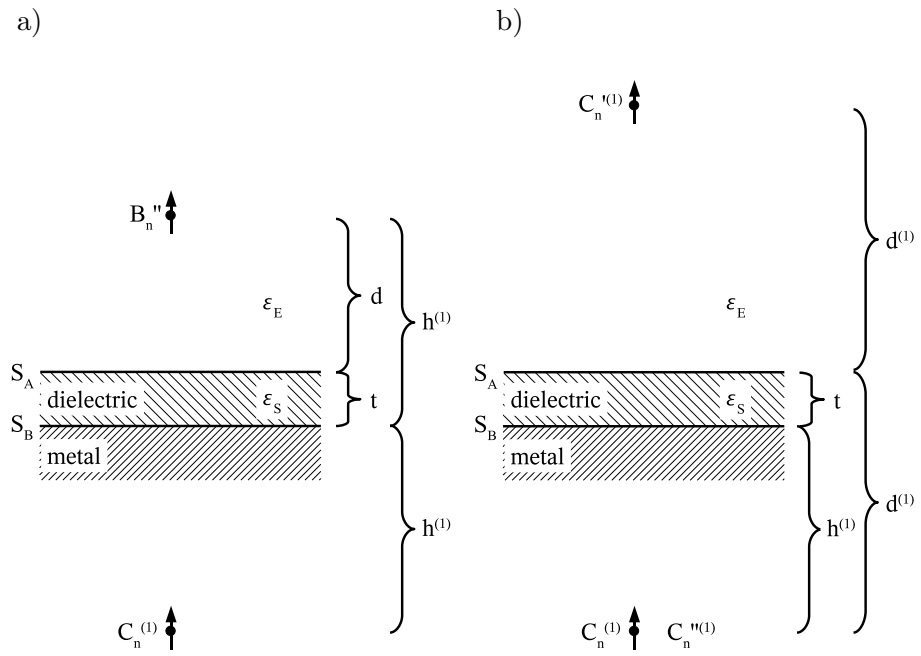


**Figure A.3** a) $C_n^{(1)}$ correcting the potential at $S_B$. b) The multipoles $C_n'^{(1)}$ and $C_n''^{(1)}$ correcting the potential at $S_A$.

placed at $h^{(2)} = h^{(1)} + t$ in the metal substrate. The potential in the dielectric is now $V_S = V_{B_n''} + V_{C_n^{(1)}} + V_{C_n'^{(1)}} + V_{C_n^{(2)}}$. But $C_n^{(2)}$ perturbs again the potential at $S_A$ which has to be adjusted by two new image charges. In this manner, the process has to be carried out until the potentials $V_E$ and $V_S$ converge. In practice, i.e. for $R$ ranging from 3 to 20 nm, $t$ from 0.2 to 2 nm, and $h - R$ from 1 to 5 nm, 15 cycles are sufficient to achieve a precision of 1 meV.

Finally, the potential in the vacuum is determined by the multipoles $C_n''^{(i)}$ and $B_n'$. They perturb the potential at the surface of the sphere which has to be corrected in the next step. The multipole $B_n$ of order 0, the initial point charge, does not perturb the potential on the sphere surface. Due to its electric field, the sphere surface is an equipotential surface at $V_{bias}$. The principle of the next step consists of a reexpansion of the $C_n''^{(i)}$ and $B_n'$ as a multipole series around the center of the sphere $\mathbf{p}$. Then an image multipole is placed for each of the elements of the expansion that sets the potential at the sphere surface back to its initial value of $V_{bias}$.

The reexpansion of a multipole is depicted in Fig. A.4. A multipole of order $n$ located at the center of a spherical coordinate system can be reexpanded at the points $m$ or $m'$ which are separated by $d$ from $B_n$ in the $\theta = \pi$ and $\theta = 0$ direction, respectively. The potential $V_p$ of a multipole of unit magnitude ($B_n = 1$) at the point $\mathbf{p}(r_p, \theta_p)$ is then after reexpansion around $m$ or $m'$:

$$V_{B_n} = \frac{1}{r^{n+1}} P_n(\cos\theta) \tag{A.21}$$

$$= \left(\frac{1}{d}\right)^{n+1} \sum_{j=0}^{\infty} \frac{(n+j)!}{n!j!} \left(\frac{-r_{m'}}{d}\right)^j P_j(\cos\theta_{m'}) \tag{A.22}$$

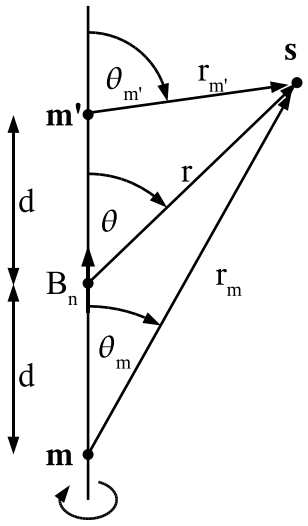


**Figure A.4** General form of the reexpansion of a multipole $B_n$ at $m$ and $m'$.

$$= \sum_{j=0}^{\infty} M_{m'j} r_{m'}^{j} P_j(\cos\theta_{m'}) \tag{A.23}$$

$$= (-1)^n \left(\frac{1}{d}\right)^{n+1} \sum_{j=0}^{\infty} \frac{(n+j)!}{n!j!} \left(\frac{r_m}{d}\right)^j P_j(\cos\theta_m) \tag{A.24}$$

$$= \sum_{j=0}^{\infty} M_{mj} r_m^j P_j(\cos\theta_m) \tag{A.25}$$

with

$$M_{m'j} = \left(\frac{1}{d}\right)^{n+1} \frac{(n+j)!}{n!j!} \left(\frac{-1}{d}\right)^j \tag{A.26}$$

$$M_{mj} = (-1)^n \left(\frac{1}{d}\right)^{n+1} \frac{(n+j)!}{n!j!} \left(\frac{1}{d}\right)^j \tag{A.27}$$

Coming back top the original problem: the sphere, that represents the tip, is placed either at $m$ or at $m'$ depending on the relative location with respect to the sphere center of the multipoles $C_n''^{(i)}$ and $B_n'$ acting on the vacuum part. After all multipoles have been reexpanded at the sphere center a term has to be added to the potential that sets the potential at the sphere surface back to its initial value $V_{bias}$ from which it deviates at this stage of the calculation due to the effect of the multipoles $C_n''^{(i)}$ and $B_n'$.

The potential at a point $\mathbf{s}(r_m, \theta_m)$ of a multipole $B_n$ of order $n$ at a distance $d$ of the sphere center $m$ of a grounded sphere, which is the center of the spherical coordinate system, is

$$V(r_m, \theta_m) = \sum_{j=0}^{\infty} M_{mj} r_m^j P_j(\cos\theta_m) + \sum_{j=0}^{\infty} \frac{B_{mj}}{r_m^{j+1}} P_j(\cos\theta_m). \tag{A.28}$$

The first term is the reexpansion of the multipole $B_n$ at the sphere center $m$. The second term takes into account the polarization of the metal sphere by the original multipole

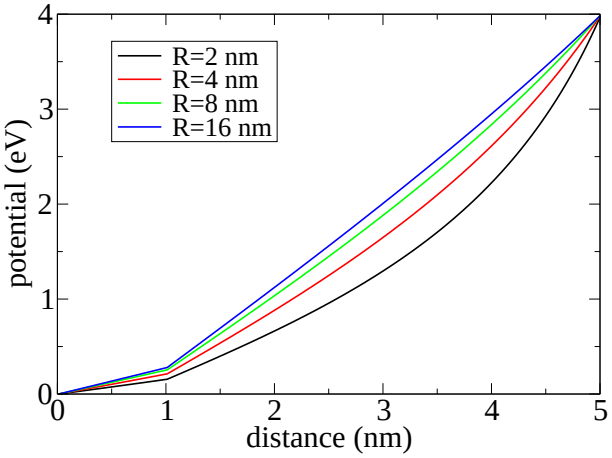


**Figure A.5** The electric potential along the $z$ direction that goes through the center of the sphere. The metal surface is at distance 0, and the sphere surface is at distance 5 nm. The thickness $t$ of the dielectric layer ($\epsilon = 3$) is 1 nm. The potential energy of an electron at the tip's surface is 4 eV.

$B_n$. It consists of a series of multipoles $B_{mj}$ centered at $m$ and of order $j$. They are given by

$$B_{mj} = -M_{mj} R^{2j+1}, \tag{A.29}$$

where $R$ is the radius of the sphere. After that step a series of multipoles $B_{mj}$ is located at the sphere center that perturb the potential at $S_A$. That means that the potential at that interface has to be adjusted again by the procedure described above in this chapter for every multipole $B_{mj}$, creating in turn again a set of multipoles—because the potential at $S_B$ has to be adjusted during the same iterative procedure as well—that pertubs the potential at the sphere surface. An iterative approach allows to solve the problem. In practice, the potential converges with a precision of 1 meV after 10 cycles with multipoles up to order 10. Examples with different sphere radii are shown in Fig. A.5.

# Acknowledgements

First of all I want to acknowledge Wolf-Dieter Schneider for giving me the opportunity to work on a fascinating research subject in his group and for letting me the freedom necessary to develop new ideas.

I want to acknowledge as well Roman Fasel, Ulrich Höfer, and Jascha Repp, who accepted to be member of the jury and to judge this thesis, for investing their time in this task.

During my thesis I appreciated the discussions with François Patthey on all the subjects of my thesis which was a valuable help throughout the four years.

A great help was the proof reading of this manuscript by Christophe Brun and Pierre Brodard.

Thanks a lot to Markus Ternes, Elizabeta Ćavar, and Marie-Christine Blüm, with whom I spent a fantastic time at the Uni as well as in our spare time. Unfortunately, they had to leave Lausanne too early.

I want to thank the other group members Frédéric Rossel, I-Po Hong, Pierre Brodard, Marina Pivetta, and Christophe Brun for the nice accompany and especially the refreshing table tennis breaks. And I learned a lot during the discussions on physics with Christophe Brun, who joined me in my empty office half a year after Markus Ternes left.

I want to acknowledge Akira Ueno, who came to Lausanne for a STM measurement session. I enjoyed his company in the lab a lot. He did by far most of the work that lead to chapter 4 of this thesis.

# Curriculum vitae

Hans-Christoph Ploigt
born 1976-11-15 in Karlsruhe, Germany
nationality: german

| | |
|---|---|
| 11/03-10/07 | PhD thesis at the Ecole Polytechnique Fédérale de Lausanne (EPFL) in surface physics |
| 10/97 - 5/03 | Chemistry studies in Marburg, Germany<br>degree obtained: "Diplom-Chemiker" |
| 9/00 - 8/01 | Theoretical chemistry studies in Bordeaux, France |
| 8/96-7/97 | Civil service at the "Diakonisches Werk" in Rastatt, Germany |
| 6/96 | High school degree, "Abitur", Ludwig-Wilhelm-Gymansium, Rastatt, Germany |

Publications during this thesis:

- A. Ueno, T. Fujita, M. Matsue, H. Yanagisawa, C. Oshima, F. Patthey, H.-C. Ploigt, W.-D. Schneider, S. Otani, *Scanning tunneling microscopy study on a $BC_3$ covered $NbB_2$(0001) surface*, Surf. Sci. **600** (2006) 3518
- H.-C. Ploigt, C. Brun, M. Pivetta, F. Patthey, W.-D. Schneider, *Local Work Function Changes Determined by Field Emission Resonances: NaCl/Ag(100)*, Phys. Rev. B **76** (2007) 195404

# Bibliography


[1] R. D. Young, J. Ward, and F. Scire, The topografiner: An instrument for measuring surface microtopography, *Rev. Sci. Instr.* **43** (1972), 999.

[2] G. Binnig and H. Rohrer, Scanning tunneling microscopy, *Helv. Phys. Acta* **55** (1982), 726.

[3] G. Binnig, H. Rohrer, C. Gerber, and E. Weibel, Surface studies by scanning tunneling microscopy, *Phys. Rev. Lett.* **49** (1982), 57.

[4] G. Binnig and H. Rohrer, Scanning tunneling microscopy, *Surf. Sci.* **126** (1983), 236.

[5] R. Young, J. Ward, and F. Scire, Observation of metal-vacuum-metal tunneling, field emission, and the transition region, *Phys. Rev. Lett.* **27** (1971), 922.

[6] J. M. Pitarke, F. Flores, and P. M. Echenique, Tunneling spectroscopy: surface geometry and interface potential effects, *Surf. Sci.* **234** (1990), 1.

[7] J. D. Zuber, K. L. Jensen, and T. E. Sullivan, An analytical solution for microtip field emission current and effective emission area, *J. Appl. Phys.* **91** (2002), 9379.

[8] J. Li, W.-D. Schneider, R. Berndt, W. O. Bryant, and S. Crampin, Surface-state lifetime measured by scanning tunneling spectroscopy, *Phys. Rev. Lett.* **81** (1998), 4464.

[9] G. Rubio-Bollinger, H. Suderow, and S. Vieira, Tunneling spectroscopy in small grains of superconducting $MgB_2$, *Phys. Rev. Lett.* **86** (2001), 5582.

[10] A. J. Heinrich, J. A. Gupta, C. P. Lutz, and D. M. Eigler, Single-atom spin-flip spectroscopy, *Science* **306** (2004), 466.

[11] R. Wiesendanger, I. V. Shvets, D. Bürgler, G. Tarrach, H. J. Güntherodt, and J. M. D. Coey, Magnetic imaging at the atomic level, *Z. Phys. B - Cond. Mat.* **86** (1992), 1.

[12] T. E. Madey, K.-J. Song, C.-Z. Dong, and R. A. Demmin, The stability of ultrathin metal films on W(110) and W(111), *Surf. Sci.* **247** (1991), 175.

[13] J. Bardeen, Tunnelling from a many-particle point of view, *Phys. Rev. Lett.* **6** (1961), 57.

[14] J. Tersoff and D. R. Hamann, Theory of the scanning tunneling microscope, *Phys. Rev. B* **31** (1985), 805.

[15] A. Selloni, P. Carnevali, E. Tosatti, and C. D. Chen, Voltage-dependent scanning-tunneling microscopy of a crystal surface: Graphite, *Phys. Rev. B* **31** (1985), 2603.

[16] N. D. Lang, Spectroscopy of single atoms in the scanning tunneling microscope, *Phys. Rev. B* **34** (1986), 5947.

[17] E. L. Wolf, *Principles of electron tunneling spectroscopy*, Oxford university press (1989).

[18] R. H. Good and E. W. Müller, Field emission, in S. Flügge, editor, *Handbuch der Physik*, volume 21, 176, Springer Verlag (1956).

[19] W. A. Harrison, Tunneling from an independent-particle point of view, *Phys. Rev.* **123** (1961), 85.

[20] K. H. Gundlach, Zur Berechnung des Tunnelstroms durch eine trapezförmige Potentialstufe, *Solid-State Elec.* **9** (1966), 949.

[21] R. S. Becker, J. A. Golovchenko, D. R. Hamann, and B. S. Swartzentruber, Real-space observation of surface states on Si(111) 7x7 with the tunneling microscope, *Phys. Rev. Lett.* **55** (1985), 2032.

[22] J. A. Stroscio, R. M. Feenstra, and A. P. Fein, Electronic structure of the Si(111) 2x1 surface by scanning-tunneling microscopy, *Phys. Rev. Lett.* **57** (1986), 2579.

[23] J. Moreland and J. W. Ekin, Electron tunneling experiments using NbSn 'break' junctions, *J. Appl. Phys.* **59** (1985), 3888.

[24] L. Esaki, New phenomenon in narrow germanium p-n junctions, *Phys. Rev.* **109** (1958), 603.

[25] I. Giaever, Energy gap in superconductors measured by electron tunneling, *Phys. Rev. Lett.* **5** (1960), 147.

[26] M. Ternes, *Scanning tunneling spectroscopy at the single atom scale*, Ph.D. thesis, Ecole Polytechnique Fédérale de Lausanne (2006).

[27] J. A. Gupta, C. P. Lutz, A. J. Heinrich, and D. M. Eigler, Strongly coverage-dependent excitations of adsorbed molecular hydrogen, *Phys. Rev. B* **71** (2005), 115416.

[28] K. Nagaoka, T. Jamneala, M. Grobis, and M. F. Crommie, Temperature dependence of a single Kondo impurity, *Phys. Rev. Lett.* **88** (2002), 077205.

[29] M.-C. Blüm, M. Pivetta, F. Patthey, and W.-D. Schneider, Probing and locally modifying the intrinsic electronic structure and the conformation of supported nonplanar molecules, *Phys. Rev. B* **73** (2006), 195409.

[30] G. Binnig, K. H. Frank, H. Fuchs, N. Garcia, B. Reihl, H. Rohrer, F. Salvan, and A. R. Williams, Tunneling spectroscopy and inverse photoemission: image and field states, *Phys. Rev. Lett.* **55** (1985), 991.

[31] J. Stark, Beobachtungen über den Effekt des elektrischen Feldes auf Spektrallinien. I. Quereffekt, *Ann. d. Phys.* **348** (1914), 965.

[32] K. Wandelt, The local work function of thin metal films: Definition and measurement, in P. Wissmann, editor, *Thin metal films and gas chemisorption*, chapter 7, 280, Elsevier (1987).

[33] D. P. Woodruff and T. A. Delchar, *Modern techniques of Surface Science*, Cambridge university press, $2^{nd}$ edition (1994).

[34] K. Wandelt, The local work function: Concept and implications, *Appl. Surf. Sci.* **111** (1997), 1.

[35] P. M. Echenique and J. B. Pendry, The existence and detection of Rydberg states at surfaces, *J. Phys. C: Solid State Phys.* **11** (1978), 2065.

[36] K. Giesen, F. Hage, F. J. Himpsel, H. J. Riess, and W. Steinmann, Two-photon photoemission via image-potential states, *Phys. Rev. Lett.* **55** (1985), 300.

[37] V. Dose, W. Altmann, A. Goldmann, U. Kolac, and J. Rogozik, Image-potential states observed by inverse photoemission, *Phys. Rev. Lett.* **52** (1984), 1919.

[38] D. Straub and F. J. Himpsel, Identification of image-potential surface states on metals, *Phys. Rev. Lett.* **52** (1984), 1922.

[39] W. Berthold, F. Rebentrost, P. Feulner, and U. Höfer, Influence of Ar, Kr, and Xe layers on the energies and lifetimes of image-potential states on Cu(100), *Appl. Phys. A* **78** (2004), 131.

[40] D. F. Padowitz, W. R. Merry, R. E. Jordan, and C. B. Harris, Two-photon photoemission as a probe of electron interactions with atomically thin dielectric films on metal surfaces, *Phys. Rev. Lett.* **69** (1992), 3583.

[41] M. Donath and K. Ertl, Adsorbate-induced enhancement of image-potential surface states on Ni(110), *Surf. Sci.* **262** (1992), L49.

[42] R. Fischer, S. Schuppler, N. Fischer, T. Fauster, and W. Steinmann, Image states and local work function for Ag/Pd(111), *Phys. Rev. Lett.* **70** (1993), 654.

[43] J. M. R. Weaver and D. W. Abraham, High resolution atomic force microscopy potentiometry, *J. Vac. Sci. Technol. B* **9** (1991), 1559.

[44] H. Bethge and M. Klaua, Photo-electron emission microscopy of work function changes, *Ultramicroscopy* **11** (1983), 207.

[45] L. Olesen, E. Lægsgaard, I. Stensgaard, and F. Besenbacher, Comparative study of methods for measuring the apparent barrier height on an atomic scale, *Appl. Phys. A* **66** (1998), S157.

[46] R. S. Becker, J. A. Golovchenko, and B. S. Swartzentruber, Electron interferometry at crystal surfaces, *Phys. Rev. Lett.* **55** (1985), 987.

[47] T. Jung, Y. W. Mo, and F. J. Himpsel, Identification of metals in scanning tunneling microscopy via image states, *Phys. Rev. Lett.* **74** (1995), 1641.

[48] D. B. Dougherty, P. Maksymovych, J. Lee, and J. T. Yates Jr., Local spectroscopy of image-potential-derived states: From single molecules to monolayers of benzene on Cu(111), *Phys. Rev. Lett.* **97** (2006), 236806.

[49] A. Hanuschkin, D. Wortmann, and S. Blügel, Image potential and field states at Ag(100) and Fe(110) surfaces, *Phys. Rev. B* **76** (2007), 165417.

[50] A. Kubetzka, M. Bode, and R. Wiesendanger, Spin-polarized scanning tunneling microscopy in field emission mode, *Appl. Phys. Lett.* **91** (2007), 012508.

[51] S. M. Gray, Photoemission with the STM, *J. Electron. Spectrosc. Relat. Phenom.* **109** (2000), 183.

[52] Y. Nakayama, H. Kondoh, and T. Ohta, Nanometer-scale mapping of local work function with a photon-assisted STM technique, *Appl. Surf. Sci.* **241** (2005), 18.

[53] R. Gaisch, J. K. Gimzewski, B. Reihl, R. R. Schlittler, M. Tschudy, and W.-D. Schneider, Low-temperature ultra-high-vacuum scanning tunneling microscope, *Ultramicroscopy* **42** (1992), 1621.

[54] L.-G. Liu and W. A. Bassett, Compression of Ag and phase transformation of NaCl, *J. Appl. Phys.* **44** (1973), 1475.

[55] M. Pivetta, F. Patthey, M. Stengel, A. Baldereschi, and W.-D. Schneider, Work function moiré on ultrathin ionic films: NaCl on Ag(100), *Phys. Rev. B* **72** (2005), 115404.

[56] W. Hebenstreit, M. Schmid, J. Redinger, R. Podloucky, and P. Varga, Bulk terminated NaCl(111) on aluminium: A polar surface of an ionic crystal ?, *Phys. Rev. Lett.* **85** (2000), 5376.

[57] W. Hebenstreit, J. Redinger, Z. Horozova, M. Schmid, R. Podloucky, and P. Varga, Atomic resolution by STM on ultra-thin films of alkali halides: experiment and local density calculations, *Surf. Sci.* **424** (1999), L321.

[58] K. Glöckler, M. Sokolowski, A. Soukopp, and E. Umbach, Initial growth of insulating overlayers of NaCl on Ge(100) observed by scanning tunneling microscopy with atomic resolution, *Phys. Rev. B* **54** (1996), 7705.

[59] J. Repp, S. Fölsch, G. Meyer, and K.-H. Rieder, Ionic films on vicinal metal surfaces: Enhanced binding due to charge modulation, *Phys. Rev. Lett.* **86** (2001), 252.

[60] J. Repp, G. Meyer, and K.-H. Rieder, Snell's law for surface electrons: Refraction of an electron gas imaged in real space, *Phys. Rev. Lett.* **92** (2004), 036803.

[61] E. Ćavar, M.-C. Blüm, M. Pivetta, F. Patthey, M. Chergui, and W.-D. Schneider, Fluorescence and phosphorescence from individual $C_{60}$ molecules excited by local electron tunneling, *Phys. Rev. Lett.* **95** (2005), 196102.

[62] L. Ramoino, M. von Arx, S. Schintke, A. Baratoff, H.-J. Güntherodt, and T. Jung, Layer-selective epitaxial self-assembly of porphyrins on ultrathin insulators, *Chem. Phys. Lett.* **417** (2006), 22.

[63] J. Repp, G. Meyer, F. Olsson, and M. Persson, Controlling the charge state of individual gold adatoms, *Science* **305** (2004), 493.

[64] J. Kramer, C. Tegenkamp, and H. Pfnür, The growth of NaCl on flat and stepped silver surfaces, *J. Phys.: Condens. Matter* **15** (2003), 6473.

[65] R. Bennewitz, S. Schär, E. Gnecco, O. Pfeiffer, M. Bammerlin, and E. Meyer, Atomic structure of alkali halide surfaces, *Appl. Phys. A* **78** (2004), 837.

[66] M. Kiguchi, S. Entani, K. Saiki, H. Inoue, and A. Koma, Two types of epitaxial orientations for the growth of alkali halide on fcc metal substrates, *Phys. Rev. B* **66** (2002), 155424.

[67] R. Bennewitz, V. Barwich, M. Bammerlin, C. Loppacher, M. Guggisberg, A. Baratoff, E. Meyer, and H.-J. Güntherodt, Ultrathin films of NaCl on Cu(111): a LEED and dynamic force microscopy study, *Surf. Sci.* **438** (1999), 289.

[68] R. Smoluchowski, Anisotropy of the electronic work function of metals, *Phys. Rev.* **60** (1941), 661.

[69] N. V. Smith, C. T. Chen, and M. Weinert, Distance of the image plane from metal surfaces, *Phys. Rev. B* **40** (1989), 7565.

[70] F. Olsson, M. Persson, J. Repp, and G. Meyer, Scanning tunneling microscopy and spectroscopy of NaCl overlayers on the stepped Cu(311) surface: Experimental and theoretical study, *Phys. Rev. B* **71** (2005), 075419.

[71] J. D. Jackson, *Classical electrodynamics*, Wiley, $2^{nd}$ edition (1975).

[72] D. Straub and F. J. Himpsel, Spectroscopy of image-potential states with inverse photoemission, *Phys. Rev. B* **33** (1986), 2256.

[73] C. D. Lindstrom, D.Quinn, and X.-Y. Zhu, Using image resonances to probe molecular conduction at the n-heptane/Au(111) interface, *J. Chem. Phys.* **122** (2005), 124714.

[74] T. Fauster and W. Steinmann, Two-photon photoemission spectroscopy of image states, in *Photonic probes of surfaces*, volume 2, chapter 8, 347, Elsevier (1995).

[75] J. Güdde, W. Berthold, and U. Höfer, Dynamics of electronic transfer processes at metal/insulator interfaces, *Chem. Rev.* **106** (2006), 4261.

[76] E. V. Chulkov, M. Machado, and V. M. Silkin, Inverse lifetime of the surface and image states on Au(111), *Vacuum* **61** (2001), 95.

[77] F. Stern, Self-consistent results for n-type Si inversion layers, *Phys. Rev. B* **5** (1972), 4891.

[78] N. W. Ashcroft and N. D. Mermin, *Solid state physics*, Thomson Learning (1976).

[79] W. R. Harper, The volta effect as a cause of static electrification, *Proc. R. Soc. London. A, Math. Phys. Sci.* **205** (1951), 83.

[80] J. Lowell, Contact electrification of metals, *J. Phys. D: Appl. Phys.* **8** (1975), 53.

[81] C. J. Fall, N. Binggeli, and A. Baldereschi, Work functions at facet edges, *Phys. Rev. Lett.* **88** (2002), 156802.

[82] N. A. Burnham, R. J. Colton, and H. M. Pollock, Work-function anisotropies as an origin of long-range surface forces, *Phys. Rev. Lett.* **69** (1992), 144.

[83] N. A. Burnham, R. J. Colton, and H. M. Pollock, Reply to comment on "Work-function anisotropies as an origin of long-range surface force", *Phys. Rev. Lett.* **70** (1993), 247.

[84] J. E. Inglesfield, Comment on "Work-function anisotropies as an origin of long-range surface force", *Phys. Rev. Lett.* **70** (1993), 246.

[85] C. Gerthsen and H. Vogel, *Physik*, Springer Verlag, $17^{th}$ edition (1993).

[86] P. Wahl, M. A. Schneider, L. Diekhöner, R. Vogelgesang, and K. Kern, Quantum coherence of image-potential states, *Phys. Rev. Lett.* **91** (2003), 106802.

[87] J. W. Gadzuk, Single-atom point source for electrons: Field-emission resonance tunneling in scanning tunneling microscopy, *Phys. Rev. B* **47** (1993), 12832.

[88] J. I. Pascual, C. Corriol, G. Ceballos, I. Aldazabal, H.-P. Rust, K. Horn, J. M. Pitarke, P. M. Echenique, and A. Arnau, Role of the electric field in surface electron dynamics above the vacuum level, *Phys. Rev. B* **75** (2007), 165326.

[89] N. Memmel, Monitoring and modifying properties of metal surfaces by electronic surface states, *Surf. Sci. Rep.* **32** (1998), 91.

[90] M. Ortuño and P. M. Echenique, Phase shifts, image planes, and surface states at metal surfaces, *Phys. Rev. B* **34** (1986), 5199.

[91] D. M. Kolb, W. Boeck, K.-M. Ho, and S. H. Liu, Observation of surface states on Ag(100) by infrared and visible electroreflectance spectroscopy, *Phys. Rev. Lett.* **47** (1981), 1921.

[92] S. Schuppler, N. Fischer, T. Fauster, and W. Steinmann, Bichromatic two-photon photoemission spectroscopy of image potential states on Ag(100), *Appl. Phys. A* **51** (1990), 322.

[93] W. R. Smythe, *Static and dynamic electricity*, International series in pure and applied physics, McGraw-Hill, New York (1968).

[94] T. J. Lewis, The work function of irregular metal surfaces, *Proc. Phys. Soc. B* **67** (1954), 187.

[95] M. J. Morant and H. House, The work function and patch field of an irregular metal surface, *Proc. Phys. Soc. B* **69** (1956), 14.

[96] J. K. Gimzewski and R. Möller, Transition from the tunneling regime to point contact studied using scanning tunneling microscopy, *Phys. Rev. B* **36** (1987), 1284.

[97] J. D. McNeill, J. R. L. Lingle, R. E. Jordan, D. F. Padowitz, and C. B. Harris, Interfacial quantum well states of Xe and Kr adsorbed on Ag(111), *J. Chem. Phys.* **105** (1996), 3883.

[98] B. Techaumnat and T. Takuma, Analysis of the electric field and force in an arrangement of a conducting sphere and a plane electrode with a dielectric barrier, *IEEE Trans. Dielectrics and Electrical Insulation* **13** (2006), 336.

[99] R. C. Leckey, Electronic structure of solids: Photoemission spectra and related data, in A. Goldmann and E.-E. Koch, editors, *Condensed Matter*, Landolt-Börnstein, 113, Springer Verlag (2006), III/23a 2.2.1.

[100] M. W. Cole, Electronic surface states of a dielectric film on a metal substrate, *Phys. Rev. B* **3** (1971), 4418.

[101] D. C. Marinica, C. Ramseyer, A. G. Borisov, D. Teillet-Billy, J. P. Gauyacq, W. Berthold, P. Feulner, and U. Höfer, Effect of an atomically thin dielectric film on the surface electron dynamics: Image-potential states in the Ar/Cu(100) system, *Phys. Rev. Lett.* **89** (2002), 046802.

[102] D. C. Marinica, C. Ramseyer, A. G. Borisov, D. Teillet-Billy, and J. P. Gauyacq, Image states on a free-electron metal surface covered by an atomically thin insulator layer, *Surf. Sci.* **528** (2003), 78.

[103] D. C. Marinica, C. Ramseyer, A. G. Borisov, D. Teillet-Billy, and J. P. Gauyacq, Quantum-well resonances and image states in the Ar/Cu(100) system, *Surf. Sci.* **540** (2003), 457.

[104] M. Robinson and A. H. Hallett, The static dielectric constant of NaCl, KCl, and KBr at temperatures between 4.2 K and 300 K, *Can. J. Phys.* **44** (1966), 2211.

[105] K. Natori, D. Otani, and N. Sano, Thickness dependence of the effective dielectric constant in a thin film capacitor, *J. Appl. Phys.* **73** (1998), 632.

[106] S. Patil, A. V. Kulkarni, and C. V. Dharmadhikari, Study of the electrostatic force between a conducting tip in proximity with a metallic surface: Theory and experiment, *J. Appl. Phys.* **88** (2000), 6940.

[107] J. P. Gauyacq and A. G. Borisov, Image states on finite size adsorbate islands: Ar on Cu(100), *Surf. Sci.* **600** (2006), 825.

[108] P. Avouris, I. W. Lyo, and P. Molinàs-Mata, STM studies of the interaction of surface state electrons on metals with steps and adsorbates, *Chem. Phys. Lett.* **240** (1995), 423.

[109] I. Merrick, J. E. Inglesfield, and G. A. Attard, Local work function and induced screening effects at stepped Pd surfaces, *Phys. Rev. B* **71** (2005), 085407.

[110] J. F. Jia, K. Inoue, Y. Hasegawa, W. S. Yang, and T. Sakurai, Variation of the local work function at steps on metal surfaces studied with STM, *Phys. Rev. B* **58** (1998), 1193.

[111] C. Schwennicke, J. Schimmelpfennig, and H. Pfnür, Morphology of thin NaCl films grown epitaxially on Ge(100), *Surf. Sci.* **293** (1993), 57.

[112] M. Cardona and L. Ley, Photoemission in solids I, in M. Cardona and L. Ley, editors, *Topics in applied physics*, volume 26, chapter 1, 1, Springer Verlag (1978).

[113] G. Ertl and J. Küppers, *Low energy electrons and surface chemistry*, VCH Verlagsgesellschaft, $2^{nd}$ edition (1985).

[114] U. Höfer, I. L. Shumay, C. Reuß, U. Thomann, W. Wallauer, and T. Fauster, Time-resolved coherent photoelectron spectroscopy of quantized electronic states on metal surfaces, *Science* **277** (1997), 1480.

[115] R. W. Schoenlein, J. G. Fujimoto, G. L. Eesley, and T. W. Capehart, Femtosecond relaxation dynamics of image-potential states, *Phys. Rev. B* **43** (1991), 4688.

[116] D. Velic, A. Hotzel, M. Wolf, and G. Ertl, Electronic states of the $C_6H_6$/Cu(111) system: Energetics, femtosecond dynamics, and adsorption morphology, *J. Chem. Phys.* **109** (1998), 9155.

[117] W. Wallauer and T. Fauster, Growth of Ag, Au, and Co on Cu(111) studied by high-resolution spectroscopy of image states, *Surf. Sci.* **331** (1995), 731.

[118] R. Fischer, T. Fauster, W. Von Der Linden, and V. Dose, Island-size distributions of Ag on Pd(111), *Surf. Rev. Lett.* **3** (1996), 1393.

[119] C. Reuß, W. Wallauer, and T. Fauster, Image states of Ag on Au(111), *Surf. Rev. Lett.* **3** (1996), 1547.

[120] N. Fischer, S. Schuppler, T. Fauster, and W. Steinmann, Coverage-dependent electronic structure of Na on Cu(111), *Surf. Sci.* **314** (1994), 89.

[121] A. K. Kazansky, A. G. Borisov, and J. P. Gauyacq, Image and adsorbate state dependence on the adsorbate coverage in the Na/Cu(111) system, *Surf. Sci.* **544** (2003), 309.

[122] H. H. Rotermund, Imaging of dynamic processes on surfaces by light, *Surf. Sci. Rep.* **29** (1997), 265.

[123] J. Hölzl and F. K. Schulte, Work function of metals, in *Springer tracts in modern physics*, volume 85, 1, Springer Verlag, Berlin (1979).

[124] J. A. Becker, Thermionic electron emission and adsorption part I. Thermionic emission, *Rev. Mod. Phys.* **7** (1935), 97.

[125] N. D. Lang, Interaction between closed-shell systems and metal surfaces, *Phys. Rev. Lett.* **46** (1981), 842.

[126] O. Y. Kolesnychenko, O. I. Shklyarevskii, and H. van Kempen, Calibration of the distance between electrodes of mechanically controlled break junctions using field emission resonance, *Rev. Sci. Instr.* **70** (1999), 1442.

[127] O. Y. Kolesnychenko, O. I. Shklyarevskii, and H. van Kempen, Giant influence of adsorbed helium on field emission resonance measurements, *Phys. Rev. Lett.* **83** (1999), 2242.

[128] O. Y. Kolesnychenko, Y. A. Kolesnichenko, O. I. Shklyarevskii, and H. van Kempen, Field-emission resonance measurements with mechanically controlled break junctions, *Physica B: Cond. Mat.* **291** (2000), 246.

[129] J. D. McNeill, J. R. L. Lingle, N.-H. Ge, C. M. Wong, R. E. Jordan, and C. B. Harris, Dynamics and spatial distribution of electrons in quantum wells at interfaces determined by femtosecond photoemission spectroscopy, *Phys. Rev. Lett.* **79** (1997), 4645.

[130] A. W. Dweydari and C. H. B. Mee, Work function measurements on (100) and (110) surfaces of silver, *Phys. status solidi A* **27** (1975), 223.

[131] M. Chelvayohan and C. H. B. Mee, Work function measurements on (110), (100) and (111) surfaces of silver, *J. Phys. C: Solid State Phys.* **15** (1982), 2305.

[132] B. Reihl and J. M. Nicholls, Image-potential surface states on Ag(100): A reinvestigation, *Z. Phys. B - Cond. Mat.* **67** (1987), 221.

[133] J. H. Coombs and J. K. Gimzewski, Fine structure in field emission resonances at surfaces, *J. Microscopy* **152** (1988), 841.

[134] W. Widdra, S. Großer, R. Shantyr, and C. Hagendorf, Stark-shifted image potential states: What we can learn from tunneling spectroscopies, in *Symposium on surface science*, Abstract book (2006) 23.

[135] H. Benia, N. Nilius, and H.-J. Freund, Photon mapping of MgO thin films with an STM, *Surf. Sci.* **601** (2007), L55.

[136] S. Schintke, S. Messerli, M. Pivetta, F. Patthey, L. Libioulle, M. Stengel, A. D. Vita, and W.-D. Schneider, Insulator at the ultrathin limit: MgO on Ag(001), *Phys. Rev. Lett.* **87** (2001), 276801.

[137] M. J. Overett, R. O. Hill, and J. R. Moss, Organometallic chemistry and surface science: mechanistic models for the Fischer-Tropsch synthesis, *Coord. Chem. Rev.* **206** (2000), 581.

[138] M. J. A. Tijmensena, A. P. C. Faaij, C. N. Hamelinck, and M. R. M. van Hardeveld, Exploration of the possibilities for production of Fischer-Tropsch liquids and power via biomass gasification, *Biomass Bioenergy* **23** (2002), 129.

[139] I. N. Remediakis, F. Abild-Pedersen, and J. K. Nørskov, DFT study of formaldehyde and methanol synthesis from CO and $H_2$ on Ni(111), *J. Phys. Chem.* **108** (2004), 14535.

[140] J. H. Miners, P. Gardner, A. M. Bradshaw, and D. P. Woodruff, A $CO_2$ surface molecular precursor during CO oxidation over Pt100, *J. Chem. Phys. B* **104** (2004), 14270.

[141] G. Ertl, Elementary steps in heterogeneous catalysis, *Angew. Chem. Int. Ed.* **29** (1990), 1219.

[142] F. El Gabaly, R. Miranda, and J. de la Figuera, Properties of dislocation half loops in Au(100): Structure, formation energy, and diffusion barrier, *Phys. Rev. B* **70** (2004), 012102.

[143] T. E. Wofford, S. M. York, and F. M. Leibsle, Properly interpreting scanning tunneling microscopy images: the Cu(100)-c(2x2)N surface revisited, *Surf. Sci.* **522** (2003), 47.

[144] S. M. Driver and D. P. Woodruff, Comment on "properly interpreting scanning tunneling microscopy images: the Cu(100)-c(2x2)N surface revisited", *Surf. Sci.* **539** (2003), 182.

[145] T. E. Wofford, S. M. York, and F. M. Leibsle, Reply to comment on: "properly interpreting scanning tunneling microscopy images: the Cu(100)-c(2x2)N surface revisited", *Surf. Sci.* **539** (2003), 186.

[146] B. An, M. Xu, S. Fukuyama, and K. Yokogawa, Nitrogen-induced structures of a Nb(100) surface investigated by LEED, Auger electron spectroscopy, and STM, *Phys. Rev. B* **73** (2006), 205401.

[147] L. Leung, C. A. Muryn, and G. Thornton, Single molecule vibrational spectroscopy of $N_2$ on Cu(110), *Surf. Sci.* (2004), 671.

[148] A. J. Heinrich, C. P. Lutz, J. A. Gupta, and D. M. Eigler, Molecule cascades, *Science* **298** (2002), 1381.

[149] M. Kulawik, H.-P. Rust, N. Nilius, M. Heyde, and H.-J. Freund, STM studies of ordered $(\sqrt{31} \times \sqrt{31})$R9° CO islands on Ag(111), *Phys. Rev. B* **71** (2005), 153405.

[150] L. Bartels, G. Meyer, and K.-H. Rieder, The evolution of CO adsorption on Cu(111) as studied with bare and CO-functionalized scanning tunneling tips, *Surf. Sci.* **432** (1999), L621.

[151] K. Morgenstern and J. Nieminen, Intermolecular bond length of ice on Ag(111), *Phys. Rev. Lett.* **88** (2002), 066102.

[152] T. Mitsui, M. K. Rose, E. Fomin, D. F. Ogletree, and M. Salmeron, Water diffusion and clustering on Pd(111), *Science* **297** (2002), 1850.

[153] L. J. Lauhon and W. Ho, Direct observation of the quantum tunneling of single hydrogen atoms with a scanning tunneling microscope, *Phys. Rev. Lett.* **85** (2000), 4566.

[154] Y. Okawa and K.-I. Tanaka, STM investigation of the reaction of Ag—O added rows with $CO_2$ on a Ag(110) surface, *Surf. Sci.* **344** (1995), L1207.

[155] X.-C. Guo and R. J. Madix, $CO_2$ + O on Ag(110): Stoichiometry of carbonate formation, reactivity of carbonate with CO, and reconstruction-stabilized chemisorption of $CO_2$, *J. Phys. Chem. B* **105** (2001), 3878.

[156] X. C. Guo and R. J. Madix, Adsorption of oxygen and carbon dioxide on cesium-reconstructed Ag(110) surface, *Surf. Sci.* **550** (2004), 81.

[157] Y. Lilach, L. Romm, T. Livneh, and M. Asscher, The first layers of water on Ru(001), *J. Phys. Chem. B* **105** (2001), 2736.

[158] Y. Lilach and M. Asscher, Compression and caging of $CD_3Cl$ by $H_2O$ layers on Ru(001), *J. Chem. Phys.* **117** (2002), 6730.

[159] C. Mundt and C. Benndorf, Influence of steps on the $H_2O$ adsorption on Ni(s)(111), *Surf. Sci.* **287** (1993), 119.

[160] R. Brosseau, M. R. Brustein, and T. H. Ellis, Water adsorption on Cu(100): The effect of defects, *Surf. Sci.* **294** (1993), 243.

[161] M. B. Hugenschmidt, L. Gamble, and C. T. Campbell, The interaction of $H_2O$ with a $TiO_2(110)$ surface, *Surf. Sci.* **302** (1994), 329.

[162] K. Onda, B. Li, and H. Petek, Two-photon photoemission spectroscopy of $TiO_2(110)$ surfaces modified by defects and $O_2$ or $H_2O$ adsorbates, *Phys. Rev. B* **70** (2004), 045415.

[163] R. Linke, T. Pelster, M. Tanemura, C. Becker, and K. Wandelt, Adsorption of CO on the ordered $Ni_3Al(111)$ surface, *Surf. Sci.* **402** (1998), 76.

[164] Y. G. Shen, D. J. O'Connor, and J. Yao, The adsorption of Al on Pd(001) and of O and CO on an interfacial Al-alloyed Pd(001) surface, *Appl. Surf. Sci.* **125** (1998), 300.

[165] K. Habermehl-Ćwirzeń and J. Lahtinen, Sulfur poisoning of the CO adsorption on Co(0001), *Surf. Sci.* **573** (2004), 183.

[166] M. Grüne, G. Boishin, R.-J. Linden, and K. Wandelt, CO adsorption on the c(8×2)-Mn/Cu(100) phase, *Surf. Sci.* **433** (1999), 221.

[167] J. S. Muenter, Electric dipole moment of carbon monoxide, *J. Mol. Spec.* **55** (1975), 490.

[168] G. Blyholder, Molecular orbital view of chemisorbed carbon monoxide, *J. Phys. Chem.* **68** (1964), 2772.

[169] I. Bönicke, W. Kirstein, S. Spinzig, and F. Thieme, CO adsorption studies on a stepped Cu(111) surface, *Surf. Sci.* **313** (1994), 231.

[170] K.-H. Ernst, D. Schlatterbeck, and K. Christmann, Adsorption of carbon dioxide on Cu(110) and on hydrogen and oxygen covered Cu(110) surfaces, *Phys. Chem. Chem. Phys* **1** (1999), 4105.

[171] T. U. Nahm and R. Gomer, Desorption of $H_2$ from W(110) and Fe covered W(110) surfaces, *Surf. Sci.* **380** (1997), 434.

[172] P. K. Schmidt, K. Christmann, G. Kresse, J. Hafner, M. Lischka, and A. Groß, Coexistence of atomic and molecular chemisorption states: $H_2$/Pd(210), *Phys. Rev. Lett.* **87** (2001), 096103.

[173] M. Golze, M. Grunze, and W. Unertl, A multitechnique approach to chemisorption studies: The $N_2$-Ni(110) system, *Prog. Surf. Sci.* **22** (1986), 101.

[174] L. J. Lauhon and W. Ho, Single-molecule vibrational spectroscopy and microscopy: CO on Cu(001) and Cu(110), *Phys. Rev. B* **60** (1999), R8525.

[175] A. Sandell, P. Bennich, A. Nilsson, B. Hernnäs, O. Björneholm, and N. Måtensson, Chemisorption of CO on Cu(100), Ag(110) and Au(110), *Surf. Sci.* **310** (1994), 16.

[176] W. Hansen, M. Bertolo, and K. Jacobi, Physisorption of CO on Ag(111) : investigation of the monolayer and the multilayer through HREELS, ARUPS, and TDS, *Surf. Sci.* **253** (1991), 1.

[177] S. Krause, C. Mariani, K. C. Prince, and K. Horn, Screening effects in photoemission from weakly bound adsorbates: CO on Ag(110), *Surf. Sci.* **138** (1984), 305.

[178] L. Bartels, G. Meyer, and K.-H. Rieder, Controlled vertical manipulation of single CO molecules with the scanning tunneling microscope: A route to chemical contrast, *Appl. Phys. Lett.* **71** (1997), 213.

[179] J. Kouvetakis, R. B. Kaner, M. L. Sattler, and N. Bartlett, A novel graphite-like material of composition $BC_3$, and nitrogen-carbon graphites, *J. Chem. Soc. Chem. Comm.* (1986), 1758.

[180] J. Nagamatsu, N. Nakagawa, T. Muranaka, Y, Zenitani, and J. Akimitsu, Superconductivity at 39 K in magnesium diboride, *Nature* **410** (2001), 63.

[181] R. M. Wentzcovitch, M. L. Cohen, S. G. Louie, and D. Tománek, $\sigma$-states contribution to the conductivity of $BC_3$, *Solid State Comm.* **67** (1988), 515.

[182] H. Rosner, A. Kitaigorodsky, and W. E. Pickett, Prediction of high $T_c$ superconductivity in hole-doped LiBC, *Phys. Rev. Lett.* **88** (2002), 127001.

[183] R. A. Jishi, M. Benkraouda, and J. Bragin, Possibility of superconductivity in $Mg_2BC_3$, *Phys. Lett. A* **306** (2003), 358.

[184] H. Tanaka, Y. Kawamata, H. Simizu, T. Fujita, H. Yanagisawa, S. Otani, and C. Oshima, Novel macroscopic $BC_3$ honeycomb sheet, *Solid State Comm.* **136** (2005), 22.

[185] H. Yanagisawa, T. Tanaka, Y. Ishida, E. Rokuta, S. Otani, and C. Oshima, Phonon dispersion curves of stable and metastable $BC_3$ honeycomb epitaxial sheets and their chemical bonding: Experiment and theory, *Phys. Rev. B* **73** (2006), 045412.

[186] H. Yanagisawa, T. Tanaka, Y. Ishida, M. Matsue, E. Rokuta, S. Otani, and C. Oshima, Phonon dispersion curves of a $BC_3$ honeycomb epitaxial sheet, *Phys. Rev. Lett.* **93** (2004), 177003.

[187] F, J. Ribeiro, and M. L. Cohen, Possible superconductivity in hole-doped $BC_3$, *Phys. Rev. B* **69** (2004), 212507.

[188] K. Kobayashi, Moiré pattern in scanning tunneling microscopy of monolayer graphite, *Phys. Rev. B* **50** (1994), 4749.

[189] Y. Yamada, A. Sinsarp, M. Sasaki, and S. Yamamoto, Moiré-like distribution of local tunneling barrier height of the monolayer graphite adsorbed on Pt(111) surface, *Jpn. J. Appl. Phys.* **41** (2002), 7501.

[190] D. Tomanek, R. M. Wentzcovitch, S. G. Louie, and M. L. Cohen, Calculation of electronic and structural properties of $BC_3$, *Phys. Rev. B* **37** (1988), 3134.

[191] M. J. Puska, R. M. Nieminen, M. Manninen, B. Chakraborty, S. Holloway, and J. K. Nørskov, Quantum motion of chemisorbed hydrogen on Ni surfaces, *Phys. Rev. Lett.* **51** (1983), 1081.

[192] C. Dong, P. Mehrotra, and G. R. Myneni, Methods for reducing hydrogen outgassing, in G. R. Myneni and S. Chattopadhyay, editors, *AIP Conference Proceedings: Hydrogen in Materials and vacuum systems*, volume 671, American institute of physics (2003) 307.

[193] P. A. Redhead, Hydrogen in vacuum systems: an overview, in G. R. Myneni and S. Chattopadhyay, editors, *AIP Conference Proceedings: Hydrogen in materials and vacuum systems*, volume 671, American institute of physics (2003) 243.

[194] E.-G. Wei, K. Tsuzaki, and T. Hara, A new method to determine the activation energy for hydrogen desorption from steels, *Material Science Forum* **475** (2005), 229.

[195] B. Techaumnat and T. Takuma, Calculation of the electric field for lined-up spherical dielectric particles, *IEEE Trans. Dielectrics and Electrical Insulation* **10** (2003), 623.

[196] B. Techaumnat, B. Eua-arporn, and T. Takuma, Calculation of electric field and dielectrophoretic force on spherical particles in chain, *J. Appl. Phys.* **95** (2004), 1586.

[197] W. Koepf, *Hypergeometric summation: An algorithmic approach to summation and special function identities*, Vieweg, Braunschweig, Germany (1998).

[198] E. W. Weisstein, Binomial coefficient, from *Mathworld* – a Wolfram Web resource `http://mathworld.wolfram.com/BinomialCoefficient.html`.